Complex Source Geometries in Volcano Seismology

Rodrigo Andrés Contreras Arratia

School of Earth and Environment

University of Leeds

A thesis submitted for the degree of

Doctor of Philosophy

September 15, 2020

Declaration

The candidate confirms that the work submitted is his own, except where work which has formed part of jointly authored publications has been included. The contribution of the candidate and the other authors to this work has been explicitly indicated below. The candidate confirms that appropriate credit has been given within the thesis where reference has been made to the work of others.

The work in Chapter 2 of the thesis has appeared in publication at Journal of Volcanology and Geothermal Research:

I developed the numerical and theoretical framework for finite seismic complex sources. I produced forward models which were subjected to moment tensor inversions. I extracted information from the radiation produced and the inversions in order to understand how these sources work. I analysed the results, wrote the manuscript and created all of the figures. Jurgen Neuberg provided comments and suggestions, which improved the analysis and manuscript.

The work in Chapter 3 of the thesis is a collective contribution in preparation:

I applied the same models for curved seismic sources to explain the trigger of low-frequency seismicity at Soufrière Hills volcano, Montserrat, West Indies, during the phase 1 of eruption in 1997. I estimated the seismic moments of these seismic events, correct them for a ring source geometry and re-estimate the magma ascent. Finally we compared these slip values with the overall magma extrusion observed.

The work in Chapter 4 of the thesis is accepted for publication at Journal of Volcanology and Geothermal Research:

I applied the models for curved seismic sources to the case of seismicity at Bárðarbunga caldera, Iceland, during the collapse event in 2014-2015. I tested partial-ring synthetic sources and retrieve solutions with non-DC component. Moreover, I recalculated the seismic moment of all seismicity in order to reassess the cumulative seismic moment, during the collapse, and compare it with the geodetic moment reported by other authors. I analysed the results, wrote the manuscript and created all of the figures. Jurgen Neuberg provided comments and suggestions, which improved the analysis and manuscript.

This thesis is dedicated to my wife Kristina and daughter Polina.
Thanks for your support...

To my parents Adelaida and Orlando, whose effort took me where I am today...

... Last, but not least, to my grandparents Margarita, Lucho, Nina and Delia. Their courage, resilience and love opened opportunities for all my family. Eternally grateful for that.

Acknowledgements

I want to thank my beloved wife Kristina, who has given me incredible support during this process, especially during this stressful lockdown/finishing thesis time. Thanks also to my little Polina, who enlighten my days and make me forget about problems.
To my whole family in Chile, parents, sisters, nephews, aunties, uncles and cousins, who have been constantly interested in my advances and wellbeing.
Special thanks to my supervisor Jurgen Neuberg (Locko), for all the knowledge given, constructive comments and the great relationship we have. It was a great experience to work with him. I hope it will continue.
Thanks to my colleagues at IGT, especially to Eduardo Morgado, Luke Marsden and Dinko Sindija, for the good moments and all the endless discussions we had, they helped me to better understand the science behind this thesis.
Infinite thanks to IT team, especially to Richard Rigby, who has helped me to solve problems since day 1. Also, to the High Performance Computing team and facilities at the University of Leeds, UK.

Finally, thanks to ANID Chile, the organisation that funded my studies through its scholarship program Becas Chile (72170194).

Abstract

The seismic source for small to moderate earthquakes is usually described by a point source on a planar geometry, where the amplitudes observed are linearly dependent on the seismic moment and the waveforms are predicted by the seismic theory. Particularly in volcanic settings, there is increasing evidence of non-planar ruptures which follow complex geometries instead, such as ring faults (conduits and calderas) and dyke faults. I propose and describe the action of complex sources as a superposition of point sources aligned along with ring structures and dykes. Synthetic seismograms are calculated and their magnitudes and waveforms analysed, finding that moment tensor inversions systematically underestimate the seismic moment or magnitude, the displacement at the fault is misinterpreted and the source dynamics follow mainly isotropic behaviour. For long wavelengths, I can treat the waves as coherent and a moment tensor inversion under a point source approach is applicable. However, this source parameters need to be carefully analysed and eventually corrected for a complex source. The correction factor for each different source studied can be calculated, thus, a corrected value for the seismic moment is available under these conditions. To test the results obtained, low-frequency events at Soufrière Hills are considered, in which the rupture is produced by brittle behaviour of magma within a conduit, the seismic moment correction is applied to the slip maintaining the area as constant, enhancing those values to match geological observations in rhyolitic volcanoes. Furthermore, partial-ring ruptures are modelled to emulate the collapse of Bárðarbunga caldera in Iceland. In this case, the correction over the seismic moment is attributable to the rupture area, maintaining the

cumulative slip as constant. This applied correction improves the reconciliation of the seismic and geodetic moment for Bárðarbunga. For both cases, the inclusion of a curved source explains more accurately the observations and the conclusions are more realistic. Collaterally, I found evidence of network-dependent results, alongside intrinsic uncertainties in the location of these sources which needs to be taken into account for an improved source description.

Contents

List of Figures

List of Tables

Abbreviations

List of Acronyms

ISO	Isotropic component
DC	Double couple
CLVD	Compensated linear vector dipole
MT	Moment tensor
MTI	Moment tensor inversion
VT	Volcano-tectonic seismic event
LP	Long period seismic event
VLP	Very long period seismic event
non-DC	Non double couple component
SF	Single force
DRE	Dense rock equivalent
UTC	Coordinated universal time
MVO	Montserrat Volcano Observatory
MBLG	Long Ground station, MVO
IMO	Icelandic Meteorological Office

List of Symbols

M_0	Seismic moment
M_w	Moment magnitude
μ	Rigidity
ρ	Bulk density
A	Rupture area
d	Average slip
M_{xy}	Components of moment tensor
u_i	i-th component of displacement at the stations
F_j	j-th component of the single force applied
G_{ik}	Components of the Green's functions
r, θ, ϕ	Spherical coordinates
$A_{\mathrm{ISO}}^{\mathrm{N}}$	Radiation pattern near-field ISO component
$A_{\mathrm{ISO}}^{\mathrm{FP}}$	Radiation pattern P far-field ISO component

$A_{\mathrm{ISO}}^{\mathrm{FS}}$	Radiation pattern S far-field ISO component
$A_{\mathrm{DC}}^{\mathrm{N}}$	Radiation pattern near field DC component
$A_{\mathrm{DC}}^{\mathrm{FP}}$	Radiation pattern P far-field DC component
$A_{\mathrm{DC}}^{\mathrm{FS}}$	Radiation pattern S far-field DC component
$A_{\mathrm{CLVD}}^{\mathrm{N}}$	Radiation pattern near field CLVD component
$A_{\mathrm{CLVD}}^{\mathrm{FP}}$	Radiation pattern P far-field CLVD component
$A_{\mathrm{CLVD}}^{\mathrm{FS}}$	Radiation pattern S far-field CLVD component
τ_{xy}	Components of shear stress tensor
η	Bulk viscosity
$\dot{\epsilon}_{xy}$	Components of strain rate tensor
L	Distance source-station
R	Radius of ring
λ (Chapter 1)	Wavelength
f	Displacement at the source
r_{ij},θ_{ij},ϕ_{ij}	Spherical coordinates between i-th station and j-th source
δ_{r}	Angle increments for integration
v_{P}	P-wave velocity
v_{S}	S-wave velocity
T (Chapter 2)	Period of wave
t_{offset}	Time between the last source acting and first one
d_{max}	Maximum distance between point sources
r/d	Radius of curvature / source-station distance
a_i	P-wave amplitude radiation in the direction i
A_i	Net P-wave amplitude radiation in the direction i
A_{max}	Maximum amplitude
ρ_{MELT}	Melt density
ρ_{BULK}	Bulk density
T (Chapter 3)	Temperature
M_{m}	Molar mass of water
P	Lithostatic pressure
n_{TOTAL}	Volatile content
n_{eg}	Fraction of exsolved volatiles
n_{dg}	Fraction of dissolved volatiles
χ	Gas fraction
ρ_{g}	Volatile density
$\Phi_{1.5}$	Magma flux at 1.5 km
Φ_0	Magma flux at surface
δ	Dip angle
λ (Chapter 4)	Rake angle
M_0^P/M_0	Correction factor

$M_0^{(g)}$	Geodetic moment

Chapter 1

Introduction

1.1 Overview

Seismology is the area of Geosciences that studies the propagation of waves across the Earth in order to understand geophysical processes and the structure of the planet. For example, some applications in volcanic environments are: tomography studies (Greenfield et al., 2016), seismic source processes (Ágústsdóttir et al., 2019; Chouet et al., 2003; Kumagai et al., 2011; Mildon et al., 2016; Neuberg, 2000; Neuberg et al., 2006; Richardson and Waite, 2013; Ruiz et al., 2006; White et al., 2011), temporal changes of elastic properties (Donaldson et al., 2017; Lecocq et al., 2014), volcanic activity (Ágústsdóttir et al., 2016; Green and Neuberg, 2006; Lyons and Waite, 2011; Miller et al., 1998), among others. In this thesis, we focus on the understanding of seismic sources in volcanic environments and study their implications for the assessment of volcanic activity, since they are closely linked (Chouet et al., 2003; Feuillet et al., 2004).

A wide range of seismic signals are produced in volcanic environments, e.g. the so-called volcano-tectonic (VT) earthquakes are usually explained by the rupture of a brittle material due to stresses that overcome the strength of rocks in particular orientations i.e. they satisfy the Mohr-Coulomb failure criterion (Labuz and Zang, 2012; Scholz, 2002). In addition, more complex seismic sources occur in a medium which comprises a mixture of crystals, gases and molten rock. These can be explained by different source processes, such as pressurisation, depressurisation,

explosions, brittle failure in magma and slow waves trapped in fluid containers. These are summarised in Chouet and Matoza (2013) or in a short version in Neuberg (2011)(Fig. 1.1).

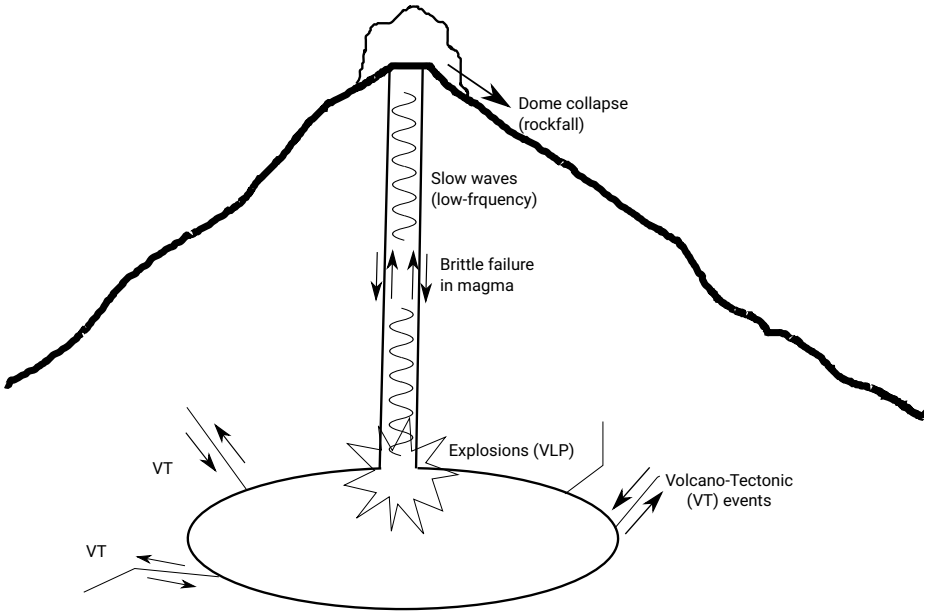

Figure 1.1: Schematic representation of the seismic processes occurring inside a volcano. Volcano-Tectonic events (VT) occur due to brittle failure of rock, explosions due to overpressure, low-frequency events (LF) due to slow waves trapped in fluid-filled conduits and rockfalls due to dome collapses and pyroclastic flows. Tremor signals comprise superposition of VT or LF events.

Catastrophic volcanic events such as dome collapse and explosions are closely linked to the occurrence of long-period (LP) and Hybrid seismic events in volcanoes with high silica content. Therefore, this type of seismicity is an important forecasting tool (Chouet, 1996; Cruz and Chouet, 1997). Hybrid events comprise a high-frequency onset (trigger) which provides the energy input for long-period oscillations trapped in a fluid-filled structure to occur (Chouet et al., 2003; Ferrazzini and Aki, 1987). The most commonly obtained MT result for the long-period oscillation points to a compensated linear vector dipole (CLVD) or crack solution with a pulsating source time function (Kumagai et al., 2002; Lokmer et al., 2007).

However, these models cannot explain the trigger mechanism due to an oversimplification of the source. Moreover, they completely ignore the rate of magma extrusion, which should be linked to seismicity. In order to understand the trigger of long-period seismicity within a resonating conduit, alternative models based on brittle magma failure (Neuberg et al., 2006) or stick-slip motion (Iverson et al., 2006) were developed and their non-planar geometries will be tested in Chapters 2, 3 and 4, and discussed in Chapter 5.

At calderas, a collapsing or uplifting movement is linked to pure shear seismicity at a curved source. However, due to the fault shape, the usual source mechanism that explains shear failure, i.e. double couple (DC), is not appropriate. Studies show that sources of moderate to big earthquakes in calderas $M_{\mathrm{W}} > 4$, can be modelled by a CLVD (Ekström, 1994; Nettles and Ekström, 1998; Tkalčić et al., 2009), the physical rupture considers a conical ring fault with reverse faulting. Shuler et al. (2013a,b) advanced the description by also considering an isotropic (ISO) component for the source, i.e. explosion or implosion, which provides a more complete description of the source. In addition, during the 2014 collapse episode at Bárðarbunga caldera, the larger events show a CLVD component dominating the source (Gudmundsson et al., 2016; Riel et al., 2015), while the smallest events show simple DC solutions. Since a caldera by definition is a ring fault, small earthquakes are produced in a very small area, which can be approximated as planar. However, for bigger earthquakes, the curvature of the fault comes into play and a curved source is more appropriate. Finally, a kinematic inversion of a ring fault rupture at Bárðarbunga during the crisis in 1996, shows a full-ring rupture releasing the same seismic moment along all sections of the ring (Fichtner and Tkalčić, 2010). A more complete description is needed for these cases since the inferred CLVD plus isotropic sources can be indicators of full- or partial-ring ruptures, which leads to discrepancies in the slip history and magnitude estimation of the earthquake due to seismic wave interference (Contreras-Arratia and Neuberg, 2019).

Moment tensor (MT) inversions are the essential step in order to understand the physical rupture processes involved. However, the strong assumption of a point source might be an oversimplification and the method will provide inaccurate results. For pure shear ruptures on a planar fault, the seismic moment M_0 is linearly dependent to both the rupture area and the average slip (Aki and Richards,

2002), however, for different fault geometries, this might no longer apply. Volcano seismicity has been widely studied and results reported comprise the full spectrum of source models. Besides the usual double couple (DC) solutions for tectonic earthquakes (Ágústsdóttir et al., 2016; White et al., 2011), explosions/implosions have been suggested (Chouet et al., 2003; Kumagai et al., 2011; Ruiz et al., 2006), alongside with exploding/imploding cracks (Mildon et al., 2016), CLVD (Shuler et al., 2013a,b) and even single forces (Richardson and Waite, 2013). All these studies are based upon the fundamental point source assumption, i.e. classic MT inversions. The interpretation of these results in a complex rupture scheme has been inconclusive so far.

Here, we advance the description of the seismic source by including the representation of a complex fault by a superposition of single point sources, over spatially extended, complex structures, such as dykes and ring faults. We consider dyke ruptures, formed by two opposed double couples in close proximity, three cases of partial-ring rupture and full-ring rupture. The seismic trigger of LP and Hybrid events has been explained through the rupture of highly viscous magma at the conduit walls due to high strain rates (Neuberg et al., 2006) or a stick-slip motion at the conduit walls (Iverson et al., 2006) and caldera rims (Ekström, 1994). We produce synthetic seismograms using these alternative non-planar sources and extract the main features of their seismic radiation, which are compared to single DC and CLVD sources. We found that amplitudes, polarisations, and waveforms can change dramatically. This has important implications for magnitude estimation, and therefore, on the average slip, rupture area, slip history, magma ascent rate estimations and caldera subsidence estimations. These models and results are applied in case studies of hybrid swarms at Montserrat, and to the calculation of the cumulative seismic moment for Bárðarbunga caldera.

1.2 Seismic sources

The study of seismic sources is very important in seismology, as it provides information about the forces involved in generating the earthquake. By using observational data we can solve the inverse problem, obtain the main source parameters

and propose a physical model for the rupture, which needs to be in accordance with the volcanic or geodynamical context.

1.2.1 Mathematical representation

Seismic sources are discontinuities in an elastic medium which produce sudden displacements due to stresses applied within the elastic body. The dynamics of an elastic medium is governed by the equation of elastodynamics, which considers the different sources applied within the body. It is given by,

$$\rho \frac{\partial^2 u_i}{\partial t^2} = \partial_j \tau_{ij} + f_i \tag{1.1}$$

(Aki and Richards, 2002) where u_i are the displacements at any point of the medium in the $i-th$ direction, t is time, ρ is the density of the medium, τ_{ij} is the stress tensor, f_i a body-force and $\partial_j \tau_{ij}$ is the divergence operator applied to the stress tensor $\underline{\underline{\tau}}$. The seismic source can be represented by the body-force $\underline{f}$.

If we consider a static solution, where the left-hand side in Eq. 1.1 is zero, we obtain deformation equations used in geodesy (Okada, 1985, 1992). In addition, in the absence of body-forces, we obtain a wave solution which comprises P and S waves, i.e. while considering temporal variations for the solutions, the stresses are transmitted inside the earth as waves. In seismology, we consider as source terms external forces which can be represented through either single forces $\underline{F}$ or moment tensors $\underline{\underline{M}}$ (MT) acting at a point source. The solution for Eq. 1.1 is given by,

$$u_i(\underline{x}, t) = F_j(\underline{\xi}, \tau) * G_{ij}(\underline{\xi}, \underline{x}, \tau, t) \tag{1.2}$$

or,

$$u_i(\underline{x}, t) = M_{jk}(\underline{\xi}, \tau) * G_{ij,k}(\underline{\xi}, \underline{x}, \tau, t). \tag{1.3}$$

depending on the representation of the source. The mathematical representation of the moment tensor is shown in Eq. 1.4 (Aki and Richards, 2002) and a schematic

representation in Fig. 1.2,

$$\underline{\underline{M}} = \begin{pmatrix} M_{11} & M_{12} & M_{13} \\ M_{21} & M_{22} & M_{23} \\ M_{31} & M_{32} & M_{33} \end{pmatrix} \tag{1.4}$$

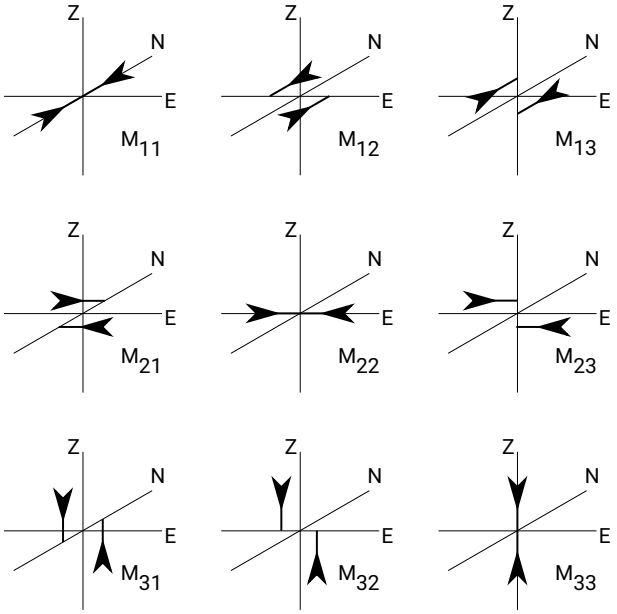

Figure 1.2: Pairs of forces representing the nine components of the symmetric moment tensor. The first index of the moment tensor component represents the direction of the force and the second the direction of the normal vector to a surface. The superposition of all these components represents all the possible force equivalents that ensure conservation of momentum.

where the first index denotes the direction of forces applied at the boundaries of an elastic volume i.e. its external area, the second index denotes the direction of the vector normal to the area where the force is applied, $1, 2, 3 = N, E, Z$, where Z is downwards. The diagonal components of the tensor contain information about opening/closing in given directions. On the other hand, the non-diagonal components contain information about shear movements, known as double couples (DC). It is important to note that this tensor is symmetric, i.e. $M_{ij} = M_{ji}$.

Double couples (DC) are the simplest and the most commonly used description to model an earthquake, most of the seismicity recorded worldwide can be

successfully describe using this approach i.e. dominant DC component, with small non-DC components (Ekström et al., 2012). Nonetheless, non-DC solutions are also used to describe seismicity, especially for volcanic earthquakes. An isotropic mechanism (ISO) represents a change in volume in all directions, mathematically represented as $M_{11} = M_{22} = M_{33}$. Negative diagonal components represent an implosion and positive components represent an explosion. If the opening occurs in only one direction the source represents an opening crack. Finally, a CLVD is represented by one diagonal component having twice the negative value of the remaining two such that the diagonal sum equals zero, hence no volume change occurs (e.g. $M_{11} = -2M_{22} = -2M_{33}$) (Fig. 1.4). The DC, ISO and CLVD sources are a set of end members of the moment tensor and they can be linearly weighted, i.e. any moment tensor can be decomposed into a sum of these sources (Jost and Herrmann, 1989; Vavryčuk, 2015).

These end members of the moment tensor have particular radiation properties. The so-called radiation pattern contains information about the amplitude distribution predicted in different directions for near-field (N), far-field P (FP) and S waves (FS), which is dependent on the geometry and orientation of the event. The isotropic, DC and CLVD radiation are shown in Eqs. 1.5,1.6,1.7, all of them as functions of the take-off angle θ and azimuth ϕ (Fig. 1.3) (Lokmer and Bean, 2010),

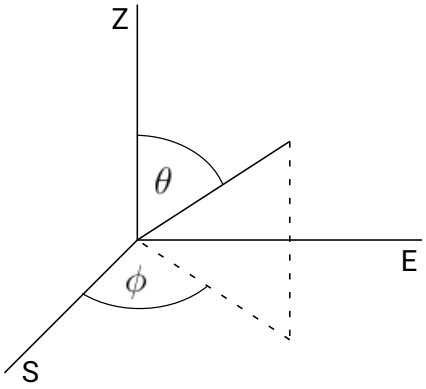

Figure 1.3: Spherical geometry for the description of radiation patterns. Azimuth angle ϕ and take-off angle θ from the seismic point source at the origin.

$$
\begin{aligned}
A^{\mathrm{N}}_{\mathrm{ISO}} &= 0 \\
A^{\mathrm{FP}}_{\mathrm{ISO}} &= \hat{r} \\
A^{\mathrm{FS}}_{\mathrm{ISO}} &= 0
\end{aligned}
\tag{1.5}
$$

$$
\begin{aligned}
A^{\mathrm{N}}_{\mathrm{DC}} &= 9\sin(2\theta)\cos(\phi)\hat{r} - 6(\cos(2\theta)\cos(\phi)\hat{\theta} - \cos(\theta)\sin(\phi)\hat{\phi}) \\
A^{\mathrm{FP}}_{\mathrm{DC}} &= 2\sin(2\theta)\cos(\phi)\hat{r} \\
A^{\mathrm{FS}}_{\mathrm{DC}} &= \cos(2\theta)\cos(\phi)\hat{\theta} - \cos(\theta)\sin(\phi)\hat{\phi}
\end{aligned}
\tag{1.6}
$$

$$
\begin{aligned}
A^{\mathrm{N}}_{\mathrm{CLVD}} &= \frac{9}{4}[1 + 3\cos(2\theta)]\hat{r} + \frac{9}{2}\sin(2\theta)\hat{\theta} \\
A^{\mathrm{FP}}_{\mathrm{CLVD}} &= [1 - \frac{3}{2}\sin^2(\theta)]\hat{r} \\
A^{\mathrm{FS}}_{\mathrm{CLVD}} &= -\frac{3}{4}\sin(2\theta)\hat{\theta}
\end{aligned}
\tag{1.7}
$$

where A are the amplitudes predicted, N is the near-field, FP is the far-field P wave radiation and FS is the far-field S wave radiation. These equations show, for example, that the ISO component shows the same amplitudes in all directions for P waves and no S wave radiation, thus, the amplitudes can only vary with path effects, e.g. geometrical spreading, attenuation, refractions, reflections or site effects. The case of a DC is particularly interesting since even though it occurs on a plane, there are two plane surfaces where no radiation is emitted, i.e. nodal planes. The maximum amplitudes for the P-wave far-field radiation are predicted at 45° from both fault planes and they have positive and negative values, meaning compression and dilatation at the seismic station, respectively. These cases of radiation patterns are shown in Fig. 1.4. We must note that this representation for radiation patterns is valid only for a single point source. Hence, the radiation patterns are based on the assumption that there are no travel time differences between seismic waves originating from different parts of extended sources.

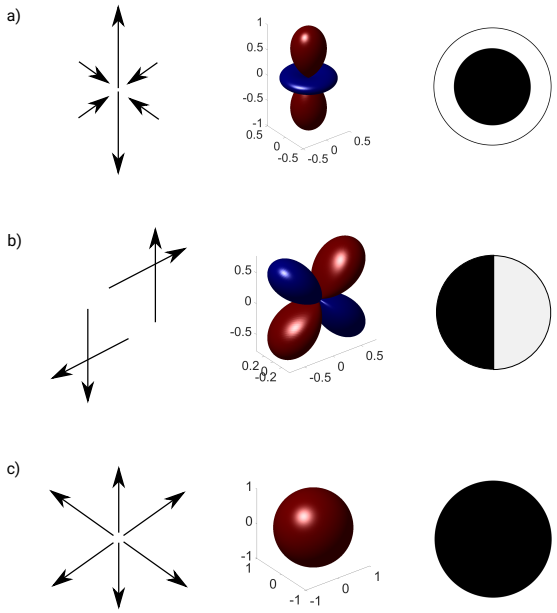

Figure 1.4: Schematic representation of the forces involved at the seismic source given by the arrows, the radiation pattern with red as the tension lobe and blue the compression lobe. Moreover, the focal mechanisms showing the lower projection of the focal sphere in black the tension and white the compression directions. a) Compensated Vector Linear Dipole (CLVD). b) Double Couple (DC). c) Isotropic Source (ISO).

1.2.2 Moment Magnitude

The seismic moment is a measure of the size of an earthquake, it can be calculated from the components of the moment tensor, and is given by,

$$M_0 = \frac{1}{\sqrt{2}}||\underline{\underline{M}}|| \tag{1.8}$$

at the same time, the moment magnitude M_{W} of an earthquake is linked to the seismic moment,

$$M_{\mathrm{W}} = \frac{2}{3}(\log_{10} M_0 - 9.1), \qquad M_0 \text{ is in [Nm]} \tag{1.9}$$

which considers all MT components, i.e. all possible pairs of forces acting at the volumetric source. The physical meaning of the seismic moment can be inferred

when we assume a pure shear source (DC) acting on a point in space. In this case, the definition of the seismic moment is reduced to,

$$M_0 = \mu A d \tag{1.10}$$

where μ is the rigidity of the country rock, A is the rupture area and d is the average slip on the fault. The term μA has units of force, and slip units of distance, therefore, the seismic moment is a measure of the energy released into seismic waves when the earthquake occurs. The seismic moment linearly increases when either the rupture area or the slip increases.

1.2.3 Inversion of source parameters

In practice, seismometers are deployed around the seismic source and from the recorded seismograms we can obtain information about source parameters and subsurface structure. This process is an inversion problem and we will focus on the inversion of the moment tensor (MT) in volcanic settings. The following is the expression for the displacement at any point in space in the i-th direction, which allows us to calculate the best estimation for M_{jk} and F_j,

$$u_i(\underline{x}, t) = M_{jk}(\underline{\xi}, \tau) * G_{ij,k}(\underline{\xi}, \underline{x}, \tau, t) + F_j(\underline{\xi}, \tau) * G_{ij}(\underline{\xi}, \underline{x}, \tau, t) \tag{1.11}$$

where the displacement u in the $i-th$ direction is given by the convolution between the moment tensor components with the gradient of the Green's functions plus the convolution of the single force components with Green's functions. The indices i, j, k are the components of the different tensors and the comma represents the spatial derivative. Thus, we need observations, i.e. seismograms, and an accurate representation of the Green's functions to obtain, through inversion methods, the components of the moment tensor (MT) and the components of the single force (SF), if applicable. The latter is the representation of the seismic source as a unique force, related to a mass movement within the crust.

Aki and Richards (2002) state that regardless of the mathematical representation of the source, i.e. MT or SF, the radiation produced is separated in the

near-field and far-field. Thus, depending on the distance between source and station, the seismic wavefield has different properties e.g. amplitudes, waveforms and radiation patterns, therefore, this information has to be included in the Green's functions. The same authors describe the near-field as permanent deformations at the stations due to the proximity of the fault rupture, and its influence is dominant up to a distance of a single wavelength λ. For tectonic earthquakes, the influence of the near-field effect is small, mainly due to the depth of the events > 5 km and the large epicentral distance compared to the wavelength. However, in volcanic environments, the near-field effect is more likely to be detected since the hypocentres are shallow and the seismic stations are located in the vicinity of the crater, together with waveforms dominated by low-frequency signals. The area of influence of the near field can vary due to other effects, such as the radiation pattern of the source. Some directions show no far-field amplitude, thus, the near-field will be dominant even at distances $> \lambda$.

The selection of seismic stations used for the MT inversion is of major importance and the results are strongly dependent on the network configuration, especially the coverage on the focal sphere. Lanza and Waite (2018a) studied the performance of different synthetic networks on non-linear moment tensor inversions and conclude that moment tensor components can be estimated accurately with at least 8 stations, and there is no significant improvement by using as much as 40 stations. In contrast, the source time function can be estimated very well with at least 4 stations. We are interested in the performance of different networks to retrieve the magnitudes and moment tensor components by analysing real networks and synthetic ones. We include cases for local and regional networks, and also, cases when the fault is bigger than the source-receiver distance.

The point source approximation for MT inversions discussed here is valid only when the source is small compared to the wavelengths of the seismic radiation, $L \ll \lambda$ (Aki and Richards, 2002), with L being the length of the fault. For bigger earthquakes, a superposition of point sources is needed to explain the geometry and dynamics of the seismic event i.e. an extended source model. Eq. 1.10 shows that M_0 and A are linearly dependent if the area and the slip have constant orientations for all sources, i.e. the moment tensors have to be proportional ($M_1 = \alpha M_2$, with $\alpha > 0$). In general, the contributions on the radiation

from each source can interfere destructively, therefore, the estimation of magnitudes from superposed sources can be misleading (Contreras-Arratia and Neuberg, 2019).

1.3 Extended sources

As we described in the previous section, the description of an earthquake by a single point source is valid only when the condition $L \ll \lambda$ is satisfied. However, there are other important cases where the point source approximation is not a valid approximation, such as,

- If the planar area is big and the distribution of slip is not homogeneous.
- Whenever the slip on the fault changes direction, even if the source geometry is fixed and small.
- If the area changes orientation i.e. non-planar shapes, even if the source geometry is small.

The use of extended sources for large earthquakes has been extensively studied theoretically (Ben-Menahem, 1962; Olson and Apsel, 1982) and applied to real case scenarios with planar (Hayes, 2017) and non-planar faults (Cruz-Atienza and Virieux, 2004). This is a good approximation when faults are hundreds of kilometres long. This approach is also followed in geodetic problems, when a fault is discretised and deformation is calculated as the superposition of different area elements in volcanic environments (Gudmundsson et al., 2016; Masterlark and Tung, 2017) and for tectonic earthquakes (SuiTung and Lo, 2018).

In this thesis, we study ring faults in volcanic environments with different radius (R) using extended source models: conduits with $R \sim 20$ m and calderas with $R \sim 3.5$ km. Ring faults in conduits can be considered a very small source compared to the wavelength radiated, therefore, they tend to be studied by using a point source. However, the different strike angles of each point source used to model the ring lead to seismic interference, thus, the point source description is not directly applicable. The relationship between the amplitudes obtained at

seismic stations and the rupture area is non-linear. Moreover, the discrete nature of the fault causes diffraction, i.e. wave phenomena which change the properties of the wavefield that needs to be considered. The net radiation is in general very different from the radiation produced by a single point source (Contreras-Arratia and Neuberg, 2019) and further discussed in Chapter 2.

In order to represent a continuous source by a superposition of discrete sources, we need to understand the impact of the diffraction pattern. For any arrangement of discrete sources, which can be considered as a diffractor as a slit in optics, we observe that the amplitude pattern of waves is dependent on the angular position from each source. For ring sources, the amplitudes do not show a smooth decay, but a sinusoidal dependence, such as the shown in Fig. 1.5 as an example. The parameters which control this phenomenon are the maximum distance between point sources L, the wavelength λ and the source-receiver distance r, they are related as follows (Aki and Richards, 2002),

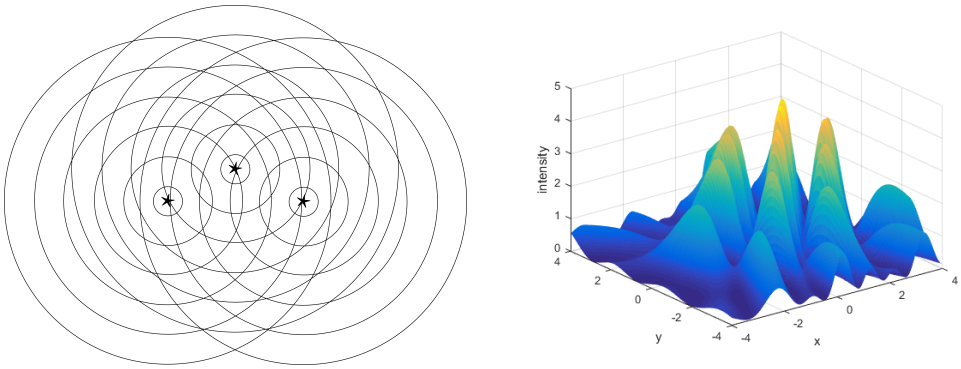

Figure 1.5: Schematic representation of more than two sources that act as diffractors. The amplitude pattern is sinusoidal rather than a smooth decay with distance.

$$L^2 \ll \frac{1}{2}\lambda r \tag{1.12}$$

if this condition is satisfied we can predict the diffraction pattern. This ensures that the point sources are close enough compared to the factor of the wavelength and the source-receiver distance. This means that all the seismic phases, near- and

far-field, produced by different point sources arrive at a station within the time Δt, no longer than 1/4 of the period T ($\Delta t < T/4$). The ring faults we study can be considered as diffractors and depending on the source-receiver distance we call them near-field diffraction (Fresnel) or far-field diffraction (Fraunhofer) (Aki and Richards, 2002). For stations which do not satisfy the condition 1.12 the seismograms display distorted waveforms as depicted in Fig. 1.6b. Nonetheless, they give important information about the extension and shape of the fault.

If it is necessary to describe the source as a point source, we can enforce the condition 1.12 by using a low-pass filter, which cut-off frequency depends on the distance source-receiver. Thus, the wavelength used for the MT inversions needs to be selected appropriately: the longer the size of the source, the longer the wavelength needed. In Fig. 1.6 we show two different cases of waveforms arriving at the station with the same period. The change in the shape of the net waveform produce inconsistencies in the MT returned when the condition 1.12 is not satisfied. We come back to this topic in Chapter 2.

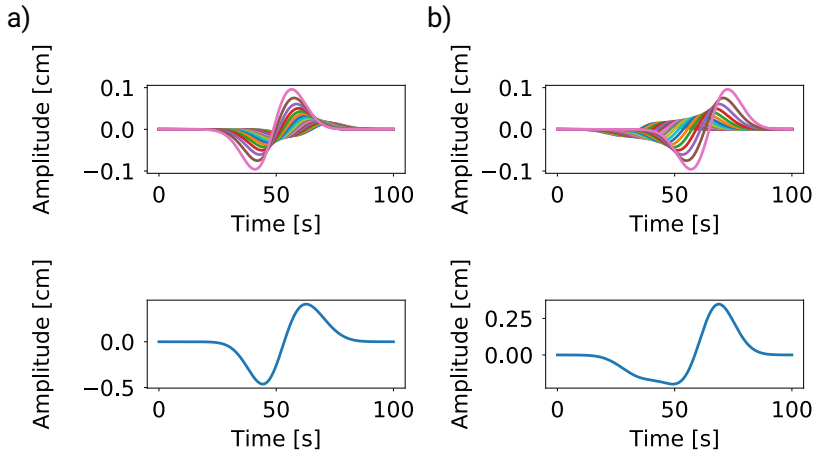

Figure 1.6: Superposition of different contributions to the net waveform. a) Coherent waves. b) Non-coherent waves, which produce misfits in posterior calculations (superposition lose the shape).

1.4 Ring faults in Volcanic Environments

As we stated in the previous section, the assumption of a planar fault is sometimes not accurate. There is increasing evidence that volcanoes around the world present faults which do not follow a planar geometry. For example, the fault creation in different stages of a caldera collapse (Acocella, 2007), solidified magma in eroded volcanoes (Tuffen et al., 2003) and physical rupture mechanisms within magma conduits (Iverson et al., 2006; Neuberg et al., 2006). Here we present the geological and physical background which allow us to link extended seismic sources and curved structures in volcanoes.

1.4.1 Conduits

We define a conduit as a narrow cylindrical body with a diameter of less than 100 m, in which magma can ascend from the reservoir and eventually erupt. For simplicity we consider a Newtonian fluid flow moving upwards (Fig. 1.7). We want to understand the conditions needed to observe brittle failure in magma, which gives us the basis to propose ring ruptures in conduits. We model the magma as a Newtonian fluid. Its constitutive relationship is given by (Collier and Neuberg, 2006),

$$\tau_{xy} = \eta\dot{\epsilon}_{xy} = \eta\partial_x v_y \tag{1.13}$$

where τ_{xy} are the shear components of the stress tensor, η is the magma viscosity, $\dot{\epsilon}_{xy}$ are the components of the strain rate tensor and $\partial_x v_y$ the velocity gradient or slope of the velocity profile. This equation provides the conditions needed for a Newtonian fluid to fail. If the strain rate is high enough to produce high shear stress that overcomes the strength of the fluid, we observe brittle behaviour with the corresponding generation of seismic waves (Collier and Neuberg, 2006; De Angelis and Henton, 2011; Neuberg et al., 2006; Okumura et al., 2010; Thomas and Neuberg, 2012).

We assume an episode of magma ascent in a conduit or pipe with constant viscosity (Poiseuille flow), the magma is faster at the centre of the pipe and the velocity tends to zero towards the edges. Considering a more realistic case, the

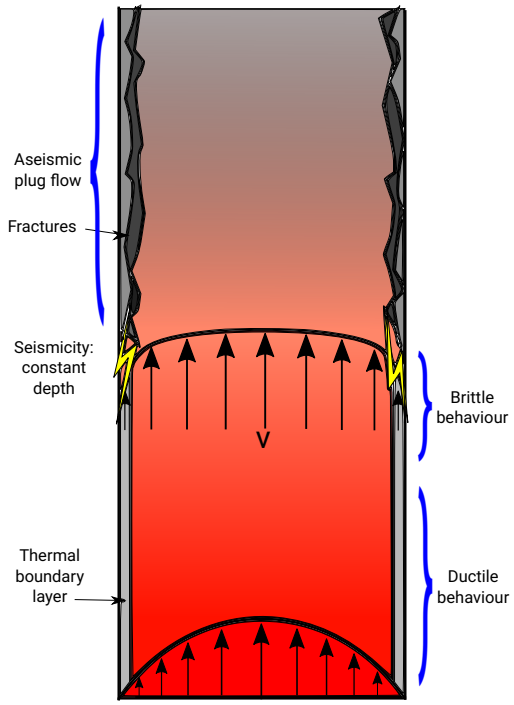

Figure 1.7: Schematic representation of magma ascent. Including potential seismic sources due to magma brittle behaviour.

flow depends on several factors (Marsden et al., 2019, and references therein), such as cooling effects due to the temperature of the surrounding rock (Collier and Neuberg, 2006), crystallisation modelled by a non-Newtonian fluid increasing the viscosity (Tsvetkova and Melnik, 2018), dehydration of the melt changing the gas content (Chevalier et al., 2017) and shear thinning, which is a non-linear mechanical behaviour of magma (Costa et al., 2009). In this case the parabolic velocity profile changes to a "plug flow" with maximum velocity at the centre and an abrupt decrease towards the edges (Fig. 1.7).

This slope in the velocity profile at the boundaries increases the value of strain rate for the plug flow and provides the highest values of strain rate ($\dot{\epsilon}_{xy}$) and the consequent increase in shear stress (τ_{xy}) . If this shear stress values overcome the strength of magma, brittle behaviour in the glass transition is observed (Neuberg et al., 2006). The strength of magma has been set as 10 MPa for rhyolitic magmas by Webb and Dingwell (1990) but recalculated to 1MPa by Marsden et al. (2019); Okumura et al. (2010).

This physical model for rupture in magma is postulated as responsible for the trigger of long-period (LP) and Hybrid seismicity (Goto, 1999; Neuberg et al.,

2006; Tuffen et al., 2003). This seismicity is non-destructive, repetitive and has a stationary source location (Neuberg et al., 2000, 2006). LP and Hybrid seismicity show a direct correlation with explosions and dome collapse, therefore, they can be used as a forecasting tool (Chouet, 1996; Chouet and Matoza, 2013; Miller et al., 1998). Several source models point to the influence of fluids upon the long-period signal, either a huge and narrow crack filled by gases (Chouet, 1996; Chouet and Matoza, 2013) or a conduit filled with magma (Goto, 1999; Neuberg, 2000; Neuberg et al., 2006; Tuffen et al., 2003) produce slow waves travelling across the body, in a process similar to resonance (Ferrazzini and Aki, 1987). Another mechanism to explain the long-period signals was provided by Bean et al. (2014), in which LP signals are produced by a simple tectonic earthquake in a very weak elastic medium, with no influence of fluids.

In this thesis, we are interested in the trigger of LP and Hybrid events, the rupture that provides the energy for the long-period oscillation. The only model which links the occurrence of this kind of events and magma extrusion is the conduit filled with magma proposed by Neuberg et al. (2006). The same authors proposed the relationship between the occurrence of this seismicity with large strain rates within the magma on the move. It has been reported (Green and Neuberg, 2006; Hammer and Neuberg, 2009; Miller et al., 1998) that swarms of LF events culminate their occurrence with a dome collapse event supporting the model proposed by Neuberg et al. (2006). The seismic radiation considers a small part of the radiation produced by rupture of magma inside the conduit is emitted as P waves, while most of the energy is trapped within the magma conduit, contributing to the propagation of slow waves. We propose the following rupture models:

- Simple plane: rupturing one side of a dyke.
- Two parallel planes: both sides of a dyke.
- Partial-ring rupture: a partial rupture in a conduit.
- Full-ring rupture: the full circumference in a conduit.

Understanding the radiation of the last three non-planar faults allow us to accurately constrain the source parameters. For example, a non-linear relationship

is valid between the area of rupture in a ring fault and the amplitudes observed, contrasting the linear relationship for planar faults. Additionally, differences in the waveforms and polarisations observed which are not predicted by the planar source theory, influence the slip history at the fault.

1.4.2 Calderas

A caldera is a large volcanic structure formed after a collapse of a volcanic edifice which had lost its sustain after the magma chamber was emptied (Sigurdsson et al., 2015). By definition, a caldera is formed by systems of ring faults, which have different properties depending on the caldera's roof aspect ratio $height/width$. For high aspect ratios, the caldera is deep and narrow, for low aspect ratios, the caldera is wide and shallow (Roche et al., 2000). The same author performed analogue experiments and found that high aspect ratio calderas collapse breaking the roof into pieces since faults are created at the rims and also within the circumference, they show piece-meal collapse. On the other hand, low aspect ratio calderas on which we are focusing, are likely to behave as a whole block collapsing, activating faults only at the rims e.g. piston-like (full-ring) and trapdoor (partial-ring). Acocella (2007) defined four stages of evolution for such a collapse (Fig. 1.8),

- Stage 1: down-sag collapse with no fracturing.
- Stage 2: reverse ring faults formed.
- Stage 3: peripheral down-sag with reverse faulting.
- Stage 4: peripheral normal ring fault development and faulting.

By studying the seismicity of a caldera, i.e. hypocentres and MT solutions, we can infer the state of evolution of the collapse. Moreover, the study of the complete seismic sequence gives information about the cumulative seismic moment during the collapse, which can be compared with the geodetic moment, calculated from InSAR measurements (Gudmundsson et al., 2016), among other methods. It is important to note that stages 1 and 3 produce plastic deformation, which can be detected by geodetic methods, but not by seismic methods, hence, the values

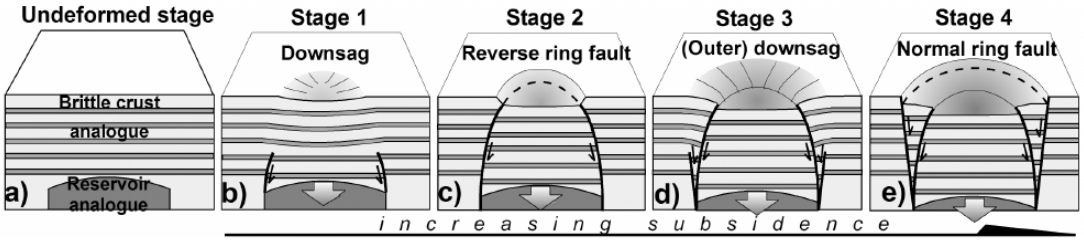

Figure 1.8: Schematic representation of a caldera during evolution stages, from 1 to 4. Arrows indicate shear movements and potential seismic sources (Adapted from Acocella (2007)).

will not match. Finally, the cumulative seismic moment might be underestimated if only classic seismicity (VT) is considered, and newly discovered earthquake processes are not taken into account, e.g. slow earthquakes (Brooks et al., 2006) on lubricated faults (Brodsky and Kanamori, 2001) or seismic creeping registered as a tremor-like seismic signal (Rubin et al., 1999).

1.5 Project Aims

In this thesis, we study the effect of the curvature in non-planar faults with ideal shapes and realistic sizes. We hypothesise that radiation produced by planar and non-planar sources is intrinsically different, therefore planar fault theory cannot be directly applied to curved cases. However, understanding seismological clues which support non-planar ruptures can help us to correct the results returned by standard methods based on a point source theory.

Specific objectives for this thesis are:

- Apply extended source models for non-planar faults, considering potential uses and limitations.
- Find a methodology to correct results obtained using a point source approach when the actual rupture is not a planar source.

- Study and quantify the performance of different seismic networks while inverting moment tensor parameters, considering not only azimuthal coverage but also epicentral distance.
- Find a relationship between magma extrusion rates and slip at the fault for low-frequency events at Soufrière Hills volcano, Montserrat, West Indies.
- Understand the differences between complex and planar rupture models and correct previous estimations of the cumulative seismic moment for the caldera collapse at Bárðarbunga, Iceland.

1.6 Outline

After setting the background in this chapter, we continue in Chapter 2 with the creation of synthetic seismograms which contain information about the seismic interference produced by these extended sources and evaluate the seismological considerations we take into account. We study the main features of radiation for cases of silicic volcanoes and calderas, understanding how the amplitudes, polarisations and waveforms change. In Chapter 3 we apply these models to low-frequency trigger signals and compare the corresponding slips retrieved with magma ascent at Soufrière Hills. In Chapter 4 we re-calculate the cumulative seismic moment, previously calculated by Gudmundsson et al. (2016) and Ágústsdóttir et al. (2019), at Bárðarbunga during the 2014 caldera collapse and discuss seismic network configuration dependence. Finally, in Chapter 5 we discuss implications of applying this approach to point source moment tensor inversions and corrections needed on moment tensor results in order to obtain real seismic source parameters. These include cumulative displacements at the fault which are translated into magma ascent or subsidence of a caldera.

Chapter 2

Complex seismic sources in volcanic environments: Radiation modelling and moment tensor inversions

Now that we have reviewed the main properties and considerations needed to apply an extended source approach to describe the seismic source, we continue with the geometrical description in 3-D adopted. Additionally, we test two approaches in order to understand the main properties of the radiation of complex sources with a radius of tens of meters. The first approach considers the superposition of radiation patterns, which assumes all the source contributions arrive at the station at the same time. Subsequently, we test synthetic seismograms which consider travel time differences and therefore different arrivals. These approaches give us information on first arrival polarisations, waveforms and amplitudes expected. Furthermore, the synthetics are subjected to moment tensor inversions (MTI) in order to understand how software interprets a complex source when assuming a point source. This chapter is based on the article I published with Jurgen Neuberg, Contreras-Arratia, R. and Neuberg, J.W., 2019. Complex seismic sources in volcanic environments: Radiation modelling and moment tensor inversions. Journal of Volcanology and Geothermal Research, 381, pp.262-272.

2.1 Introduction

At silicic volcanoes, dome collapse events and explosions are often preceded by increased activity of long-period earthquake swarms (LP events). Therefore, this type of seismicity can be used as a forecasting tool (Chouet, 1996). LP events comprise a high-frequency onset (trigger) which provides the energy input for long-period oscillations trapped in a fluid-filled structure to occur (Ferrazzini and Aki, 1987; Neuberg et al., 2006). The detailed interpretation of such low-frequency seismic events often points to source models comprising the repeated expansion and compression of steam-filled, or ash-laden, sub-horizontal cracks explaining both the dominant frequency content and the seismic radiation pattern (Molina et al., 2004). While such models explain the low-frequency records adequately, the trigger source geometry is often geologically oversimplified e.g. simple planar faults. Furthermore, they fail to incorporate the magma movement, ignoring the simultaneous observation of magma extrusion. The adoption of more realistic, alternative seismic source mechanisms based on brittle magma fracture (Neuberg et al., 2006) or stick-slip motion (Iverson et al., 2006) at the conduit or dyke margins during magma ascent has been the subject of experimental and numerical endeavours in which more complex source mechanisms have been suggested. For example, a conical fault (Ekström, 1994; Nettles and Ekström, 1998; Shuler et al., 2013a,b) observed at regional and teleseismic distances was linked to a Compensated Linear Vector Dipole (CLVD) at a point source located at the centre of the cone.

Usually, seismic moment tensor (MT) inversions are the essential next step in shedding more light on the physical rupture processes involved. Classic inversions for a planar fault consider the fault size, orientation, and amount of slip as the main contributing factors controlling seismic amplitude patterns. For shear failure along a single fault plane the seismic moment M_0 is directly proportional to both the area on which slip occurs and the amount of slip (Aki and Richards, 2002), however, this might no longer apply for other fault geometries. Earthquake sources in volcanic areas have been studied by several authors, obtaining the full range of possible MT solutions. Besides double couple (DC) solutions (Ágústsdóttir et al., 2016; White et al., 2011), mass-movement related sources have been observed, such as explosions/implosions, (Chouet et al., 2003; Kumagai et al., 2011; Ruiz et al.,

2006), exploding/imploding cracks (Mildon et al., 2016), CLVD (Shuler et al., 2013a,b) and single forces (Richardson and Waite, 2013). All these studies use the fundamental assumption behind classic MT inversions i.e. they are based on planar surface geometry. The application to more complex seismic sources has so far been inconclusive.

Here, we advance existing source models from commonly used point sources on single fault planes, including the representation of a complex fault by a single point source, to spatially extended, more complex structures modelled by a combination of sources on the dyke margins. We consider five complex ruptures: a dyke rupture, three cases of failure along partial ring rupture and full ring rupture (Fig. 2.1). The seismic triggering is explained through the rupture of highly viscous magma that succumbs to high strain rates at the conduit walls (Neuberg et al., 2006), or as a friction-controlled stick-slip motion at the conduit margins (Iverson et al., 2006). Here, we solve the forward problem and obtain the main features of seismic radiation patterns produced by these alternative source mechanisms in comparison to a single DC and CLVD. We found significant changes in amplitude, polarisation, and waveform (observation parameters) which have important implications when seismic data are interpreted in terms of magma movement e.g. slip history on the fault or maximum amplitude of slip. These implications become evident when solving the inverse problem.

2.2 Modelling complex sources by superposition of point sources

In order to represent these complex sources, we superimpose simultaneously acting DC sources on "patches" arranged along with the shape of non-planar narrow ruptures. Each point source is represented by a vertical DC moment tensor with rake and azimuth angles varying depending on the shape, upward movement is always in the inner part of the structure representing magma ascent. For the first time, we model slip on: (i) a dyke fault with 2 patches, (ii) 1/4-ring with 9 patches, (iii) 1/2-ring with 18 patches, (iv) 3/4-ring with 27 patches and (v) a full-ring with 36 patches. The number of patches was chosen to satisfy the sampling theorem

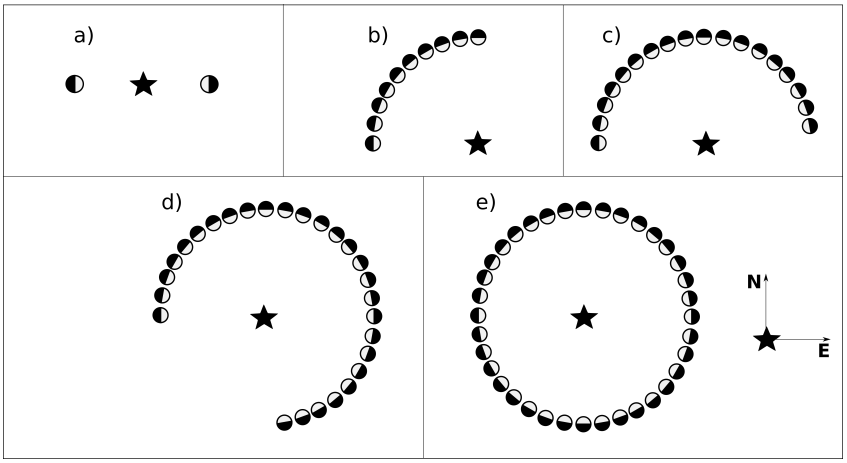

Figure 2.1: The five extended sources studied with focal mechanisms for each point source in plan view: a) Dyke fault, comprising two opposed DC. b) 1/4-ring fault, comprising 9 point sources. c) 1/2-ring fault, consisting of 18 point sources. d) 3/4-ring fault, 27 point sources. e) Full-ring fault, 36 point sources. Each point source is acting within an area patch. The star represents the reference point for each case.

using the velocity of the medium and the frequency of the radiation. Hence, for narrow structures considered here, the contributions of all sources arrive in a short time interval compared to the period.

Since our complex seismic sources are represented by several individual sources with different locations, the spherical coordinates $(r_{ij}, \theta_{ij}, \phi_{ij})$ (observation parameters, i.e. distance, take-off angle and azimuth, respectively) from the j-th source to the i-th seismic station vary slightly. For each complex source, we define a reference point (star in Figs. 3.1 and 3.2) and find analytical expressions linking the observation parameters between each single point source and a seismic station $(r_{ij}, \theta_{ij}, \phi_{ij})$ to the equivalent observation parameters between the reference point of the entire complex source and this particular station $(r, \theta, \phi)_i$, as shown in Fig. 2.2,

$$r_{ij} = \sqrt{r^2 + R^2 + 2rR\cos\theta\cos\phi}$$

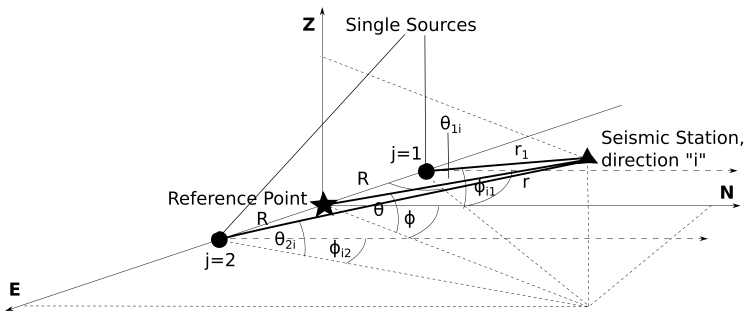

Figure 2.2: Coordinate system used showing the reference point (star) for a dyke comprising two DC sources (dots j=1,2) and a seismic station (triangle). The observation parameters related to the seismic source are a function of the equivalent parameters related to the reference point, i.e. $r_1 = r_1(r, \theta, \phi)$, $\theta_1 = \theta_1(r, \theta, \phi)$, $\phi_1 = \phi_1(r, \theta, \phi)$, $r_2 = r_2(r, \theta, \phi)$, $\theta_2 = \theta_2(r, \theta, \phi)$ and $\phi_2 = \phi_2(r, \theta, \phi)$.

$$\theta_{ij} = \arctan\left(\frac{r\sin\theta}{\sqrt{(r\cos\theta)^2 + R^2 + 2rR\cos\theta\cos\phi}}\right)$$

$$\phi_{ij} = \arctan\left(\frac{\sin\phi}{\cos\phi + \dfrac{R}{r\cos\theta}}\right). \tag{2.1}$$

We can estimate the P-wave Radiation Pattern for a single DC in a spatial grid (θ, ϕ), using $a_i = \sin 2\theta_{ij} \cos\phi_{ij}$ which gives us the relative amplitudes produced by the j-th source at a certain direction $(\phi, \theta)_i$. Then, we sum all contributions produced by each source in angle increments of δ_r [°] in order to span all space and calculate the net amplitude expected for P-waves in all directions. We assume that all the phases from different point sources arrive simultaneously at the station i.e. we use a long-wavelength approximation since the maximum distance between sources $2R$ is very small compared to the source-station distance r. Integration steps and boundaries depend on the shape of the source and are shown in Table 2.1. Note that all cases considered in this study use $R << r$, where $R = 20$ m represents a typical size for a narrow conduit geometry. The modelling of the seismic wavefield of larger volcanic structures, e.g. calderas, where $R \sim r$, show

that the radiation properties will have different characteristics and their analysis is developed in Chapter 4.

Source	Lower boundary for summation, ϕ_1	Upper boundary for summation, ϕ_N	No. of Point Sources (N)
Dyke	0°	180°	2
1/4-ring	90°	180°	9
1/2-ring	0°	180°	18
3/4-ring	−90°	180°	27
Full-ring	0°	0°	36

Table 2.1: Parameters for numerical integration.

We calculate the net Radiation Pattern for M sources assuming all the contributions arrive at the same time (no time dependency included),

$$A_i = \sum_{j=1}^{M} \sin(2\theta_{ij}) \cos(\phi_{ij}) \quad \text{, with } \theta_{ij} = \theta_j + i\delta_r \text{ and } \phi_{ij} = \phi_j + i\delta_r \tag{2.2}$$

where A_i is the relative P-wave amplitude compared to a normalised single DC, N the number of directions (ϕ, θ) considered and δ_r denotes the angular increments in space.

However, as we mentioned previously, this integration process does not consider travel time differences caused by the slight differences in source-receiver distances for different sources at the same station. To take this effect into account, we use the software QSEIS (Wang, 1999) to produce Green's functions and synthetic signals in a homogeneous half-space in order to obtain the direct influence from the source and minimise path effects. This software uses a simple numerical method to make the fundamental displacement at each station orthonormal. It avoids well-known numerical instabilities of the solutions when calculating Green functions using Thompson-Haskell propagator algorithm for waves that become evanescent. We had tested the the synthetic seismograms returned by using a set of different sources and analyse the amplitudes and polarisations at different stations, returning consistent results with the theory.

The "Recording stations" are located in circular grids in every 500 m epicentral distance, up to 5 km and every 30° azimuth, however, for the moment tensor inversions we use 3 concentric rings at 1, 2 and 3 km (Fig. 2.3). Hence, we have 120 stations sampling at a frequency of 100 Hz and we use 36 for inversion. The parameters for modelling are shown in Table 2.2 and an example of input file is shown in Appendix A. We obtain synthetic seismograms from each contributing DC source using values for the observation parameters given in Eq. 2.1 and the source-station configuration. Next, we sum up all the waveforms recorded at each station to obtain the net waveform produced. An example of the waveforms produced by the Dyke source is shown in Fig.2.4 and 2.5

Later, we quantify their main features such as the amplitude of first arrivals, polarisation and the waveform itself. We compare them with the ones produced by a simple DC and a Compensated Linear Vector Dipole (CLVD) for comparison, both of magnitude $M_{\mathrm{W}} = 2.2$. Then, we obtain amplitudes generated by the ruptures shown in Fig. 2.1. In order to compare the "efficiency" of all rupture models, we need to calculate the seismic radiation produced by the same areas, slips and shear coefficient with different shapes. To achieve this we normalise the waveforms by the number of sources/patches acting in each case.

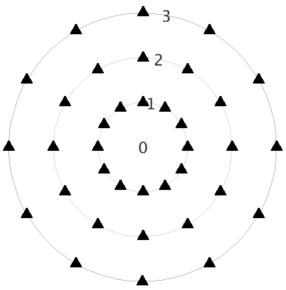

Figure 2.3: "Recording stations" used for inversion in this study, located in 3 rings, 1-3 km from the rupture models at the centre.

Using the datasets created in the forward modelling for the five sources listed above, we perform "classic" moment tensor inversions under the assumption of a point source on a simple fault plane, which is the most common approach in volcano seismology. The inversions were carried out using the Kinematic Waveform

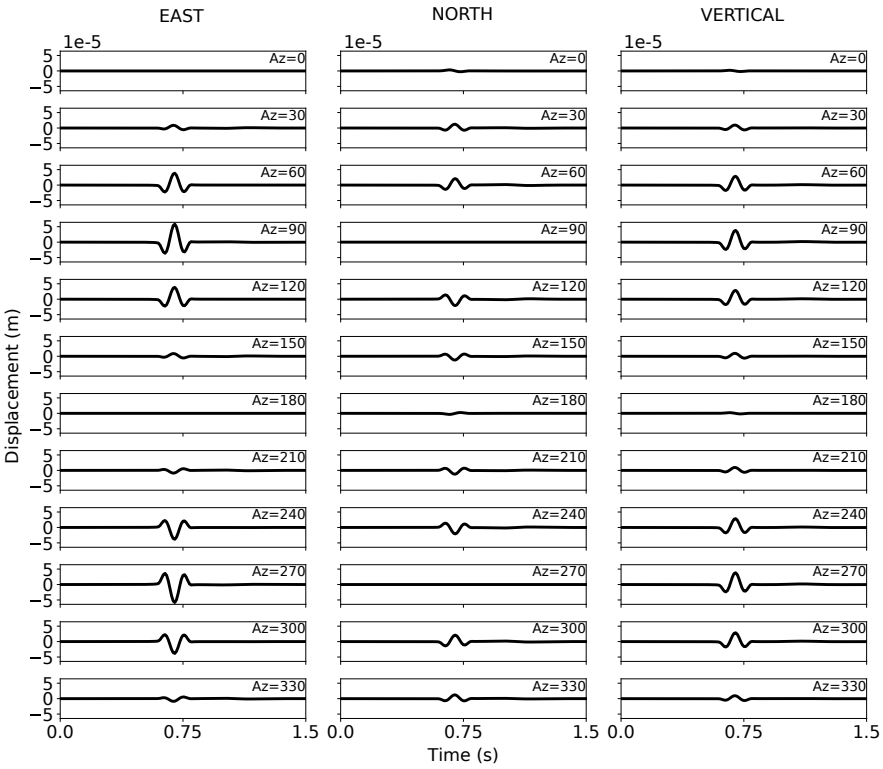

Figure 2.4: Example of the seismograms obtained for the Dyke source at constant epicentral distance of 1.5 km. Each column show different seismogram components. Each row show different azimuth angles of the stations.

V_p	q_p	V_s	q_s	R_{dyke}	R_{ring}	M_{w}	Depth Event	Frequency
3000 m/s	1000	1732 m/s	1	10 m	20 m	2.2	1 km	5 Hz

Table 2.2: Parameters for forward modelling.

Inversion Tools (KIWI) (Cesca et al., 2010) which uses the Levenberg-Marquardt method to solve the full waveform moment tensor inversion (Moré, 1978). The solution is retrieved in two steps, the first in the frequency domain, where the best source geometry is calculated, later, the polarisations are set by using the time series. We tested the solutions provided by KIWI for filtered synthetic seismograms of simple point sources previously generated using QSEIS and compared with the radiation patterns, obtaining good results. The main parameters to set are the

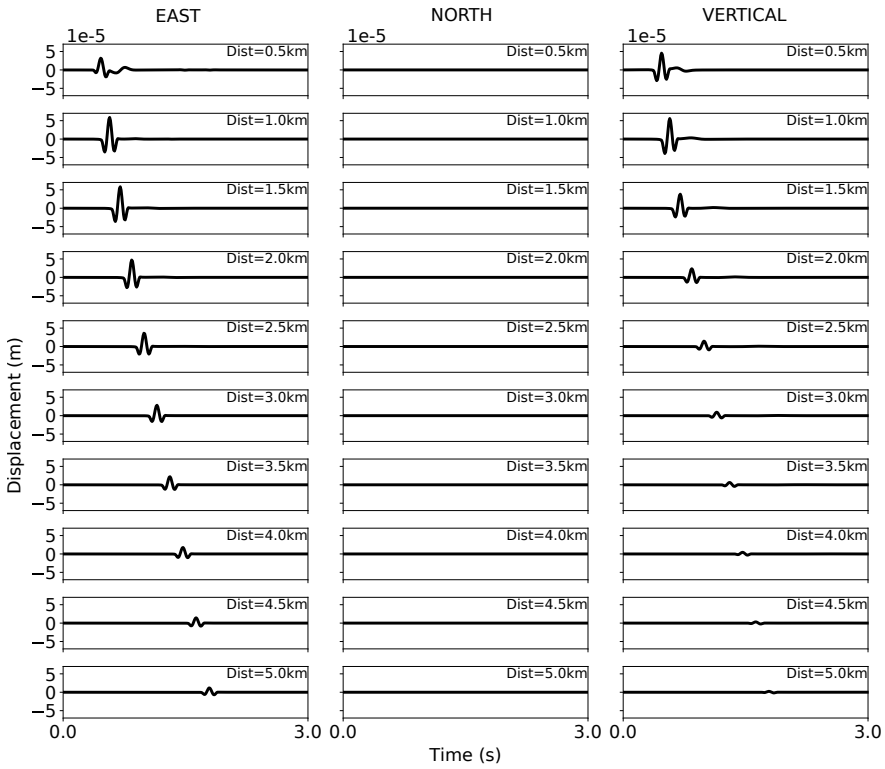

Figure 2.5: Example of the seismograms obtained for the Dyke source at constant azimuth of 90°. Each column show different seismogram components. Each row show different epicentral distances of the stations.

frequency band and the seismic phases to consider, for our case, we consider them all, one example of an input file is shown in Appendix A. The software successfully retrieves the source used as input, providing the mathematical representation of a full moment tensor (matrix) comprising the isotropic and deviatoric components, the latter of which is further decomposed into a double couple (DC) and a compensated linear vector dipole (CLVD).

We allow single force components to be calculated along with moment tensor components using the software package VOLPIS (Cesca and Dahm, 2008), which uses the method proposed by Vasco (1989) to obtain source time functions (STF) by using the singular value decomposition scheme. We tested the solutions returned and compare the amplitudes of the STF with the solutions provided by KIWI and the synthetic source. Additionally, an extensive testing scheme was

done by Sindija and Neuberg (2019) obtaining a good performance for different double couple sources and a sufficiently dense seismic network. The software returns STF for the 9 components, i.e. the 6 moment tensor components + 3 single force components. Here we find an "*apparent solution*" by applying standard moment tensor inversion techniques to a curved, more complex fault using a band-pass filter between 0.1 - 0.5 Hz. These apparent solutions can now be compared to real cases (Chapter 3 and 4).

Finally, we want to explore the effect of the radius of curvature in the radiation, specifically, in the maximum amplitude obtained in a particular station. We model 1/4-ring ruptures with different radius of curvature with the same location for the central point. The recording station is located 6 km away forming a perpendicular line to the tangent of the curved surface at the central point of the fault (Fig. 2.6a). These results are analysed and discussed in Section 2.5.3.

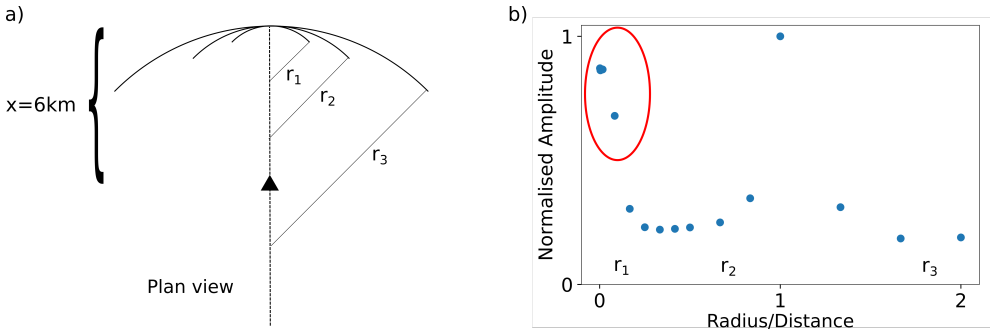

Figure 2.6: a) Geometries used to quantify the curvature dependence on amplitudes, station fixed at 6 km while the radius of curvature varies. b) Normalised amplitudes for different curvatures are smaller than a DC, except when the seismic station is located at the centre of the ring structure at $r = 6$ km and perfect focusing effect occurs. The circle shows the case of study for narrow dykes.

2.3 Coherence, travel time differences

In order to explore the range of parameters that satisfy the condition 1.12, we undertake an empirical study. We test 2 extended sources: a 7 km long N-S

planar rupture and a half-ring rupture with same size diameter (Fig. 2.7). All individual sources represent implosive isotropic moment tensors. We calculate the net waveform at a station located to the south of each source for different periods and rupture velocity. By performing a simple geometrical analysis we deduce that the condition 1.12 at a station in the same axis than the maximum distance between stations is met, then, it is met at all stations.

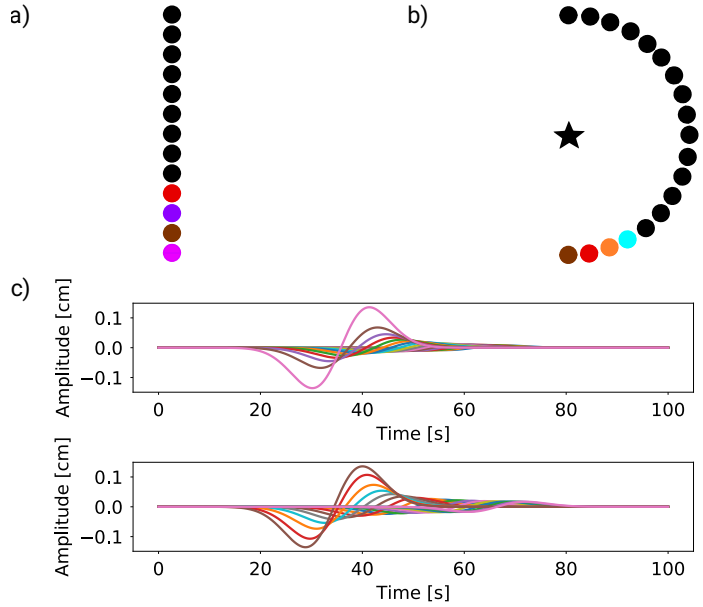

Figure 2.7: Geometry of synthetic experiment, a) Planar fault and b) Ring fault. Both faults represented as a superposition of point sources and colour-coded for the four largest amplitudes in each case. The rupture is receding from the station. c) Waveforms produced by each implosive point source from: (up) a planar source. (down) a ring source. Note the differences in the second-highest waveform for each case, following the colours shown in panel a) and b). This is due to differences in the travel paths for each source.

To model the net waveforms we created a simple script which calculate the travel time differences for each contribution and superpose the wavelets considering also the geometric spreading. Besides the geometrical parameters already mentioned, the input values used are: the frequency of the wave, the velocity of the medium (acoustic) and the rupture velocity,

First, we calculate for plane and ring faults the waveforms produced by ruptures propagating to the north (receding from the station) and south (approaching to the station) with an average rupture velocity of 1 km/s. After testing several wavelets for different cut-off frequencies (frequency of the source time function), we show results for 0.02 Hz, 0.1 Hz and 1 Hz. We observe three different cases of superposition: coherent, non-coherent and independent superposition. The coherent superposition is characterised by a waveform similar to the individual contributions regardless of the spectral content, which can shift due to the Doppler effect, e.g. Fig. 2.8 and 2.9. The non-coherent superposition is observed when the wavelength is too short under the conditions of source size and rupture velocity, in this case, the waveform is lost and it can be considered to be an indicator of an extended diffractor (source) as defined in Section 1.3 (Figs. 2.10 and 2.11). In Figs. 2.12 and 2.13 we show the case when all individual contributions are independent and they appear as individual earthquakes. The latter case was performed with a slower rupture velocity to exaggerate the effect of individual events.

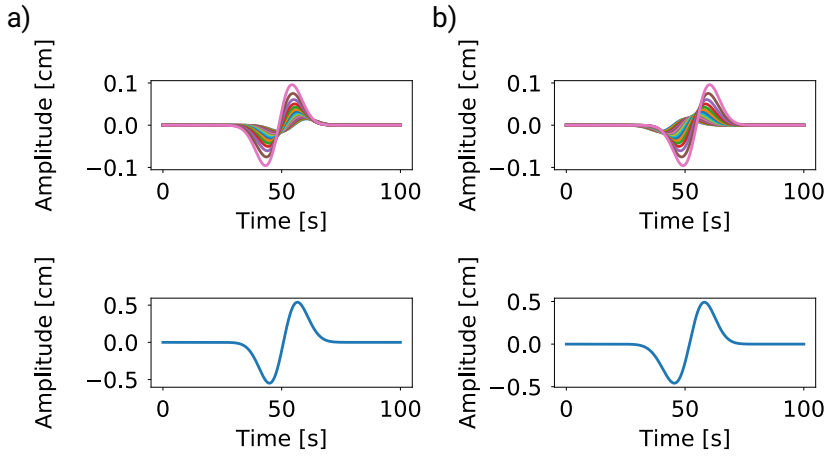

Figure 2.8: (Up) individual point source contributions at the station and (down) the net waveform produced by a planar fault for long-period waves, when coherence is achieved. a) Rupture approaching to the station. b) Rupture receding from the station.

In general, the coherence is achieved with long wavelengths, our synthetic tests are all coherent when we use a wave frequency of 0.02 Hz, however, we might be

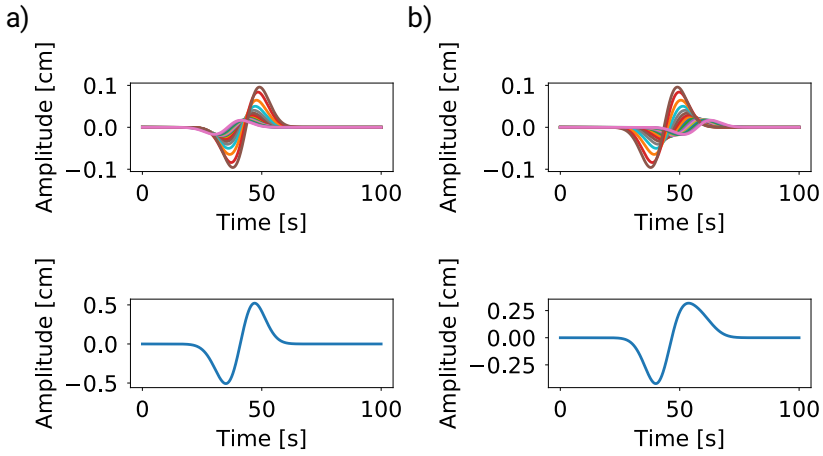

Figure 2.9: (Up) individual point source contributions at the station and (down) the net waveform produced by a half-ring fault for long-period waves, when coherence is achieved. a) Rupture approaching to the station. b) Rupture receding from the station.

interested in wave phenomena occurring at higher frequencies. To observe these effects we include shorter periods in the analysis, unstable diffraction patterns will be recorded and source parameter estimations cannot be applied. Nevertheless, these signals provide important information to support extended source ruptures. It is also important to note that the rupture velocity has the biggest impact on the coherence, in general, slower ruptures implies less coherence.

Another important aspect regarding the coherent waves is the evidence of the Doppler effect for caldera size ruptures, which cannot be identified for small ruptures. The maximum frequency observed in all cases is the same, regardless whether the rupture is receding or approaching. However, the overall frequency content is shifted towards higher frequencies when the rupture is approaching, as it is expected. This effect is stronger for ring ruptures (Fig. 2.14).

2.4 Coherence condition for propagating ruptures

In this section we establish a mathematical condition for the inclusion of the rupture velocity in the treatment of coherence. We study the relationship between

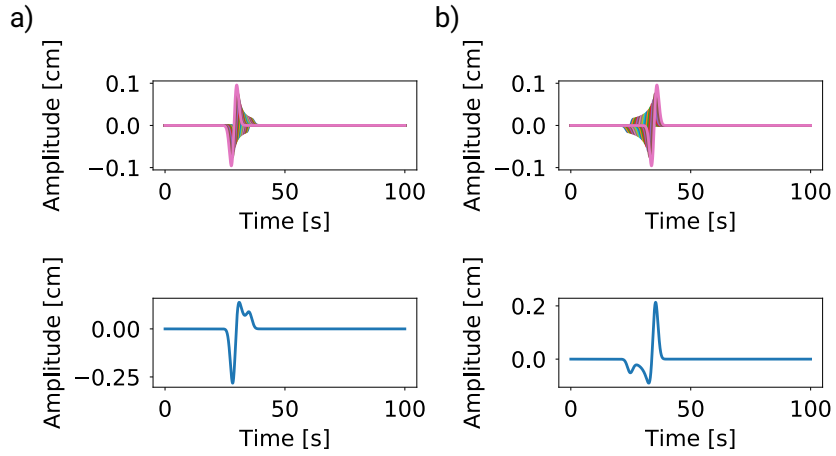

Figure 2.10: (Up) individual point source contributions at the station and (down) the net waveform produced by a planar fault when coherence is not achieved. This means that if we perform a MT inversion, it will return unrealistic results, we cannot treat the source as a point source. The maximum difference in time arrivals from two point sources is longer than the quarter of the period, i.e. the condition $\Delta t < T/4$ is not satisfied. a) Rupture approaching to the station. b) Rupture receding from the station.

wavelength, fault size and rupture velocity in time. Empirically we observe that coherence is achieved when the travel time differences between contributions are not longer than a quarter the value of the period T. We consider the time differences due to rupture propagation $t_{\text{offset}} = t_{\text{last}} - t_{\text{first}}$, defined as the difference between the arrival times of the last and the first contribution. In addition, we consider the time taken by a wave to travel along the fault t_{L}. Mathematically,

$$\begin{aligned} |t_{\text{L}} + t_{\text{offset}}| &< \frac{T}{4} \\ \left|\frac{d\text{max}}{v} + t_{\text{offset}}\right| &< \frac{T}{4} \end{aligned}$$

replacing the values for a rupture size of 7 km and both wave velocities $v_{\text{P}} = 4500$ m/s and $v_{\text{S}} = 2600$ m/s, we obtain the inequalities,

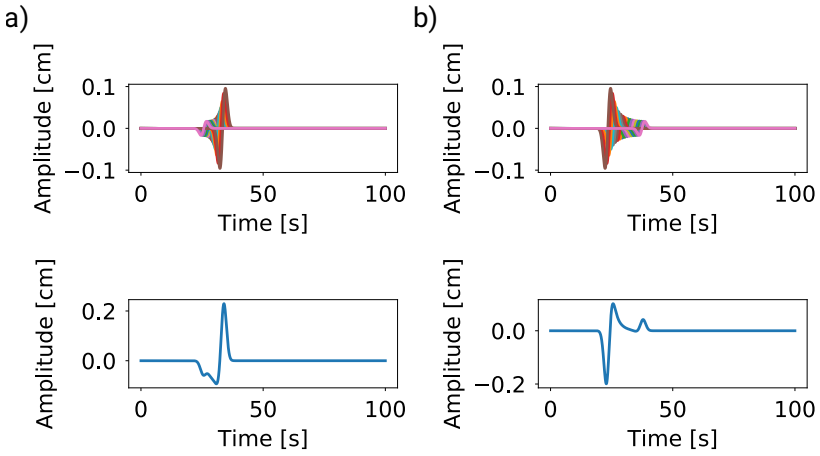

Figure 2.11: (Up) individual point source contributions at the station and (down) the net waveform produced by a ring fault when coherence is not achieved. This means that if we perform a MT inversion, it will return unrealistic results, we cannot treat the source as a point source. The maximum difference in time arrivals from two point sources is longer than the quarter of the period, i.e. the condition $\Delta t < T/4$ is not satisfied. a) Rupture approaching to the station. b) Rupture receding from the station.

$$\begin{aligned} \left|\frac{d_{\max}}{v} + t_{\text{offset}}\right| &< \frac{T}{4} \\ \left|\frac{7000}{4500} + t_{\text{offset}}\right| &< \frac{T}{4} \qquad \text{for P wave} \\ \left|\frac{7000}{2600} + t_{\text{offset}}\right| &< \frac{T}{4} \qquad \text{for S wave} \end{aligned} \tag{2.3}$$

where we can obtain the values accepted for the period T as a function of the t_{offset} to ensure coherence, the latter can be positive i.e. rupture receding or negative i.e. rupture approaching. The inequalities for P and S phases are shown in Fig. 2.15.

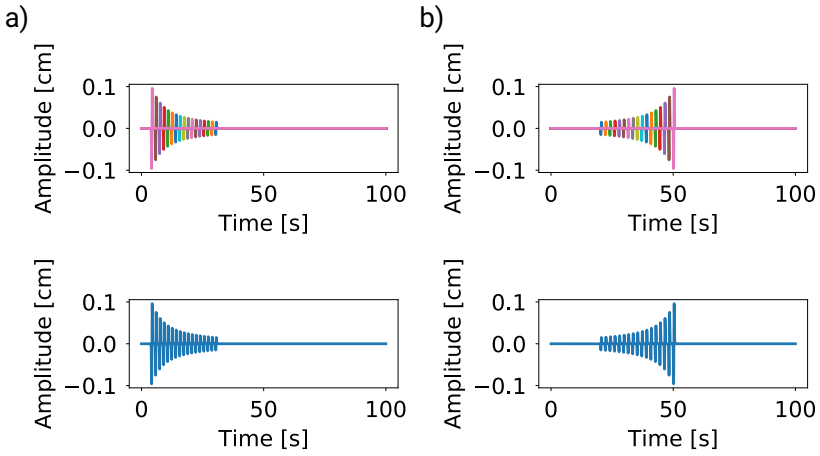

Figure 2.12: (Up) individual point source contributions at the station and (down) the net waveform produced by a planar fault when individual contributions are independent. Moment tensor inversions performed with this data will retrieve the source parameters of each contribution separately. The maximum difference in time arrivals from two point sources is actually longer than the period of the wave, therefore, all contributions are independent. a) Rupture approaching to the station. b) Rupture receding from the station.

2.5 Results

2.5.1 Seismic radiation patterns and amplitudes

In this section, we calculate the main features of the seismic radiation pattern produced by the complex-shaped faults shown in Fig. 2.1. These are calculated as described in the previous section using Eqs. 2.1 and parameters in Table 2.1. If the dimension of the complex source is small compared to the seismic wavelength and, therefore, the differential travel times are negligible, we can obtain an estimation of the radiation pattern assuming simultaneously arriving P-waves at a single station, e.g. at regional and teleseismic distances. On the other hand, when travel time differences between sources are considered, corresponding to a short wavelength approximation, the radiation can be affected. For comparison, in Fig. 2.16a and b, we show the radiation patterns, polarisations at the surface, waveforms and focal mechanisms for a vertical DC and a vertical CLVD in the far-field, respectively.

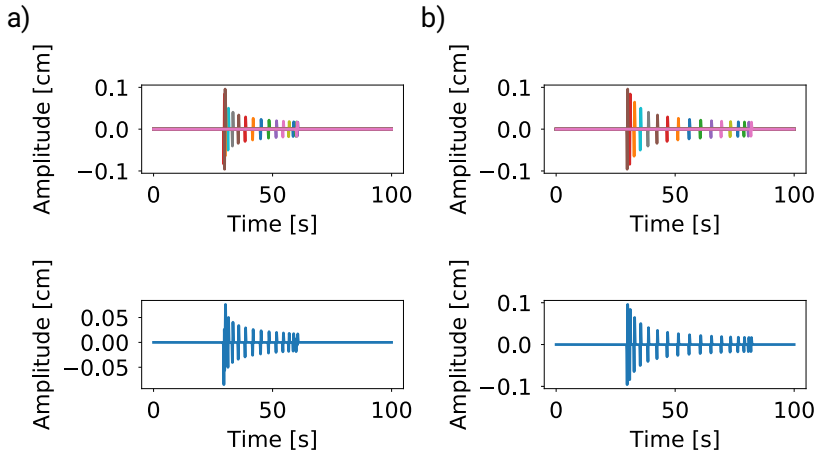

Figure 2.13: (Up) individual point source contributions at the station and (down) the net waveform produced by a ring fault when individual contributions are independent. Moment tensor inversions performed with this data will retrieve the source parameters of each contribution separately. The maximum difference in time arrivals from two point sources is actually longer than the period of the wave, therefore, all contributions are independent. a) Rupture approaching to the station. b) Rupture receding from the station.

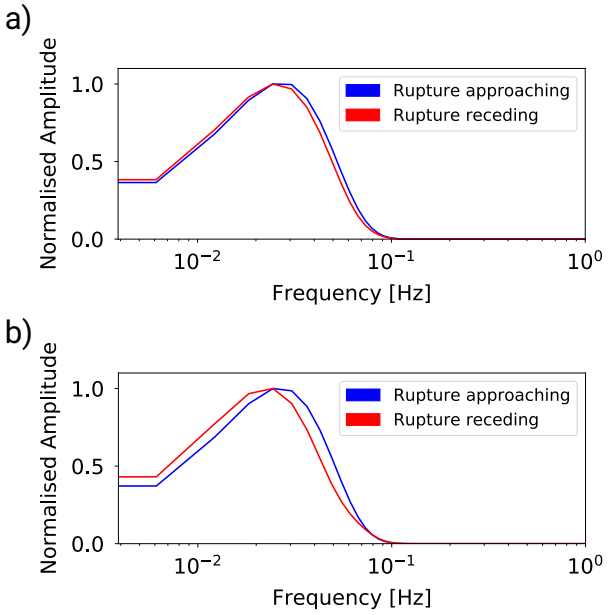

Figure 2.14: Evidence of Doppler effect for a) Planar rupture and b) Half-ring rupture. Note that the effect is stronger for ring-faults.

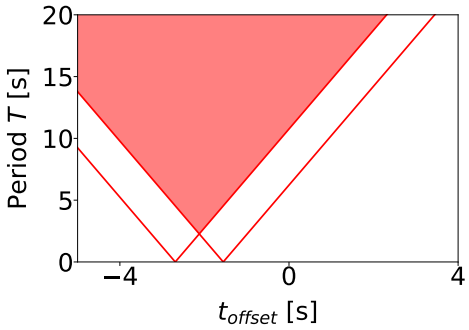

Figure 2.15: The area in red where the period T and the t_{offset} ensure coherence for P and S waves. Negative t_{offset} values indicate rupture approaching to the station.

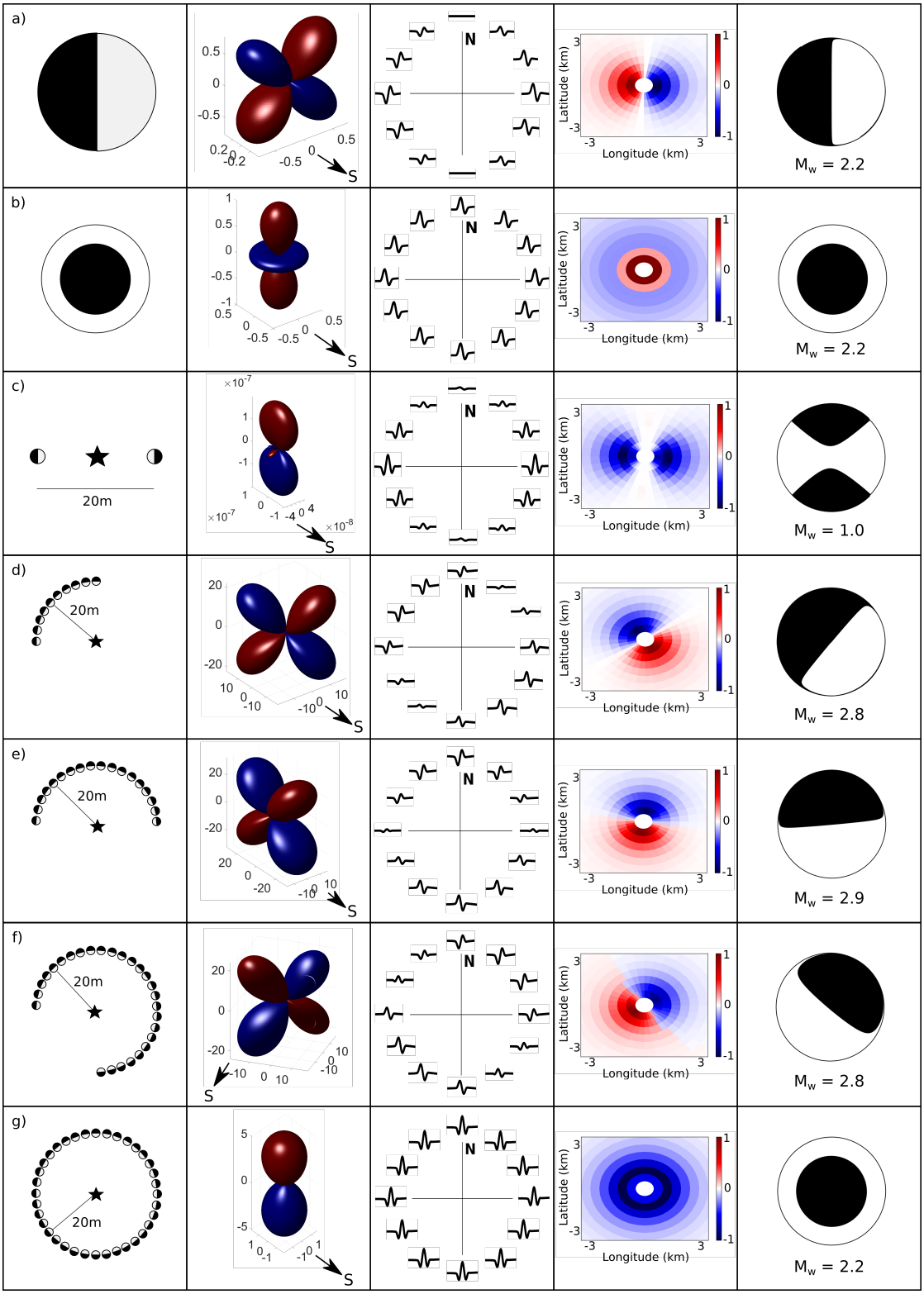
a)
b)
c)
20m
d)
20m
e)
20m
f)
20m
g)
20m
N
S
Latitude (km)
Longitude (km)
M_w = 2.2
M_w = 2.2
M_w = 1.0
M_w = 2.8
M_w = 2.9
M_w = 2.8
M_w = 2.2

Figure 2.16 *(previous page)*: Summary of results obtained for forward and inverse modelling showing in columns: the rupture inspected, radiation pattern calculated, waveforms in all directions, polarisations at surface and moment tensor solution. a) DC point source: waveforms are represented by the derivative of the slip on the fault. The inversion retrieves accurately the MT solution, geometry and magnitude. b) CLVD point source: waveforms are represented by the derivative of the slip on the fault. The inversion retrieves accurately the MT solution, geometry and magnitude. c) Dyke source: waveforms are represented by the second derivative of the slip on the fault. Radiation patterns, which assume simultaneously arriving contributions, are not consistent with polarisations at the surface. The inversion process does not retrieve the correct moment tensor solution and the magnitude is underestimated. d-f) 1/4-, 1/2- and 3/4-ring ruptures show similar results to a DC with different azimuth (Fig. 2.18) The inversion process supports the similarities between these ruptures and DC solutions, however, the magnitudes are underestimated. g) full-ring source: waveforms are represented by the second derivative of the slip on the fault. Radiation patterns, as for the case of the dyke fault, are not consistent with polarisations at the surface. The inversion process does not retrieve the correct moment tensor solution and the magnitude is underestimated. The representation of the MT solution is misleading, as for the dyke rupture, since the correct solution is an implosion and the focal mechanism only shows the deviatoric components.

Radiation patterns (long-wavelength approximation) for dyke and full-ring ruptures are shown in Fig. 2.16c and g, they look similar to a single force acting upwards. For the dyke rupture, lobes are elongated along the dyke's axis with small lobes perpendicular to this axis, which can be observed in very narrow areas. In addition, for the full-ring rupture, lobes are axially symmetric, moreover, we expect positive first arrivals in the vicinity of the epicentre when all contributions arrive at the same time. For partial ring ruptures, we obtain radiation patterns similar to DC ruptures with different orientations, as shown in Fig. 2.16d, e and f. We further discuss them below.

We calculate synthetic seismograms (short-wavelength approximation) for all

rupture types and we select the stations with the largest amplitudes at 1 km epicentral distance. These synthetic amplitudes are computed for ruptures with a different number of point sources. Even without normalising the amplitudes of the overall fault area involved, dyke and full-ring ruptures produce the smallest amplitudes among the complex sources due to the high amount of destructive interference. For partial ring ruptures, we obtain radiation patterns similar to DC ruptures, in addition, the amplitudes do not increase linearly with the fraction of fault area that fails. The highest amplitudes are obtained for half-ring rupture, while amplitudes for 1/4-ring and 3/4-ring ruptures are smaller and similar (Fig. 2.17a). Note, that despite the increasing slip surface from 1/4- to 3/4-ring ruptures, the amplitude remains similar due to a higher proportion of negative interference in the case of the 3/4-ring rupture which affects the overall efficiency of radiated energy from these sources. These amplitude differences are crucial for the calculation of moment magnitude of the events during the inversion process.

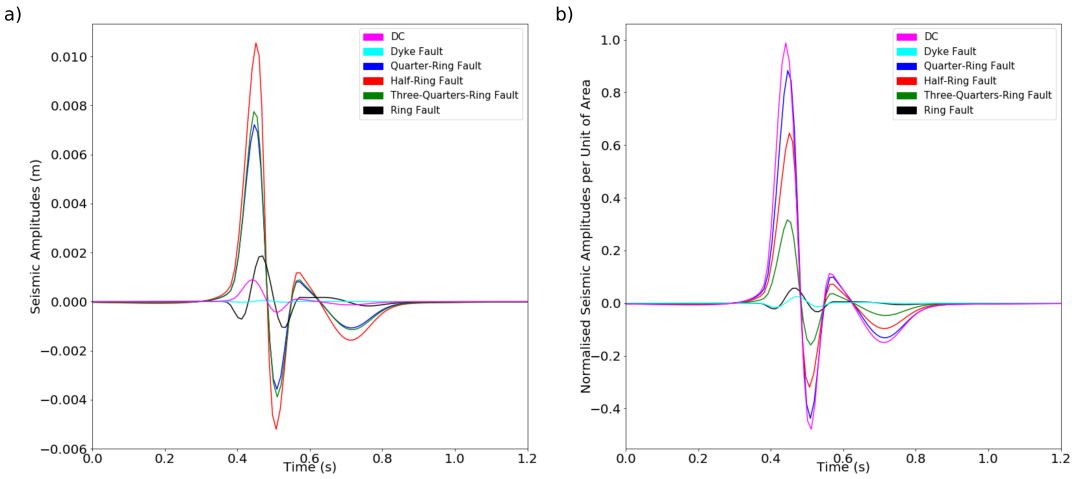

Figure 2.17: a) Raw amplitudes obtained from modelling. b) Normalised amplitudes by area of rupture, it can be understood as the radiation efficiency of each source geometry. This plot compares the radiation produced by all source shapes having the same area of rupture, thus, the differences in maximum amplitudes are only attributable to the shape differences ("efficiency" of each source).

In order to quantify the efficiency of each source type, we compare the amplitudes with the maximum amplitude produced by a single DC with the same surface slip area i.e. we calculate the maximum amplitudes of first onsets at 1 km epicentral distance and normalise them to the area of rupture for each case. Then, we compare the radiation emitted by sources with the same area but different shapes (Fig. 2.17b). The maximum amplitude of the first arrival at 1 km distance produced by a 1/4-ring rupture is reduced to 89% of the amplitude produced by a DC. For 1/2-ring rupture, the reduction reaches 63% and for 3/4-ring rupture, the amplitude is reduced to 30%. The waveforms and polarisations obtained are consistent with far-field DC radiation: the 1/4-ring rupture shows similar radiation to a 45° striking vertical DC, the half-ring rupture similar to a vertical DC with 90° strike and the 3/4-ring rupture with a 135° striking vertical DC, as it is shown in Fig. 2.18.

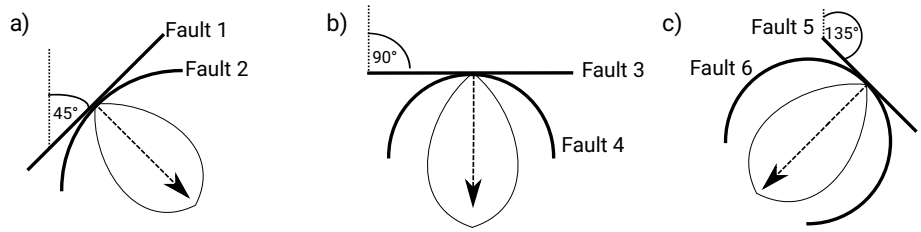

Figure 2.18: Six different faults with their direction of maximum amplitude. This direction is parallel to the symmetry axis of the curved faults and perpendicular to the planar faults. Left: Similarities between 1/4-ring rupture and 45° striking planar fault. Centre: Similarities between 1/2-ring rupture and 90° striking planar fault. Right: Similarities between 3/4-ring rupture and 135° striking planar fault.

The similarity between these partial ring ruptures and their corresponding planar fault is because the point source contribution at the flanks of the rupture is responsible for the negative interference, reducing the resulting amplitude, while the sources at the central zone of the partial ring contribute most of the radiated energy. Hence, the direction of maximum radiation is defined by the normal to the alignment of the sources in the central zone (Fig. 2.18). The general amplitude

behaviour is dependent on the symmetry and dimension of the complex sources and will be further reviewed in the discussion section.

For the dyke and full-ring rupture we obtain a further amplitude reduction to only 0.7% and 2.4%, compared to a same-size DC, respectively (Fig. 2.17b). Results of the modelling are summarised in Fig. 2.16. Note that this behaviour is observed only for strong curvatures, e.g. for a small conduit radius of 20 m or narrow dyke with 10 m opening. In subsection 2.5.3 and Chapter 4 we will investigate the impact of fault curvature, i.e. for different radius.

2.5.2 Waveforms: travel time differences

In this section, we focus on the polarisations and waveforms for each source type, now taking travel time differences between individual sources into account, i.e. using a short wavelength approximation. Synthetics are calculated as described in the previous section using Eq. 2.1 and parameters in Table 2.1. The slip at the fault is modelled by a simulated delta function f,

$$f(t) = \exp\left(-200(t-0.2)^2\right) \tag{2.4}$$

with 5 Hz cut-off frequency, therefore, we expect for each contribution waveforms proportional to the first derivative of the slip at the fault $\dot{f}$ since all the stations are located in the far-field domain.

The synthetic seismograms obtained for partial ring rupture using the software QSEIS show that the waveforms represent the first derivative of the displacement on the fault $\dot{f}$, as expected. Hence, the configuration of sources, in this case, does not affect significantly the waveforms. On the other hand, the synthetic seismograms for dyke and full-ring ruptures are proportional to the second derivative of the slip on the fault $\ddot{f}$, which differs from that expected for a point source (Fig. 2.19). Due to interference of sources of opposite polarisation in close proximity e.g. dyke rupture, the waveforms $u(t)$ show an additional differentiation effect. Hence,

$$u(t) \propto \left[\dot{f}(t) - \dot{f}(t+dt)\right] \quad \propto \quad \ddot{f} \quad \text{, if } dt \to 0 \tag{2.5}$$

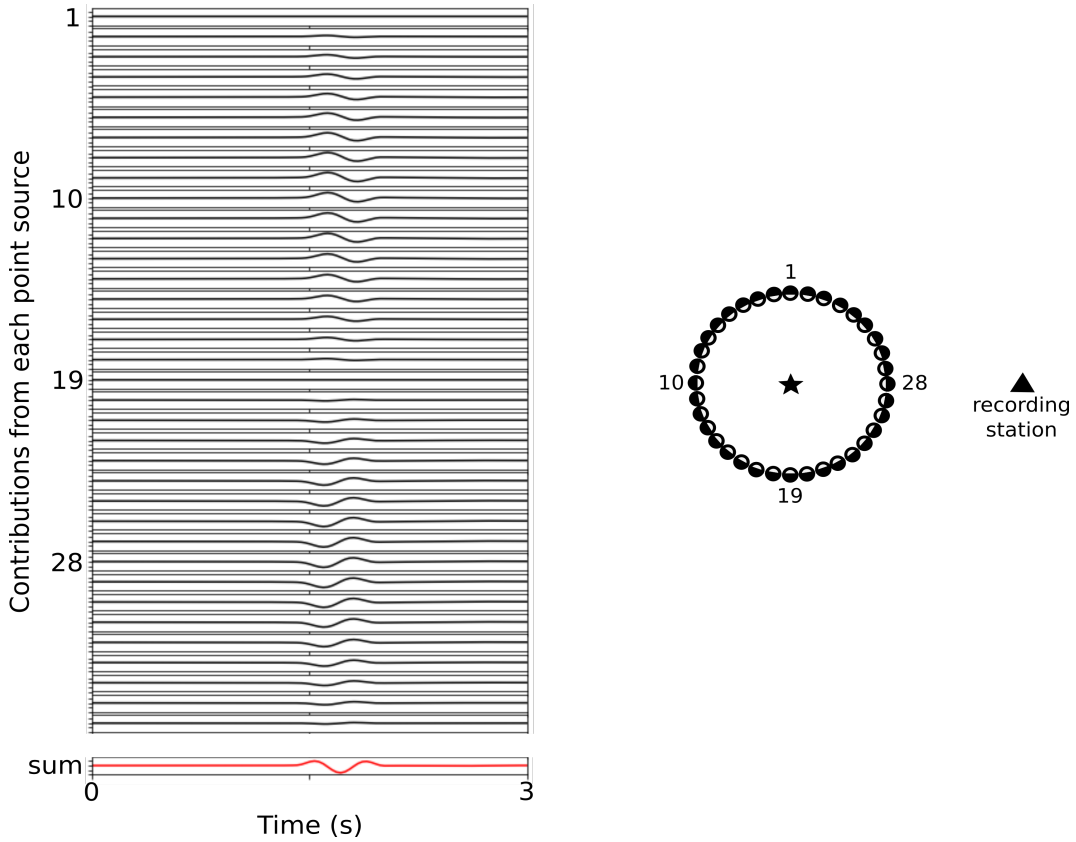

Figure 2.19: Contributions of individual sources representing a full-ring rupture (black) and the resulting waveform (red) at a recording station to the east. Note that single waveforms differ according to the radiation pattern. The resulting waveform (sum) exhibiting an apparent time derivative is due to slight differences in travel time between contributing sources. The sketch on the right is not to scale.

where dt corresponds to the travel time difference between the two sources on opposite sides of the dyke rupture or full-ring rupture. Hence, for small dt the superposition of these two sources introduces an apparent time derivative. The special case of the waveform produced by a 3/4-ring rupture where two opposed quarter ruptures produce this double differentiated signal, i.e. NW and SE quarters. However, their amplitude is much smaller than the produced by the remaining quarter (NE) which dominates the signal with a waveform proportional to $\dot{f}$, emulating

the case of a 1/4-ring rupture with 135° azimuth (Fig. 2.18).

Although the magmatic process to produce these synthetic seismograms is related to an overpressure in the plumbing system which drives magma ascent, the polarisations for the dyke and the full-ring ruptures show negative first onsets. Note that for a single source this negative polarisation would be linked to an implosion or a closing crack, i.e. a geological structure collapsing due to lack of pressure.

2.5.3 Effect of the curvature on the seismic radiation

So far we have investigated the effect of different angular ruptures on the net radiation, using a fixed 20 m radius using recording stations outside the ring. In this section, we locate the recording station in an axis perpendicular to the curved source at its middle point (Fig. 2.6a) in order to evaluate the relationship between amplitude and the radius of curvature.

We calculate the radiation of a 1/4-ring rupture with different curvatures arriving at the station fixed at 6 km away from the rupture's centre point (Fig. 2.6a). Using the radius of curvature r and the distance from the station to fault d, we can generalise the results and identify three cases depending on the value of the ratio r/d: for $r/d < 1$ the station is located outside the ring structure, for $r/d > 1$ is located within the structure, while for $r/d = 1$ is located in the centre of the ring. We show in Fig. 2.6b that the amplitudes for stations outside the ring structure reach values that we can consider normal for far-field radiation. For larger ring faults, hence $r/d \to 1$, the amplitude of radiation decays about 5 times the maximum amplitude due to the combination of geometrical effects and wavelength interference. An important focusing effect is observed when the station is placed in the centre of the ring fault $r/d = 1$, where it reaches the maximum value, which is not predicted by the geometrical spreading. This is the only point where travel time differences are zero, i.e. all the contributions arrive at the same time and interfere constructively. Amplitudes decrease again when the station is placed even closer to the fault $r/d > 1$, increasing destructive interference. This shows that the amplitudes behave differently when stations are located inside and outside

the ring fault, increasing the variability of possible moment tensor solutions and magnitudes. We will further investigate this inference in Chapter 4.

All these ruptures produce signals that might have been observed in nature and they could have an interpretation in terms of the classic view of moment tensor inversion. Some of these interpretations were made considering first arrivals instead of the full waveform, and therefore they may be an oversimplification for magma ascent processes. For the moment tensor inversion carried out here, we show that the classic approach will provide a solution based on a single point source, fitting the "best" moment tensor solution in the established scheme, however, it does not point to the actual physical process. We will prove in the next section that this method systematically underestimates the magnitude and misinterprets the slip on the fault.

2.6 Inverse modelling

The synthetic seismograms for each source are a superposition of individual point source contributions. The wave interference between different point sources distort the net radiation at different levels, e.g. dyke and full-ring ruptures introduce an additional time derivative in the waveforms and the amplitudes change drastically. On the other hand, partial ring ruptures maintain the waveforms expected for a single source, while amplitudes and location of nodal planes change significantly. Therefore, wave interference introduces apparent changes in source parameters and magnitude calculations, which need to be quantified and corrected. We perform moment tensor inversions in order to obtain source parameters for each source assuming a point source. The KIWI software (Cesca et al., 2010) provides moment tensor components in a specific frequency band and considering the full waveforms based on the Levenberg-Marquardt method (Moré, 1978). It computes the fraction of this solution which represents ISO, DC and CLVD components. Thus, we treat these spatially extended sources as a simple point source, although it does not consider the physics involved and the real geometry.

To perform the moment tensor inversion we use a subset of 36 "recording stations" that are deployed in 3 concentric rings at 1 km, 2 km and 3 km distance and an ideal azimuthal coverage every 30°. It is important to note that each

point source used in the forward modelling are vertical DCs with $M_W = 2.2$ or $M_0 = 2.5 \times 10^{12}$ Nm. For comparison with the ruptures studied, Fig. 2.16a and b show radiation patterns, polarisations at the surface, waveforms and focal mechanisms for a single DC rupture and CLVD, respectively. These sources for comparison are $M_W = 2.2$ events with a seismic moment of $M_0 = 2.5 \times 10^{12}$ Nm.

Fig. 2.16c shows main features of radiation for the dyke rupture, radiation pattern, polarisations at surface and waveforms. Synthetic seismograms show negative first onsets in the stations to the east and west from the epicentre, in addition to amplitudes tending to zero to the north and south, no positive first onsets are obtained. The MT solution shows an 87% isotropic component, 10% DC and 3% CLVD, the magnitude calculated is $M_W = 1$. This MT result returns a closing/imploding crack, which can explain the polarisations at the surface but fail to retrieve the correct shear dynamics at the dyke source replacing it by volumetric forces in the E-W direction.

For partial ring rupture cases (Fig. 2.16d, e and f) we observe similarities with DC radiation. Accordingly, the MT solutions are dominated by vertical DC components ($> 90\%$). We obtain different fault azimuths for different ruptures modelled, which are consistent with polarisations observed, e.g. 45° for 1/4-ring rupture, 90° for 1/2-ring rupture and 135° for 3/4-ring rupture. However, the maximum amplitudes are different in each case, e.g. the magnitude for the case of 1/2-ring rupture shows an apparent Moment Magnitude of 2.9. Moreover, despite the differences in areas of rupture, the cases of 1/4-ring rupture and 3/4-ring rupture show the same magnitude of $M_W = 2.8$.

Fig. 2.16g shows the axially symmetric results of the full-ring rupture. Only negative first onsets are observed, despite the radiation pattern showing a positive lobe just above the hypocentre. The focal mechanism shown points to a vertical CLVD point source, however, this is fundamentally different as far as polarisations are concerned. The CLVD solution assigns positive first arrivals to the stations at 1 km distance which actually shows negative onsets. Thus, this solution minimises the misfit during the inversion process, but it does not represent the physics of the

source process at all. In addition, the MT solution is,

$$\begin{pmatrix} -1.543778 & -0.002433 & -0.003922 \\ -0.002433 & -1.546797 & -0.002606 \\ -0.003922 & -0.002606 & -1.032088 \end{pmatrix} \times 1.8 \cdot 10^{12} \text{ Nm} \tag{2.6}$$

indicating 80% isotropic component and 20% CLVD. In this case, the graphic representation of the result is misleading since it looks like a vertical CLVD (deviatoric), however, the diagonal components are all negative representing an imploding volume.

Moreover, the inversion procedure integrates the waveforms observed in the far-field to obtain the correct source slip at the fault. For cases of partial rupture, this point source approach returns the correct slip on the fault. However, for the cases of dyke rupture and full-ring rupture, the moment tensor inversion returns the derivative of the actual source slip at the fault. Hence a double integration would be necessary to retrieve the correct source time history.

2.7 Discussion: implications for volcano seismology

This theoretical and numerical approach attempts to provide the fundamental features of the radiation patterns, i.e. waveforms, polarisations and amplitudes for non-planar faults and compare them with point sources. Furthermore, from synthetic seismograms, we obtain moment tensor solutions assuming a point source rupture.

2.7.1 Classic view fails

The study of these scenarios demonstrates that the added complexity of volcanic seismic sources leaves a much wider space for interpretation of the actual source process. This has important consequences if classic moment tensor inversion techniques, based on the point source assumption, are used to estimate magma ascent rates from earthquake swarms. This is an open question and one of the aims of Chapter 3, which can be adapted by volcano observatories around the world if it

is calibrated appropriately with as low as one seismic station (assuming a full-ring rupture). The slip at the fault and the seismic moment within a magma conduit is thought to be linked with magma ascent. Due to interference, a complex rupture of any shape will always produce seismic amplitudes that are smaller than any planar slip surface of equivalent size and slip. In addition, the actual values for amplitudes depend on the trade-off between wavelength and curvature of the structure. If a spatially extended source is assumed as a point source, the discrepancies in P-wave amplitudes will lead to an underestimation of the rate at which magma rises in the volcanic conduit. For example, the moment tensor inversion of the full-ring rupture case can result in an underestimation of the seismic moment M_0 by a factor of ~ 42. This correction comes from the reduction to 2.4% in the seismic radiation, i.e. a reduction of 42 times the radiation of the same size double couple. The underestimation of M_0 leads to an underestimation of slip on the fault and a consequent underestimation of magma flow rate in depth which may have severe implications for eruption forecast. Hence, we are assuming less magma moving upwards in the system.

If the nature of the source (planar or ring rupture) and its seismic moment M_0 are known, magma ascent rates can be inferred from measured seismic amplitudes. We propose that the ascent of magma is proportional to the seismic slip at complex sources if the conditions of magma and overall strain are constant (overpressure). However, this proportion needs to be constantly monitored in order to identify temporal variations in this proportion due to changes in magma properties or overpressure of the system. By advancing towards inversion techniques that allow for spatially extended source mechanisms, the amount of slip occurring in the conduit can be calibrated. These inversion techniques need to be able to analyse the full waveform obtained, not only the first arrivals in order to address the differences in waveforms we obtained for the cases of dyke and full-ring ruptures. For these cases we obtain a waveform which appears to be the second derivative of the slip function on the fault, introducing a critical problem when using classic moment tensor inversions since these methods integrate waveforms only once to retrieve the slip function. This leads to a misinterpretation of the slip history at the fault, which can have huge implications for volcano monitoring. If we observe $\ddot{f}$ at the stations, a point source inversion scheme will interpret the slip on the

fault as $\dot{f}$ which means an oscillating magma column while the model was based on a simple upward motion followed by relaxation (Fig. 2.20).

The calibration of individual volcanic systems by comparison of observed seismic amplitudes and magma extrusion rates is therefore crucial to obtain accurate magma flow rates along extended fault planes, and once successfully calibrated this will contribute towards identifying a critical value of magma flow rate that may lead to dome collapse (Thomas and Neuberg, 2012). Moreover, unless a volcanic edifice is covered by a very dense seismic network providing sufficient input for the inversion of a higher-order moment tensor, with a suitable network geometry (Lanza and Waite, 2018a), it is very unlikely that the true mechanism of a complex volcanic seismic source can be determined in a unique way. In addition, caution should be applied if classic moment tensor inversions return CLVD, DC or single force component mechanisms with large uncertainties, the magma ascent rates determined in such way should be considered lower bounds only. This will be further discussed in Chapter 3.

2.7.2 Are the signals observed generated by complex sources?

In contrast to automatically assuming point sources and planar faults, we suggest considering other rupture shapes to explain the seismic observations, which show high levels of uncertainty and might be generated within a volcanic environment. However, how can we gather enough evidence to select complex ruptures approach and discard planar fault rupture?

For the case of dyke and full-ring ruptures we expect negative polarisations at all stations, however, they have different properties than an isotropic implosion or an imploding crack. For example, the dyke rupture shows a nodal plane along with its projection at the surface, thus, the amplitude pattern is unique for these ruptures. For the full-ring rupture, waveforms show radial symmetry with amplitudes that increase in the first kilometre, for a 1 km depth source. A first onset polarisation study can give important information to decide which approach we should follow.

Moreover, the waveforms modelled can be more easily explained with complex ruptures. A scheme of the different situations assuming different slip on the fault

is shown in Fig. 2.20, explaining the integration process needed to retrieve the correct slip history at the fault. Note that the function f was selected for this study since the modelled displacement (Fig. 2.20a - 3rd waveform) has similarities with velocity seismograms in nature when the slip on the ring fault is modelled as a step function (Fig. 2.20b - 5th waveform). On the other hand, the same waveforms can be explained as far-field velocity records produced by a planar fault if we assume a displacement on the fault given by a simulated delta function (Fig. 2.20c - 4th waveform), i.e. upward and downward magma movement. However, tectonic or magmatic tractions cannot change direction so fast and easily, and a net displacement on the fault is needed when magma is moving upwards and eventually being extruded. Thus, the most suitable function to describe slip on the fault is still the step function. Some studies have considered source time functions described by a simulated delta function to explain the data, which can be a possible mechanism for very long period pressurisation and depressurisation of the system (Chouet and Matoza, 2013; Lyons and Waite, 2011) but not for LP trigger signals.

Additionally, due to the radial symmetry, polarisations obtained for full-ring rupture are similar to the ones produced by a single vertical force which are often used in moment tensor inversions in volcanic environments. We perform moment tensor inversions for the full-ring rupture, obtaining simultaneous solutions for moment tensor and single force components. This returns the superposition of a downward single force and a vertical CLVD (Fig. 2.21). Hence, the isotropic components obtained previously are now replaced by a vertical single force. A significant contribution attributed to a single force (plus CLVD) could give an indication that a complex source such as a ring fault should be considered, particularly if the inferred displacement at the source indicates an additional derivative of an expected upwards motion by magma ascent. In this light, single force inversions would decrease the misfits, however, without explaining the physics of the source adequately and still the displacement at the fault would be misinterpreted.

2.7.3 Full-ring rupture as CLVD?

By numerical integration along the conduit walls, we obtain the radiation patterns depicted in Fig. 2.16. For comparison, they are shown together with the classic

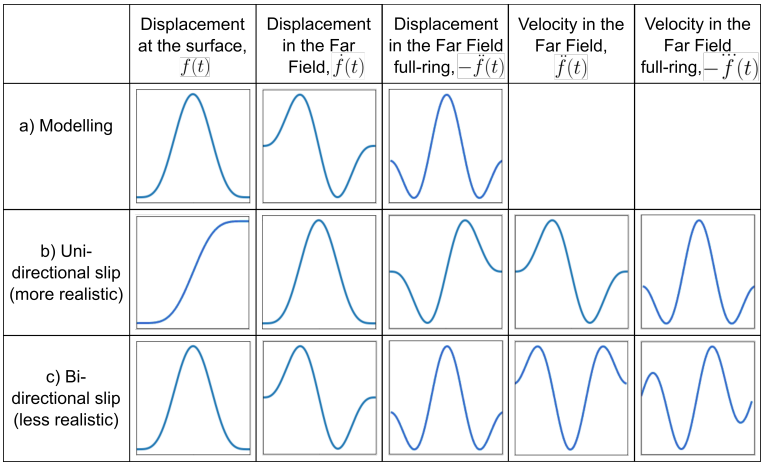

Figure 2.20: Waveforms expected for the forward modelling, using a source described through a Moment Tensor for: a) Case modelled. b) Uni-directional slip, note that the velocity record in the far-field for the full-ring rupture is similar to the displacement produced by a full-ring fault in our modelling. During volcanic unrest, the magma follows an upward movement, so this is a more realistic case for LP trigger rupture. c) Bi-directional slip. This would represent magma moving upwards and downwards as part of the same rupture process, which during unrest is unlikely.

vertical double couple solution and the pattern for a compensated linear vector dipole (CLVD). The radiation pattern for the full-ring rupture shows axial symmetry about the vertical axis and consists of a large compressional lobe directly above the source and an inversely polarised, tensional lobe with the same amplitude below it. The observed radiation patterns of ring fault and CLVD source are remarkably similar in the upper hemisphere (in the vicinity of the epicentre), but they are fundamentally different as a whole. Their distinction in volcanic settings, however, is likely to be very difficult. For both, CLVD and full-ring rupture, the nodal surfaces lie off the fault axes, and the transition from compressional to tensional first motion is, therefore, dependent on the source depth of the event. Due to the shallow source depths of most volcano seismic events, the generally narrow aperture of seismic networks on volcanoes, and small magnitudes ($M_{\mathrm{W}} < 3$), the only seismicity radiated at limited take-off angles above the source will likely be

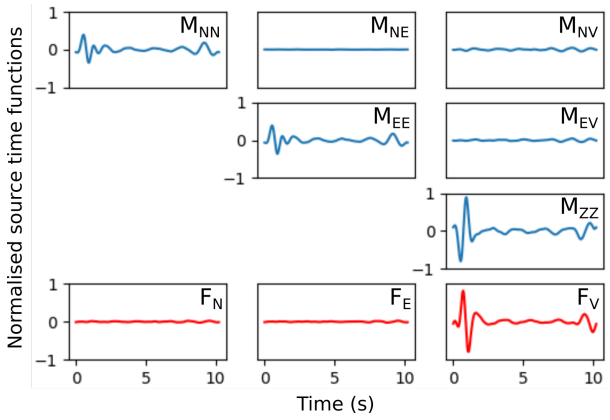

Figure 2.21: Source time functions for moment tensor components and single forces. The results show a vertical CLVD and a single force pointing downwards (note that the F_{V} component is positive downwards).

detected. This means that the radiation of the trigger should not be observed at distant stations e.g. in our modelling of the full-ring rupture, the amplitudes observed at the closest stations 500 m decay by a factor of 12 compared to the stations at 5 km. Generally, given a specific topography and station distribution the two fundamentally different physical processes for the trigger, ascending magma in the conduit represented by the full-ring fault model on the one hand, and a CLVD model, on the other hand, may result in the same observed P-wave polarities with almost indistinguishable radiation patterns.

Seismic signatures observed at Nyiragongo volcano, D. R. Congo, between 2002 and 2005 exhibited a radiation pattern showing downward motion in the centre and upwards motion around it (Shuler and Ekström, 2009). These events were interpreted as caused by slow slip on an outward dipping ring fault (Ekström, 1994) and labelled as CLVD. Similarly, in 2014, seismic events were detected on Bárðarbunga volcanic complex, Iceland, comparable to some events observed in 1995, which had been associated with slip on at least a part of a ring fault and described as having a CLVD component (Nettles and Ekström, 1998). In these cases, a CLVD component was generated by inverse ruptures at a conical fault surface and their seismic signature was observed in the far-field as teleseismic events. By inverting long-period seismic data, the epicentre would be determined

in the centre of the ring fault, but not along the fault. CLVD and ring ruptures are fundamentally different source mechanisms which require different interpretations. A CLVD is caused by redistribution of volume, e.g. the drainage of magma from a chamber into a sill. In contrast, the motion of a ring fault could be interpreted as ascending or descending magma without conserving the overall volume, even though the ruptures comprise only shear rupture. These caldera-size cases will be further discussed in Chapter 4, since extra considerations need to be taken into account.

2.8 Conclusions

Geological observations of different fault shapes have been reported in volcanic environments, which deviate from planar faults. We demonstrate that MT inversions for these ruptures systematically underestimate the magnitude of the event and misinterpret the slip on the fault when we adopt the classic view of point sources. MT inversion software packages will calculate the best fitting solution between DC, CLVD and isotropic components or combinations of them, even if the geometry of the fault and the physics of rupture are not well represented.

Some important considerations need to be taken into account to create synthetic seismograms. Condition 1.12 or equivalently the condition 2.6

The misinterpretation of the slip on the fault can introduce ambiguity in the estimations of magma ascent, which we will study in the following chapter. Since the fractures occur in the magma body, the seismic slip represents the time history of magma ascent. If we record a full-ring rupture with broadband seismometers in the surroundings of the event, and we treat it as a point source, we obtain as the slip on the fault a simulated delta function, hence, an upward and downward motion. This means that the magma seems to ascend in the first part, and then falls back to its original position, therefore, no net ascent is taking place. This is in contrast to the step-wise magma ascent actually taking place which leads to a fundamentally different source process.

The impact of underestimating the magnitude is critical for magma ascent estimation since a smaller magnitude implies smaller slip, hence a smaller ascent rate.

The polarisation of first onsets cannot be represented by the summation of radiation patterns, the restriction of simultaneously arriving waves is not feasible due to travel time differences. For full-ring ruptures, the radiation is axially symmetric, similar to a negative CLVD or downward single force but not exactly the same. It is very difficult in real observations to differentiate between those interpretations due to the limited number of instruments in seismic networks. The dyke ruptures can be spanned as closing cracks using the point source approximation, which is a completely different physical mechanism. Moreover, we expect DC solutions for a partial-ring rupture with vertical faults, so far there is no seismological methodology capable of differentiating between a planar fault and a vertical partial-ring rupture. It is important to note that for conical ring faults (non-vertical walls) the deviatoric solution retrieved a dominant CLVD component (Ekström, 1994), we will come back to this case in Chapter 4.

A theory is needed, which can address differences between spatially extended sources with different fault geometries and predict radiation features analytically, e.g. higher-order moment tensor (Dahm and Krüger, 1999) or multiple MT inversions (Tsai et al., 2005). Ambiguous results during inversion methods should be interpreted as an indication that complex sources might be at work. Data have to be compared with synthetics in order to inspect different ruptures. Finally, it is of major importance that the MT solutions and focal mechanisms include the study of full waveforms, instead of considering only first arrival polarisations, since the waveforms can be seriously deformed by interference patterns due to a complex source geometry.

Chapter 3

Magma Ascent Estimations: Case Soufrière Hills

In the previous section, we studied the properties of radiation produced by complex sources and how the MT inversion software interprets this radiation pattern in order to provide source parameters. One of the main results found is that the radiation does not follow the same linear relationship between seismic moment and amplitudes. In this section, we will study these differences in a real case scenario and apply corrections to the results provided by moment tensor (MT) estimations from the previous chapter regarding seismic moment and amplitudes observed. By linking the slip at the rupture area within the conduit with the magma extrusion observed at Soufrière Hills in Montserrat island, West Indies, we attempt to estimate magma extrusion and ascent rate directly from the seismogram. This chapter is based on an article in preparation with Jurgen Neuberg and Luke Marsden.

3.1 Soufrière Hills eruption

Soufrière Hills is a silicic volcano in Montserrat island, West Indies, which has been erupting for more than 25 years. It has shown periods of explosive behaviour, dome collapse events and pyroclastic flows, among other hazards, endangering the whole population and infrastructure of the island (Wadge et al., 2014). The eruption has been very well monitored and studied extensively, considering its evolution

divided in five phases with different eruptive styles (Cole et al., 2014a,b; Kokelaar, 2002; Melnik and Sparks, 2002; Sparks and Young, 2002; Stinton et al., 2014a,b; Wadge et al., 2010, 2014; Young et al., 1998), measurements of the dense rock equivalent (DRE) erupted volume at surface (Stinton et al., 2014a; Wadge et al., 2010, 2014), dome growth and collapse dynamics (Melnik and Sparks, 2002; Sparks et al., 1998), magma mixing and the silicic composition of the melt (Murphy et al., 1998), alongside near and far field deformation which correlates with intense and varied seismic activity (Wadge et al., 2014). All these contributions have helped to make this event one of the best described volcanic eruptions ever analysed.

Seismic activity has been present throughout the eruption with a wide variety of seismic signals with different source interpretations (Aspinall et al., 1998; Green and Neuberg, 2006; Luckett et al., 2008; Miller et al., 1998; Neuberg et al., 1998, 2000; White et al., 1998), e.g. volcano-tectonic events (VTs) which are interpreted as brittle failure of rock (Ágústsdóttir et al., 2016), rockfalls interpreted as dome collapse or pyroclastic flows (Hale et al., 2009; Loughlin et al., 2010) and low-frequency events, which can be divided into hybrids, with a high-frequency onset, and long-period events (LPs), the latter can be interpreted as the result of brittle failure, fluid resonance and travel path effects (Bean et al., 2014; Chouet, 1988, 1996; Ferrazzini and Aki, 1987; Neuberg et al., 2006). In addition, low-frequency events can merge into tremor in epochs of intense activity (Neuberg et al., 2000). Prior to dome collapse events, an increase in the occurrence of low-frequency events has been observed (Neuberg et al., 2006; White et al., 1998) which are very well correlated to cyclic tilt changes (Green and Neuberg, 2006; Hautmann et al., 2009). In this study, we focus on the trigger of low-frequency events, which is non-destructive, repetitive and shows constant locations (Jolly et al., 2012; Neuberg et al., 2006; Richardson and Waite, 2013; Varley et al., 2010).

3.2 Low-frequency events

A robust and widely accepted physical model has been developed to explain the rupture process for these events which explain the main characteristics of the high-frequency trigger and the low-frequency coda. A combination of viscous magma and high strain rates produce shear stresses that can overcome the strength of

magma and produce brittle failure at the conduit's wall (Denlinger and Hoblitt, 1999; Neuberg et al., 2006; Thomas and Neuberg, 2012). Theoretical studies (Denlinger and Hoblitt, 1999) and data analysis (Green and Neuberg, 2006; Neuberg et al., 2006; Voight et al., 1999) have shown that this behaviour is cyclic with periods of around 10 hours. De Angelis and Henton (2011) have also studied seismicity occurrence between June 22nd and 25th, 1997, and estimated the dynamic values for magma ascent to analyse the feasibility of magma rupture for different viscosity values. Moreover, models of rock failure (Hammer and Neuberg, 2009; Salvage and Neuberg, 2016) have been developed to estimate the time of occurrence of dome collapse events, which are the ultimate process when the rate of seismicity reaches a certain critical value. Furthermore, Green and Neuberg (2006) thoroughly studied the cyclic seismicity and tilt data from June 23rd to June 28th, 1997, which include a dome collapse event on June 25th at 16:45 UTC. They grouped the seismicity into families which mainly differ on their focal depth, for example we show the locations of low-frequency events of a single family reported by Neuberg et al. (2006) in Fig. 3.1. Moreover, we show in Fig. 3.2 the locations of around 250 events, which follow an oblique direction from 300 m − 100 m with no reported clear temporal variation. Those families are active at different stages of the 10 hours cycles, e.g. group A earthquakes (Fig. 3.3) occur when the tilt is maximum until the dome collapse occurs (Green and Neuberg, 2006), similar to the model proposed by Denlinger and Hoblitt (1999). After the collapse, no events were recorded for more than 24 hours; when the dome is rebuilt family A restarts its occurrence. The conceptual models described explain adequately the trigger source, dome collapse and the cycles of seismicity and tilt, however, no studies have focused on the relationship between amplitudes, seismic moment and magma ascent rates.

We analyse data from a single family of low-frequency events occurred between June 22nd and 25th, 1997, the activity culminates in a dome collapse at 16:45 UTC. The intense cyclic occurrence is closely related to the magma extrusion observed during those days. We assume that the rupture occurs at the conduit wall following a ring-shape since the conduit radius R is small ($R \sim 15$ m) and the models of magma ascent point to a radial symmetry of the velocity profile, we expect that the rupture also shows this radial symmetry. This is a strong

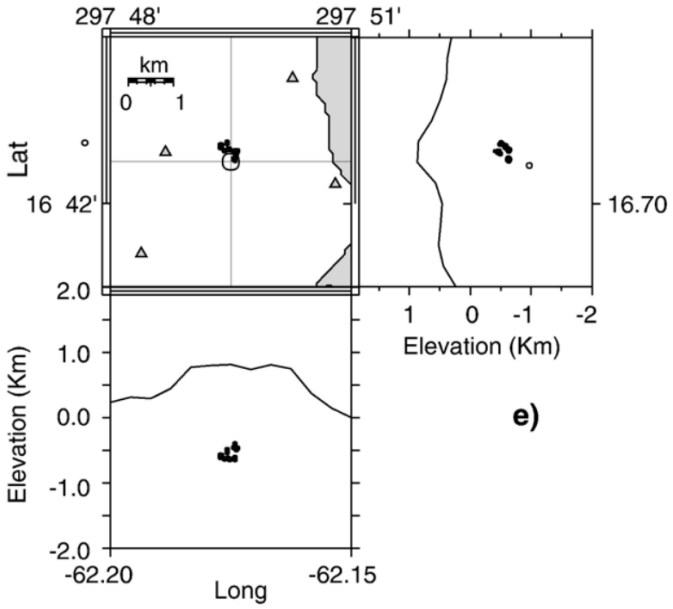

Figure 3.1: Figure adapted from Neuberg et al. (2006). Seismic location of low-frequency events during June 1997, locations are fixed around 500 m depth within an acceptable range of uncertainties. They do not migrate with time.

assumption that can include large misfits to our results, we discuss these misfits in Chapter 5. Therefore, seismic sources from different parts of the ring fault interfere with each other and net radiation could be interpreted as a point source instead of a curved real fault surface with a smaller seismic moment (Contreras-Arratia and Neuberg, 2019). We use the correction factors obtained in Chapter 2 in order to estimate real slip vectors at a ring fault. The radiation of the full-ring rupture, represents 2.4% of the radiation produced by a planar fault, thus, the correction factor is $\sim$ 42. Subsequently we quantify for the first time magma ascent and extrusion by using low-frequency seismicity.

3.3 Seismic data

We inspect seismic data provided by the Montserrat Volcano Observatory (MVO), who run a seismic network shown in Fig. 3.4, which consists of a mixture of broadband, short period and vertical sensors with intermittent periods of good

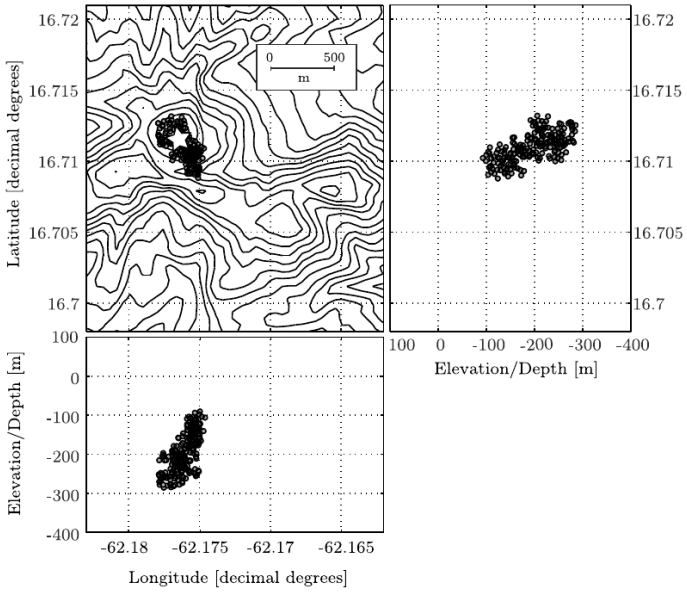

Figure 3.2: Figure adapted from De Angelis and Henton (2011). Seismic location of low-frequency events during June 1997, locations follow an oblique linear structure from 300 m − 100 m depth.

performance. Other organisations such as BGS (United Kingdom), USGS (USA) and SRU (currently SRC, Trinidad and Tobago) have helped in the acquisition of the data. The catalogue contains more than 1400 trigger-recorded seismic events that occurred between June 22nd and 25th, 1997, however, Green and Neuberg (2006) have reported more than 2000 events at the same period of time from continuous data. The station MBLG recorded the highest number of events (Fig. 3.5a), is located 2 km to the north-east of the volcanic centre and is equipped with a Guralp CMG-40T sensor.

In Fig. 3.5b we observe a histogram of occurrence of the low-frequency seismicity belonging to a single family (262 events), in which we can observe the cyclic behaviour and its correlation with the extrusion rate (daily data). Its peak is achieved just before the extrusion on July 24th. The same behaviour can be seen in Fig. 3.5c, where we compare the cumulative seismic moment per cycle with the daily extrusion. We postulate that magma ascent is correlated with the cumulative seismic moment (Fig. 3.5c) rather than the counts of low-frequency events (Fig.

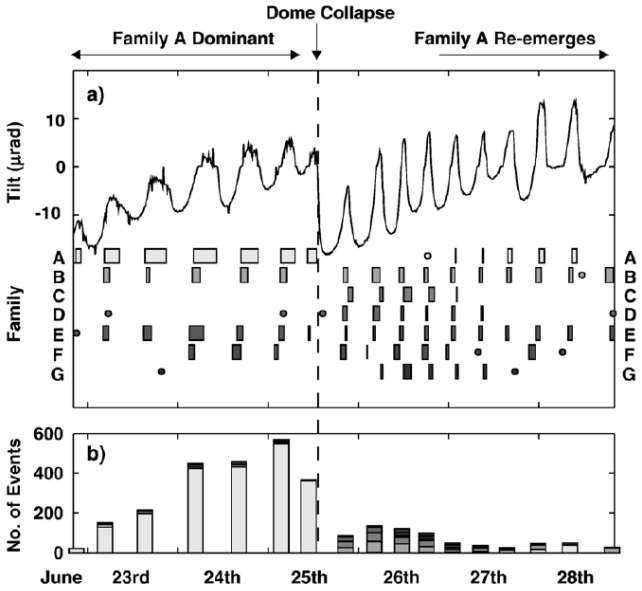

Figure 3.3: Figure adapted from Green and Neuberg (2006). Time series for a) Tilt and family occurrence and b) for histograms of temporal occurrence for each family. We are interested in Family A in the present study.

3.5b). Moreover, the seismic moment for each event needs to be corrected for a full-ring rupture geometry, as discussed in Chapter 2, by multiplying by a factor of 42 to obtain the ring-geometry seismic moment. Thus, we obtain a larger seismic moment and slip for a curved surface earthquake than the values we calculate by assuming a point source.

To analyse the seismic data we remove the instrument response, we integrate to obtain displacement records and filter them with a bandpass filter between 0.5 and 5 Hz (Green and Neuberg, 2006). Later, we cross-correlate all the events recorded during these 4 days, where high correlation coefficients indicate that events belong to the same family i.e. same source mechanism and location (Fig. 3.6, for all the seismicity and the most recurrent family). The family of low-frequency events which shows cyclic behaviour can be grouped in intermittent time windows of 30 hours in total (1 hour = 1 bar in Fig. 3.5b). Examples of the same family events are shown in Fig. 3.7, including their spectra.

We estimate the seismic moment for each event on a planar fault by comparing

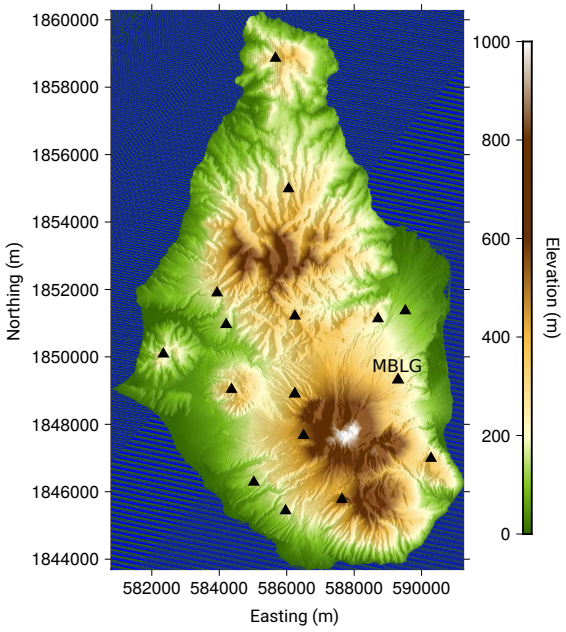

Figure 3.4: Seismic network Montserrat, West Indies. The station MBLG is used for our analysis. The colour shows elevation, coordinates are UTM.

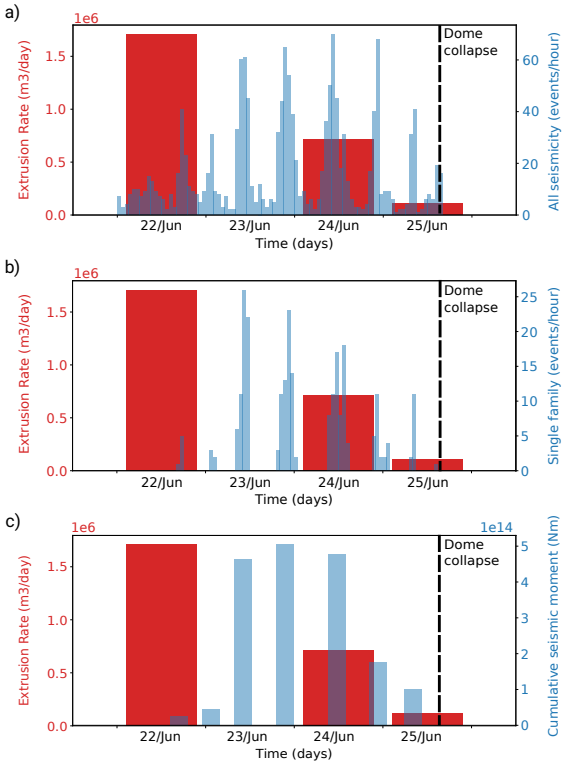

Figure 3.5: In red: Magma extrusion per day during the period of study, one datum per day. In blue: a) Hourly histogram of seismic occurrence, all events. b) Hourly histogram of low-frequency event occurrence, a single family (A in Green and Neuberg (2006)). c) Cumulative seismic moment of low-frequency events per cycle.

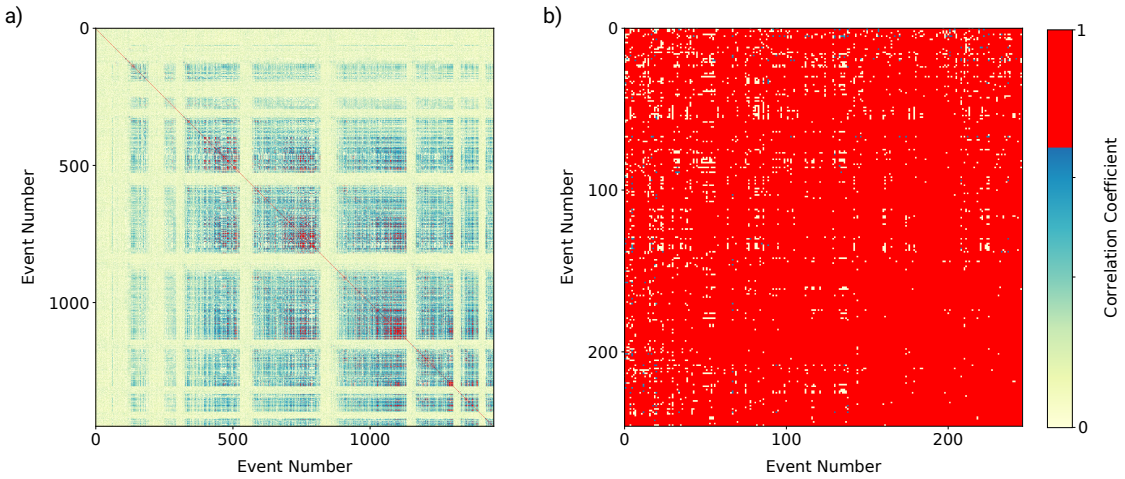

Figure 3.6: Cross correlation matrix between events in our catalogue. a) All events. b) Single family, low-frequency events.

maximum amplitudes obtained with synthetic seismograms using a full-ring source. The events on the catalogue are located below the crater at a focal depth of 500 m below sea level (Neuberg et al., 2006). We also estimate the magnitude of events by using 200 m depth to account for uncertainties (De Angelis and Henton, 2011). Later, we consider an the following empirical relationship between average slip d and seismic moment (Murotani et al., 2013) which helps us to constrain the total vertical movement of the magma pulse during the 30 hours of seismicity,

$$d = 1.66 \times 10^{-7} M_0^{1/3}. \tag{3.1}$$

This empirical relationship was developed for earthquakes with magnitudes larger than 6.7 but the slip values we found are consistent with geological observations of healed fractures in exhumed dykes at Torfajökull volcano, Iceland (Tuffen et al., 2003). This will provide the ratio between the total earthquake slip and the total extrusion rate observed over the 30 hours. This calculation is the first attempt to quantify the direct effect of magma ascent on seismicity.

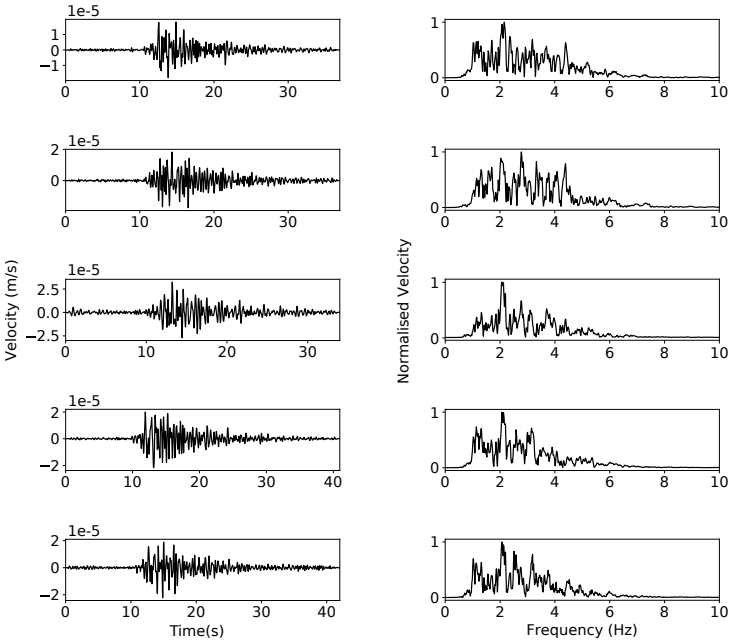

Figure 3.7: Five examples of seismograms recorded at station MBLG and their spectra, one event for each cycle. They all belong to the same family. The events are recorded on: June 23rd, 08:45:13; June 23rd, 20:43:48; June 24th, 10:58:48; June 24th, 21:56:02; June 25th, 08:21:35 (GMT time).

3.4 Seismic moment estimations

The magnitude estimation of low-frequency events (LP and hybrid events) encounters several complexities, which can lead to a wrong estimation of the real energy release during rupture. The local magnitude scale is not appropriate for these events because it is conceived for brittle failure only. It follows an empirical relationship for small to moderate magnitudes ($< M_{\mathrm{L}} = 7$), the magnitude depends on the maximum amplitude and the duration of the earthquake which scale in a definite unique way. For the case of low-frequency events, the slow waves trapped in the conduit produce oscillations for a much longer time at the stations. Thus, this scale overestimate the magnitude of the events, i.e. we link a certain amplitude with a considerably larger duration, which is outside the domain where this magnitude scale is applicable. In other words, they do not follow the scaling laws between duration and amplitude needed to apply this method (Del Pezzo et al., 2013). In addition, full waveform moment tensor inversions cannot provide a reliable result either, since the low-frequency component is not related to the rupture process itself. In both cases the seismic moment would be overestimated

since the source inversion process retrieves a longer source time function than the actual one. However, moment tensor inversion (MTI) studies have been performed on long period events with a pulse-like waveform, which show short durations. In such cases, MTI can accurately estimate the source parameters (Eyre et al., 2013; Lanza and Waite, 2018b; Lokmer et al., 2007), however, the waveforms at Soufrière Hills are different showing a clear resonance effect (Neuberg et al., 2000).

To estimate the seismic moments, we produce synthetic seismograms with software Specfem3D (Tromp et al., 2008) (Fig. 3.8) which uses the spectral element method to approximate the solutions at discrete spectral elements (hexahedra) of 200 m. We tested the results provided by the software by analysing waveforms at different stations for simple point sources (DC, ISO), the amplitudes and polarisations are consistent with the radiation patterns for each case, the same way that for QSEIS in Chapter 2. Moreover, this software has been used extensively by the scientific community and the results are trusted (Peter et al., 2011, and references therein). We include in the Appendix A: Meshfem input files, Specfem input files, together with examples of multiple sources and stations.

By using the full-ring moment tensor retrieved in Chapter 2 (Eq. 2.6) and the station configuration at Montserrat,

$$\begin{pmatrix} -0.63876163 & -0.00100669 & -0.00162279 \\ -0.00100669 & -0.64001079 & -0.00107827 \\ -0.00162279 & -0.00107827 & -0.42704211 \end{pmatrix} \times M_0$$

where $M_0 = [1.71 \times 10^{11}, 1 \times 10^{12}]$ Nm. By using the linearity between the amplitude and the seismic moment (Eq. 1.11), we can find a linear relationship between M_0 and A_{max} for a single station, e.g. MBLG. We obtain the slope of the linear equation by using the synthetics modelled from these two values of M_0. We use a medium with constant properties and the topography of Montserrat. The source time function used is 2.4 with 1 Hz cut-off frequency. The main parameters used for the modelling are summarised in Table 3.1. The elastic parameters were selected to ensure a rigidity of 2.1 GPa as proposed by Heap et al. (2020) for volcanic edifices and the depth of the events following the locations by De Angelis and Henton (2011); Neuberg et al. (2006),

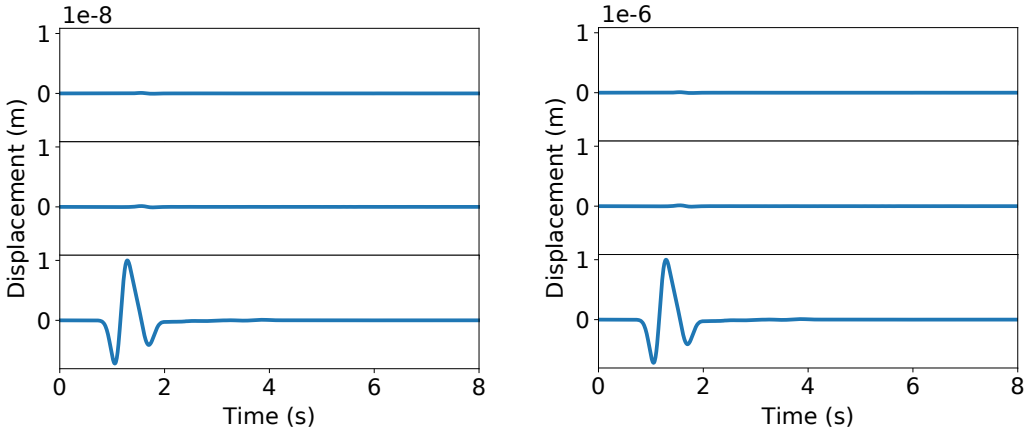

Figure 3.8: Example of synthetic seismograms at Soufrière Hills for two events with different magnitudes and same moment tensor at station MBLG. Each panel shows the east, north and upward component. Note that the waveforms are the same, only the amplitudes vary.

Bulk density ρ (kg/m^3)	1240
v_{P} (m/s)	2250
v_{S} (m/s)	1300
Rigidity μ (GPa)	2.1
M_0(Nm)	1.71×10^{12}
Depth Event (km)	0.5 and 0.2
Frequency (Hz)	1

Table 3.1: Parameters for forward modelling. The elastic parameters were selected to ensure a rigidity of 2.1 GPa as proposed by Heap et al. (2020) for volcanic edifices and the depth of the events following the locations by De Angelis and Henton (2011); Neuberg et al. (2006).

Each maximum amplitude observed A_{max} is mapped into a seismic moment M_0, hence, all the events lie on the linear plot shown in Fig. 3.9. The relationships for each focal depth are the following,

$$
\begin{aligned}
M_0 &= 9.66 \times 10^{16} \times A_{\max} \quad \text{, for 0.5 km depth} \\
M_0 &= 5.83 \times 10^{16} \times A_{\max} \quad \text{, for 0.2 km depth}
\end{aligned} \tag{3.2}
$$

hence, we can relate the maximum amplitudes for each event in our catalogue to a point source seismic moment which needs to be scaled to account for the shape of the rupture, i.e. multiplying by a factor of 42 for full-ring ruptures. We calculate the slip at the fault for each event by using the empirical law in Eq. 3.1, to finally, discuss the feasibility of the individual and total displacements within the conduit and compare them with the total movement of magma.

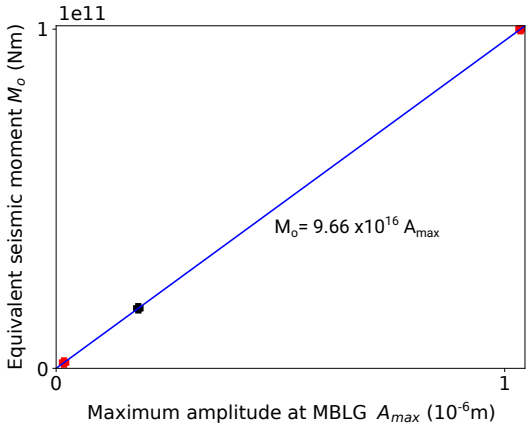

Figure 3.9: Linear relationship used to estimate the seismic moment of events at 0.5 km depth from the maximum amplitude observed at station MBLG. In red we show the data points for the seismic moments modelled and in black the average value for seismic moment for our catalogue, which needs to be corrected for a full-ring rupture.

3.5 Magma volume estimation

Similarly to continuous creep in a tectonic fault zone, where earthquakes contribute only a fraction of the slip along the fault, seismic low-frequency events are only

triggered when the continuous magma flow in the conduit reaches a critical velocity such that shear stress overcomes the shear strength of the magma. In order to link seismicity to magma flux at depth and observed extrusion rate at the surface, we need to estimate this fraction of seismic slip contributing to magma ascent. First we need to link magma flux at depth comprising volatiles, crystals and melt to the observed, so-called dense rock equivalent (DRE) of extruded material. We consider a pipe flow in a cylindrical conduit in which magma is ascending with the velocity profiles shown in Fig. 3.10. The aim of this calculation is to obtain an approximate value for the total volume at 1.5 km depth (measured from the top of the volcano) (Neuberg and O' Gorman, 2002), which comprises volatiles and melt. Using typical parameters in Table 3.2. ρ_{MELT}, T and molar mass are common values for silicic volcanoes (Neuberg and O' Gorman, 2002). The values for n_{TOTAL} and R follow Thomas and Neuberg (2014),

Parameter	Value
Melt density (ρ_{MELT})	2300 kg/m^3
Temperature of magma (T)	1123 K
% of volatiles (n_{TOTAL})	$[4.5; 5.5; 6.5]\%$
Molar mass H_2O (M_{m})	18.015×10^{-3} kg/mol
Conduit radius (R)	15 m

Table 3.2: Parameters for conduit flow model. ρ_{MELT}, T and molar mass are common values for silicic volcanoes (Neuberg and O' Gorman, 2002). The values for n_{TOTAL} and R follow Thomas and Neuberg (2014).

First we estimate the pressure at depth, assuming the pressure to be the sum of magma-static (lithostatic) plus the excess pressure exerted by the magma reservoir. We approximate the magma-static pressure using the melt density,

$$P = \rho_{\mathrm{MELT}} g h = 2300 \times 9.81 \times 1500\mathrm{Pa} = 33.8\mathrm{MPa}, \tag{3.3}$$

where ρ_{MELT} is the density of the melt, g the acceleration of gravity and h the depth. We assume that the dominant volatile present is water given by the range $n_{\mathrm{TOTAL}} = [4.5\%, 6.5\%]$. This range is based on the work by Thomas and Neuberg

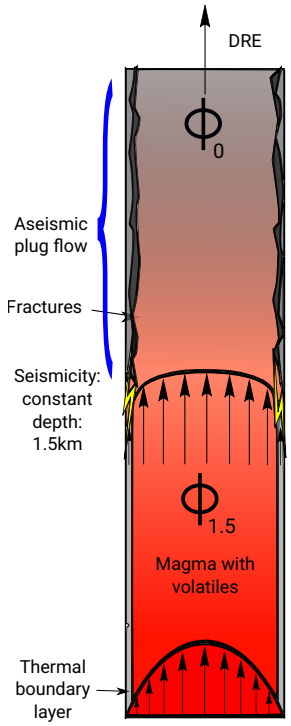

Figure 3.10: Scheme showing the kinematics of the magma ascent in three stages: parabolic flow at depth, seismically active magma flow and aseismic plug flow. $\Phi_{1.5}$ and Φ_0 are the flux at 1.5 km and at the surface denoted by dense rock equivalent (DRE).

(2014), however, it is a source of large uncertainties that we will discuss in Chapter 5. The bulk density ρ_{BULK} is given by (Neuberg and O' Gorman, 2002),

$$\frac{1}{\rho_{\text{BULK}}} = \frac{1 - n_{\text{eg}}}{\rho_{\text{MELT}}} + \frac{n_{\text{eg}}}{\rho_{\text{g}}} \tag{3.4}$$

where the gas density ρ_{g} is derived from the ideal gas law, the fraction of exsolved gas n_{eg} from the solubility law. Assuming a total water content of $[4.5\%, 5.5\%, 6.5\%]$, the bulk density results in $[1337.7; 1115.5; 956.6]$ kg/m^3 and the gas fraction in the range of,

$$\chi = \frac{\rho_{\text{BULK}}}{\rho_{\text{g}}} n_{\text{eg}} = [0.43; 0.53; 0.6] \tag{3.5}$$

this shows that for the parameters in Table 3.2, the volume of magma at 1.5 km depth is around twice the degassed volume observed and measured at the surface (Wadge et al., 2014). This estimation allows us to calculate the magma flux at depth, which is compared with the cumulative slip produced by the trigger of low-frequency earthquakes.

3.6 Magma flux

Wadge et al. (2014) have reported the volume erupted from the volcano during the five stages of the eruption, with roughly one measurement per day. The value provided is the dense rock equivalent (DRE) which considers the magma completely degassed at the surface, i.e. melt and crystals. The total volume reported is 1.063×10^6 m^3, which over the whole period represents an average extrusion rate of 4.5 m^3/s. For this study, we focus on a particular dome collapse event on June 25th, 1997, and the seismicity that led to it. On June 24th and 25th, the erupted material is 0.71×10^6 m^3 and 0.11×10^6 m^3 (Fig. 3.5), respectively. As we calculated in Section 3.5, at 1.5 km depth, the gas occupies 50% of the total volume, hence, the value 0.82×10^6 m^3 at the surface is doubled to account for volatiles at this depth, i.e. 1.64×10^6 m^3. For this estimation we use mass continuity, since the melt at surface represents 99% of the total mass, therefore, we do not consider the mass of volatiles exsolved near the surface. Finally, the extrusion is assumed to occur in a time frame of 30 hours, thus, we can calculate the displacement of the magma using this time frame and the equation of magma flux $\Phi_{1.5}$ at this depth passing through the conduit,

$$\Phi_{1.5} = \frac{v}{t} = \frac{1.64 \times 10^6 \text{ m}^3}{30 \times 3600 \text{ s}} \approx 15 \text{ m}^3/\text{s} \tag{3.6}$$

where V is the total volume and t the time. Similarly,

$$\Phi_{1.5} = Av = A\frac{d}{t} \rightarrow d = \frac{\Phi_{1.5} t}{\pi R^2} \approx 2 \text{ km} \tag{3.7}$$

where A is the cross-sectional area of the conduit, and v the average ascent velocity. This result shows that magma moved 2 km upwards to finally emplace 0.82×10^6 m^3 of material at the surface. In addition, we see in Fig. 3.10, that magma at the centre of the conduit moves faster than at the boundaries, therefore, the biggest contribution to the volume extruded is through its centre. The material ascending near the conduit wall is a small percentage of the total movement.

3.7 Full-Ring slip estimations

So far, we obtained the net ascent of the magma column which explains the magma extrusion measurements provided by Wadge et al. (2014), but, how important is brittle failure in magma during this process? Can we effectively estimate the magma extrusion from observed high-frequency phases in low-frequency seismicity?

We use the linear relationship between the maximum amplitudes observed at MBLG and the seismic moment of a point source (Eq. 3.2) to obtain an estimation of the seismic moment assuming a point source M_0. Then, by using the empirical relationship found by Murotani et al. (2013) (Eq. 3.1) we can calculate the slip at the fault for each event. Later, we calculate the seismic moment and the slip for a full-ring rupture by applying the correction found in Chapter 2 for full-ring ruptures. The results are summarised in the following: Table 3.3 for 0.5 m depth and Table 3.4 for 0.2 m depth.

	Point source assumption	Full-ring assumption
Average seismic moment	1.77×10^{11} Nm	7.44×10^{12} Nm
Average seismic slip	$\sim 3 \times 10^{-3}$ m	$\sim 3.8 \times 10^{-2}$ m
Cumulative seismic moment	4.64×10^{13} Nm	1.95×10^{15} Nm
Cumulative slip	~ 0.84 m	~ 10 m

Table 3.3: Summary of results: seismic moment estimations and slip for each case using 0.5 km depth events.

	Point source assumption	Full-ring assumption
Average seismic moment	1.07×10^{11} Nm	4.5×10^{12} Nm
Average seismic slip	$\sim 1 \times 10^{-3}$ m	$\sim 3.5 \times 10^{-2}$ m
Cumulative seismic moment	2.8×10^{13} Nm	1.18×10^{15} Nm
Cumulative slip	~ 0.2 m	~ 8.6 m

Table 3.4: Summary of results: seismic moment estimations and slip for each case using 0.2 km depth events.

Regardless of the nature of the empirical law derived for large earthquakes, the results obtained for the slip of each event on a full-ring rupture are consistent

with geological observations made by Tuffen et al. (2003) in Torfajökull volcano, Iceland. They measured faulting processes in an exhumed dyke which shows slip values of the order of centimetres.

The area of rupture is constant through the process since the seismicity is stable, i.e. the same location and the same source, therefore, each rupture occurs within the section of magma that takes the position of the previously fractured section. Tuffen et al. (2003) and Neuberg et al. (2006) also considered the effect of healing of the fractured magma. Due to the high temperature, the evolution of the system can be intermittent between fracturing and healing processes, this is a plausible scenario since the temporal separation of these events are long enough for the magma to heal < 3 s.

We can observe from the results in Table 3.3 that the values are very low compared to the total ascent due to magma flow, hence, magma ascent is mainly aseismic. Although the seismicity is recurrent, the rupture areas, the slip at the fault and therefore the seismic moments at ring ruptures are small.

We can separate the flux in 2 regimes, the first and most important is the flow ascending through the centre of the conduit where the magma behaves as a fluid with an average velocity of 2×10^{-2} m/s. For a parabolic flow, the maximum velocity is twice this value, i.e. 4×10^{-2} m/s, or smaller if a more realistic plug flow is considered. At the thermal boundary layer, near the conduit walls, a high temperature gradient promotes crystallisation which in turn stimulates brittle failure. The ascent within this layer is slower and the velocity tends to zero at the walls (Fig. 3.10). If the magma moved by the rate of seismicity alone, it would ascend with a velocity of only 9.26×10^{-5} m/s. This comparison gives an idea of how much of the flow motion is transferred into seismic energy for an average earthquake, which is at least 2 orders of magnitude smaller. We can use this ratio of ascent velocities to estimate the magma extrusion from seismicity, when brittle failure of magma is triggering the low-frequency events.

3.8 Discussion

We successfully apply a methodology to represent the trigger of low-frequency seismicity and relate its slip at the fault with magma ascent estimations. We estimate

the seismic moments of low-frequency events observed Soufrière Hills volcano in Montserrat between 22nd and 25th of June, 1997, by comparing the maximum amplitudes observed with the maximum amplitudes produced by synthetic full-ring sources. Subsequently, we calculate the slip values for each event and discuss their feasibility. Furthermore, we compare the cumulative slip with the total magma ascent which explains the extrusion reported by (Wadge et al., 2014).

We show that the seismic moments and slip values for brittle failure in magma cannot be represented by planar faults. The slip values retrieved assuming these type of faults are one or two orders of magnitude smaller than observations (Tuffen et al., 2003), therefore, they cannot explain the physics of the source. A full-ring rupture is a better source model since it allows us to assume a higher slip at the source without increasing the amplitudes observed at different stations. For example, the slip produced by a planar fault would be smaller than 1 mm on average, according to the empirical law proposed by Murotani et al. (2013). The full-ring rupture produces a seismic moment per event of 7.44×10^{12} Nm and a slip which is consistent with geological observations of $\sim 4 \times 10^{-2}$ m (Tuffen et al., 2003). The same authors estimated a seismic moment on a planar fault of 3.16×10^{8} Nm by using a larger rigidity. Here, we constrain the trade-off between rigidity and slip by lowering the rigidity due to the high temperature at the conduit and the highly fractured country rock of the edifice (Heap et al., 2020). The area of rupture (ring) we propose is considerably larger ($\times 10\pi$) than their estimation, hence, the average seismic moment is four orders of magnitude larger.

The cumulative slip value $d_{\mathrm{T}} \approx 10$ m, over the 30 hours of seismicity, is very small compared to the total displacement of the magma column. Conduit flow is usually modelled using a parabolic velocity profile (Turcotte and Schubert, 2014), thus, the velocity is higher at the centre of the conduit. We can perturb the velocity profile by considering a thermal boundary layer at the edges of the conduit (Collier and Neuberg, 2006), hence, the profile is flattened at the centre and goes to zero abruptly only near the boundaries (in the thermal boundary). The total flow calculated in Section 3.6 is the superposition of the conduit flow, considering the magma as a fluid, and the slip at the ring fault when it shows brittle behaviour. Previous studies have focused on the dynamics of the movement, and the possible values of viscosity needed to observe brittle failure (De Angelis and Henton, 2011).

Our approach is kinematic, which is easy to observe and model, especially to implement in a volcano observatory. The ratio between the magma ascent by slip and the magma erupted is $\approx 1/200$, which can give us an idea of the proportion of magma that ascends as a fluid. With this result, it is evident that the magma ascent is mainly aseismic, even though the seismicity is intense, the total slip is very low compared to the magma flow.

Previously, Green and Neuberg (2006) analysed continuous data which allowed them to identify a larger number of low-frequency events during the same period of time as our study. This is due to the possibility to apply post-processing identification techniques and overcome problems related to the seismic-to-noise ratio, which is much more computationally expensive to apply in real-time. The authors found 973 events of the same family we analysed, acting in the same period of time. In Fig. 3.11 we observe the real velocity amplitudes recorded for each family studied, especially the family A (in red), which we are interested in. The mean maximum velocity amplitude is approximately 0.85×10^{-4} m/s. Thus, by using the same methodology described in Section 3.4, we can calculate the cumulative seismic moment by using the average maximum amplitude for the 973 events. The results are shown in Table 3.5, and are consistent with the results obtained with our catalogue. The same conclusions can be made for a complete catalogue of events since we observe that the slip at a planar fault is too small compared to previous geological observations of healed fractures in solidified dykes at Torfajökull (Tuffen et al., 2003), on the other hand, the ring fault can explain the slip and the wave amplitudes observed.

	Point source assumption	Full-ring assumption
Average seismic moment	4.56×10^{11} Nm	1.91×10^{13} Nm
Average seismic slip	$\sim 1.2 \times 10^{-3}$ m	$\sim 5.4 \times 10^{-2}$ m
Cumulative seismic moment	4.44×10^{14} Nm	1.86×10^{16} Nm
Cumulative slip	~ 1.17 m	~ 52 m

Table 3.5: Summary of results using Green and Neuberg (2006) seismic data: seismic moment estimations and slip for each case.

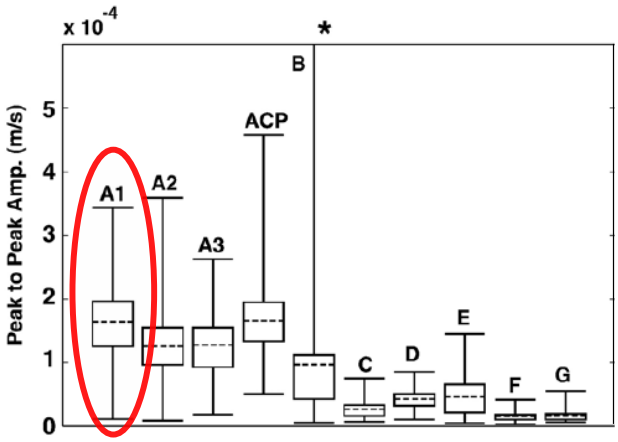

Figure 3.11: Amplitude peak-to-peak range for each family in Green and Neuberg (2006) in velocity. We are interested in family A, which has mean peak-to-peak velocity of $\sim 1.7 \times 10^{-4}$ m/s. The mean amplitude is $\sim 0.85 \times 10^{-4}$ m/s.

From this analysis, we can infer another important issue, which is the completeness of the seismic catalogue. The data we analysed was stored by using a trigger method, which omits a big percentage of events occurred since the signal-to-noise ratio may be too low. This is particularly problematic in volcanic environments, where some long-lasting signals can increase the seismic amplitude average values over days or weeks, e.g. tremor signals, thus, the individual events might be hidden. The availability of continuous data and/or a complete seismic catalogue is vital for seismologists, alongside with computational resources. This method can greatly benefit volcano observatories when a complete seismic catalogue of low-frequency events is available, especially when extrusion data are not provided.

Our calculations are developed by using the full-ring rupture assumption, thus, all point source seismic moments are scaled by the same factor, i.e. $\times 42$, satisfying linearity between the seismic moment and amplitudes. The implication of this assumption on the uncertainties are discussed in Chapter 5. Since the area of the cylinder is small, it is unlikely that a larger strain rate is achieved only in one section of the conduit. Nonetheless, if we consider ruptures with different arc lengths the relationship between seismic moment and amplitudes is not linear and the correction factor needs to be applied for each earthquake separately. Moreover,

as we discussed in Chapter 2, partial-ring ruptures show radiation patterns similar to DC sources, therefore, we have to consider an accurate fault strike in order to correctly estimate the amplitudes at each station, which makes the process of seismic moment estimation much more difficult. Finally, there will be intrinsic uncertainties in such cases, since we do not have a tool to differentiate sources showing 1/4- and 3/4-ring ruptures (Contreras-Arratia and Neuberg, 2019).

The constrained results we provide in this section can lead to new horizons in volcano seismology since we describe a method and quantify the relationship between seismicity and magma ascent. Especially in developing countries where seismic monitoring might be the only tool available and considering that it can be run with just a few seismic stations. For such cases, we can either estimate the volume extruded by using a minimum of one station, if the seismicity behaves similarly to the low-frequency events at Soufrière Hills, or following this study, calibrate the ratio seismic slip to magma ascent for a particular volcano if data for extrusion rates (DRE) are available. This estimation can be improved by using several stations and applying statistical analysis to estimate average values of magma extrusion and their uncertainties.

3.9 Conclusions

We successfully related the occurrence of a particular family of low-frequency events to magma ascent. The ascent process is dominated by the magma flow, the slip at the fault contributes a small proportion of the total movement. The small displacements at the fault are consistent with previous geological observations which validate our approach (Tuffen et al., 2003).

For a complete catalogue of seismic events, the seismicity represents less than 3% of the total movement. Although the slip at the fault is minuscule, we can extrapolate the value of the vertical displacement and obtain an estimation of the total extrusion. If a volcano observatory identifies and counts low frequency events with a robust method in real time, this method can be implemented with no significant computational cost. The ratio of total seismic slip to vertical magma movement needs to be calibrated for each particular volcano and a particular time frame, to accurately estimate the magma ascent.

Chapter 4

Towards Reconciling Seismic and Geodetic Moment Estimations: Case Bárðarbunga

We have studied the theoretical considerations and an application of the results to a stratovolcano, these cases consider ring faults with a radius of the order of tens of meters, therefore, the location of a representative point source is coincident with the structure itself, considering the uncertainties of the problem. In this chapter, we investigate if the results shown in Chapter 2 are applicable to ring faults with diameters of several kilometres. We found that the results are strongly dependant on the seismic network used, nevertheless, we can find reliable results using networks with special features. The results obtained follow a similar interpretation to ring faults for conduit size structures, however, the problem present intrinsic complications we must overcome. This chapter is based on the article "Towards reconciling seismic and geodetic moment estimations", which is accepted for publication at Journal of Volcanology and Geothermal Research.

4.1 Introduction

The energy released by an earthquake is given by the seismic moment M_0 which for a planar fault is linearly dependent on the average slip on the fault $\overline{d}$, the rupture

area A and the shear modulus of the surrounding rock μ (Aki and Richards, 2002). If the rupture area is small compared to the wavelength the earthquake can be considered as taking place in a point in space i.e. point source. However, as the area increases, the approximation is no longer valid and the description of the earthquake needs a representation of the rupture area as the superposition of several point sources (extended fault model). In this study we focus on a special case of rupture, ring faults, with caldera-size dimensions with diameters of about 5 km.

We apply the ring-fault model proposed by Contreras-Arratia and Neuberg (2019) to the Bárðarbunga caldera collapse, explaining more accurately the geometrical problem, moment tensor (MT) inversions and seismic moment estimation. It is evident that the Bárðarbunga caldera as a whole is formed by a non-perfect ring fault. For small events, the curvature of the rupture area is negligible and therefore can be explained by a single double couple (DC) (Ágústsdóttir et al., 2019), on the other hand, for bigger ruptures, the curvature comes into play and a more complex model is needed to explain the observations. Moreover, MT solutions reported for these events (Gudmundsson et al., 2016; Riel et al., 2015) include an important Compensated Linear Vector Dipole (CLVD) component, which Ekström (1994) attributed to outward dipping ring-fault ruptures. Thus, these MT solutions can be a good indicator that curved-ruptures are applicable.

Previous results on the 2014 Bárðarbunga caldera collapse support the idea of an aseismic collapse (Riel et al., 2015) since the cumulative seismic moment reported during the collapse is one or two orders of magnitude smaller than the geodetic moment obtained from InSAR measurements (Gudmundsson et al., 2016). This implies creeping slip at the caldera rims or a tremor-like superposition of events forming a slow slip event. These processes are very likely to occur, therefore, there is always a discrepancy when comparing seismic and geodetic moment. Here we propose that the partial wave interference produced by the radiation of different point sources plays an additional role in being responsible for the low value of the seismic moment. By applying the ring-fault model we re-calculate the areas of rupture for each event and determine the cumulative seismic moment, which can then be compared to the geodetic moment.

4.1.1 Ring faults: conduits

We showed previously (Contreras-Arratia and Neuberg, 2019), that partial- or full-ring ruptures, with a radius of tens of meters (conduits), cannot be directly represented by a single-source model. The planar geometry of a classic point source produces the highest amplitudes, however, increasing the fault curvature while keeping the rupture area constant result in decreasing amplitudes. Thus, if we assume a planar seismic source instead of the real curved source, the seismic moment is systematically underestimated. Moreover, the waveforms produced by opposed double couples at close proximity (dyke and full-ring) are the time derivative of the waveform predicted by the source theory in the far-field. This implies that if we assume a planar fault framework, an MT inversion returns the derivative of the actual slip history. Finally, the MT solutions for these curved sources return dominant isotropic (ISO) components, which points to a reorganisation or change of volume, respectively, regardless of the pure shear nature (DC) of the ruptures.

Ekström (1994) studied the MT components produced by outward-dipping ring faults after the isotropic component was set to zero, he found a trade-off between DC and CLVD components while varying the dipping angle. Nettles and Ekström (1998); Shuler and Ekström (2009); Shuler et al. (2013a,b) reported vertical- and sub-vertical-CLVD focal mechanisms at Bárðarbunga, Nyiragongo, Rabaul, Tungurahua, Miyakejima, among others. These results were explained by ring fault rupture models. Shuler et al. (2013a) proposed the inclusion of the isotropic component in the analysis, they consider a trade-off between isotropic and CLVD, alongside with smaller DC contribution, which can be a more appropriate description. In this study, we use the classic decomposition of the moment tensor to be a summation of the ISO, CLVD and DC components. The isotropic component represents homogeneous tension or pressure forces, i.e. explosion and implosion, respectively. The sum of all components (ISO, DC and CLVD) represents the 100% of the seismic moment.

4.1.2 Caldera collapse: Bárðarbunga, 2014-2015

The Bárðarbunga caldera is located in central Iceland under a tensional stress regime due to divergent Eurasia and North American plates with direction 106°

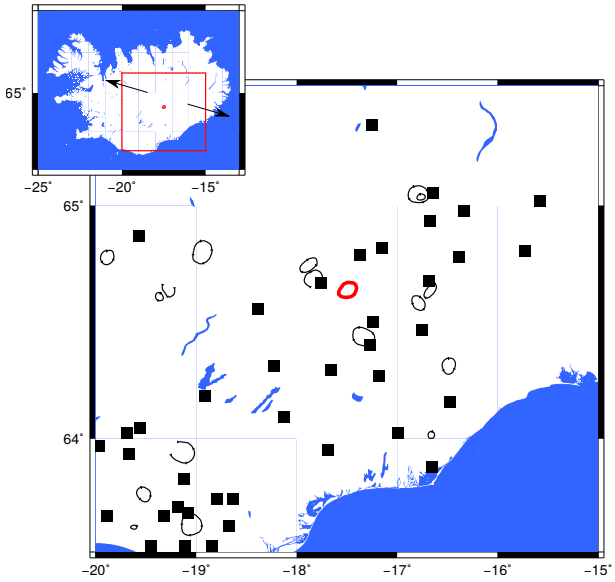

Figure 4.1: Map of Iceland, and the location of Bárðarbunga caldera in red and other volcanic systems in the area in black. Black squares are the locations of the Icelandic Meteorological Office (IMO) seismic stations. In addition, the black arrows show the direction of plate divergence.

and a rate of 18.2 mm/yr (DeMets et al., 2010). The divergence plus a mantle plume located just below Iceland are the driving mechanisms for all the volcanism in the island (Jenkins et al., 2018). It is covered by the Vatnajökull glacier of around 500 - 700 m thickness, it has an elliptical shape with main axes of 8 and 11 km. Gravity studies (Gudmundsson and Högnadóttir, 2007) have shown that its roof aspect ratio, which comprises gabbroic intrusions, is fairly low (height/width $= 5/11 \sim 0.5$), i.e. the caldera roof is thin and wide. This is also supported by Ágústsdóttir et al. (2019) who locate the brittle-ductile transition at $6 - 7$ km depth. It has been reported 26 eruptions during Holocene, none of them located at the caldera, instead the magma finds its way outside the caldera and erupt in the vicinity. The lava erupted is mainly Tholeiitic basalt but some cross-contamination with more evolve magmas is possible, due to interconnections with Torfajökull volcanic system (Larsen et al., 2015). A detailed figure of the region is shown in Fig. 4.1.

During a caldera collapse of these characteristics, special fault systems develop

at the boundaries (Roche et al., 2000). Acocella (2007) defined stages to explain this kind of caldera formation process (Fig. 1.8), according to experiments, calderas evolve from an initial downsag type (stage 1) collapse showing no seismicity followed by thrust faults developed at the boundaries (stage 2), later, a combination of the two previous stages is developed (stage 3) and finally, normal faults are created outside the pre-existing reverse faults (stage 4). Previous studies of the seismicity at Bárðarbunga showed tensional, vertical CLVD focal mechanisms supporting the conceptual model at stage 2 of caldera formation (Nettles and Ekström, 1998; Tkalčić et al., 2009).

Ágústsdóttir et al. (2019); Gudmundsson et al. (2016); Riel et al. (2015) studied seismicity during the 2014-2015 collapse which was concentrated at both the north-northwest and southern parts of the caldera. In summary, the seismicity was interpreted as normal DC solutions for small events $M_{\mathrm{W}} > 4.5$, whereas for bigger events, non-DC component (CLVD and ISO) become dominant (Rodriguez Cardozo et al., 2018). Most focal mechanisms show vertical pressure axes (stage 4, normal faulting according to Acocella (2007)) and can be explained by inner dipping normal ring-faults. Gudmundsson et al. (2016) calculated the cumulative seismic moment for the whole caldera collapse process as $M_0 = 5.07 \times 10^{18}$ Nm, and the geodetic moment $M_0^{(g)}$ in the range of 4×10^{19} Nm for a rigidity of $\mu = 2$ GPa and 4×10^{20} Nm for $\mu = 20$ GPa, assuming a total average slip at the ring-fault of 60 m and a vertical extent of the ring-fault of 12 km. Parks et al. (2017) have recalculated slip distribution at the boundaries of the caldera, finding an average slip of 40 m. Moreover, Ágústsdóttir et al. (2019) have localised all the seismicity associated with the collapse, finding the brittle-ductile transition at 6 km depth, delimiting the bottom of the ring-fault, in contrast to the previous estimation (Gudmundsson et al., 2016).

4.2 Methodology

By analysing the reported features of seismicity at Bárðarbunga (Ágústsdóttir et al., 2019; Gudmundsson et al., 2016; Riel et al., 2015), we suspect that ring faults are activated due to the non-DC components reported. We create synthetic seismograms for partial- and full-ring ruptures using Specfem3D (Tromp et al.,

2008) (introduced in Chapter 3). We represent curved fault surfaces by a superposition of single DC point sources with seismic moment $M_0 = 4 \times 10^{20}$ Nm, following the methodology described in Contreras-Arratia and Neuberg (2019) and Chapter 2. Our study is divided into two parts, which are described as follows:

- In order to obtain MT components, we simulate extended partial-ring ruptures with a radius of $R = 3.5$ km and constant inward dip of 60° for three different rake angles $\lambda = [-45°, -90°, -135°]$ (negative for normal faults). The strike varies from consecutive point sources in 10° increments, forming a 1/4-ring rupture centred at azimuth −15°. To assure coherent waves (condition 2.3), we use a slip function of 40 s, therefore, P, S and near field phases arrive in one single wave package. We use two synthetic seismic networks to record these events, the first emulates the real Icelandic Meteorological Observatory (IMO) seismic network (Fig. 4.2a and b), and second, an ideal network covering sufficiently azimuth and take-off angles, the latter defined with respect to the vertical upward axis (Fig. 4.2c). The aim is to reproduce the MT solutions observed in nature (Riel et al., 2015; Rodriguez Cardozo et al., 2018) with our complex rupture models.

- In order to study how the magnitude of an event is affected by the curvature of the source we consider 1/4-, 1/2-, 3/4- and full-ring ruptures with radius $R = 3.5$ km, 60° inward dip and −90° rake. The sources in all cases are separated by 5° angular arc, therefore, the ruptures are represented by 18, 36, 54 and 72 sources, respectively. We calculate their seismic moments using the IMO network, which provides acceptable results for magnitude estimation. We compare them with the seismic moment of a single source multiplied by the number of point sources composing the ring-ruptures. The ratio of the seismic moment produced by a planar source divided by the seismic moment of the same-size curved fault M_0^P/M_0 gives us a correction factor which can be applied to compensate for the underestimated rupture area, i.e. seismic moment.

The period used for the slip function was selected to avoid errors during the inversion by satisfying the Fraunhofer diffraction condition (Aki and Richards,

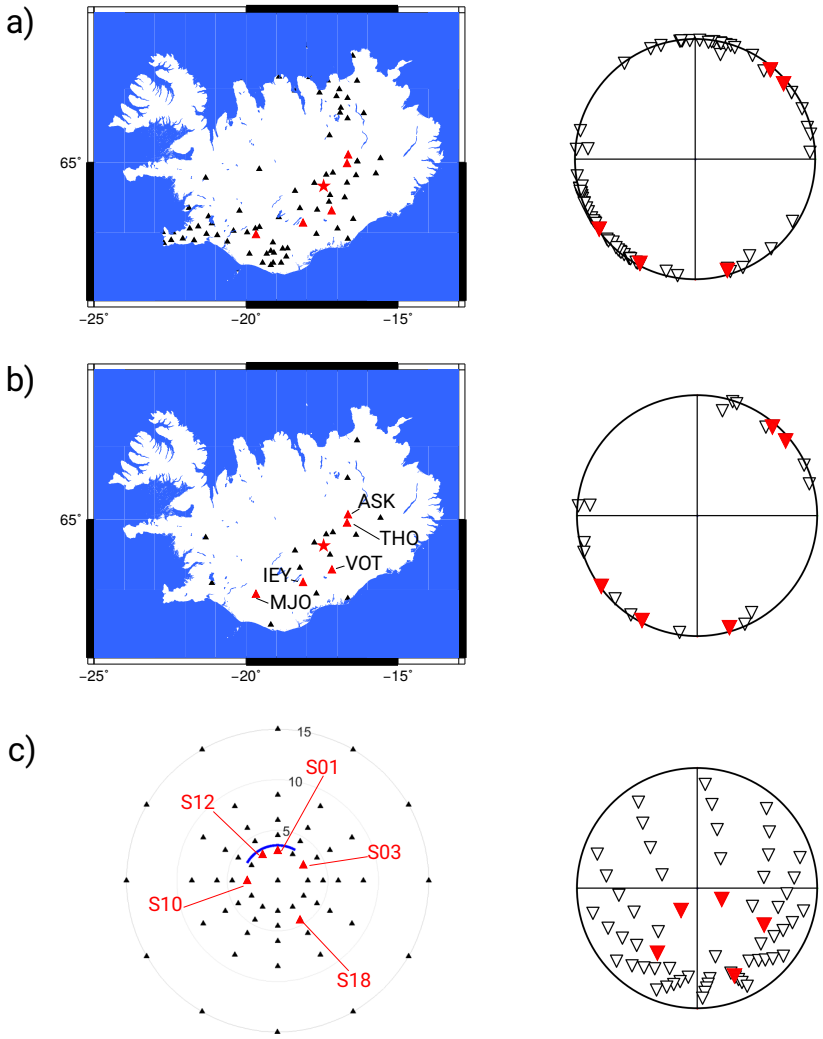

Figure 4.2: Station locations used for modelling in geographical coordinates (black triangles) and in the focal sphere (inverted white triangles). Red triangles are the stations used to show waveform match in Fig. 4.4. The red star is the location of the modelled curved-source earthquake. a) Icelandic Meteorological Office (IMO) stations and their locations on the focal sphere. b) Subset of IMO, actually used for seismic moment estimations and their locations on the focal sphere. c) Ideal network simulated, with stations up to 15 km away and a very good focal sphere coverage. Arc in blue shows the rupture simulated.

2002), which ensures a stationary interference pattern (condition 1.12 and 2.3). The shape of the extended-source waveform can be seriously deformed if the period and therefore the wavelength is not long enough. Shorter wavelengths are observed in nature and give important information about the dimensions of the source, however, for our analysis, we need to low-pass filter the signals in order to apply point source MT inversions. Here, we simplify the problem by using the same source time function for all the sources, however, they can be different in shapes and durations. We can perform the same study with different wavelengths only if the shortest wavelength satisfies the same conditions 1.12 and 2.3.

The waveforms obtained from the forward modelling are subjected to MT inversions using the software package KIWI (Cesca et al., 2010) (introduced in Chapter 2). This returns the mathematical representation of the best DC solution and the full moment tensor, both based on a point source approach. No source time function is calculated. The Green's functions were created using the software package Fomosto with QSEIS backend (Heimann et al., 2019; Wang, 1999) and a Gaussian wavelet in a half-space medium. The analysis of the moment tensors returned is based on the focal mechanisms showing information about the deviatoric MT, the seismic moment related to the magnitude, and the so-called lune plot which gives information of the full moment tensor (Tape and Tape, 2012).

The focal mechanisms provided by the KIWI software are based on the deviatoric components only (DC + CLVD) and indicate the polarisation on a focal sphere, which contains information about the principal axes for each source. In contrast, the lune plot shows the full moment tensor solution, where the deviatoric components are aligned at 0° latitude between the DC at the centre and CLVD at the edges (second row Fig. 4.3). The latitude position of the solution gives a measure of the importance of the ISO component (explosion at the top, implosion at the bottom). The focal mechanism dominated by isotropic components (white or black "beachball") cannot provide any information on the principal axes. The same is valid for the lune plot, which is only a map representation of the importance of each component of the moment tensor. Therefore, both representations, focal mechanisms and lune plots are complementary. In any case, we label the solutions as consistent if two conditions are satisfied: (i) the vertical forces for the CLVD and isotropic component must have the same sign and (ii) the deviatoric solution

must be consistent with solutions for partial ring rupture proposed by Ekström (1994). The solutions which do not satisfy these conditions are labelled as biased due to artefacts introduced by the network configuration.

Finally, using the seismic moments calculated for different arc ruptures at Bárðarbunga, we estimate the correction factor for the seismic moment under the assumption of the respective partial-ring rupture. The underestimation of the seismic moment by assuming a planar fault can be important while comparing the cumulative seismic moment with the geodetic moment of the whole caldera collapse process. By definition, these quantities give information about the seismic energy radiated and the strain energy, only for planar faults, therefore, their direct application to ring faults can lead to misinterpretations.

4.3 Results: Bárðarbunga caldera collapse

In this section, we show the MT solutions and the seismic moment estimations for each case. The aim is to contrast information given by different synthetic seismic networks when we analyse a volcanic event similar to the ones that occurred at Bárðarbunga during 2014, regarding its dynamics and magnitudes. The results, described in the next two paragraphs, are obtained by using the seismic networks shown in Fig. 4.2b and c. The results of the source inversion are shown in Fig. 4.3 and summarised in Table 4.1 and 4.2.

- Moment tensor estimations: The MT inversions show contradictory results when using these three different seismic networks. The ideal network shows a consistent superposition of DC, CLVD and ISO (mostly implosion, i.e. negative diagonal components of the MT) for all three rake angles (Table 1). By analysing the deviatoric component shown by the focal mechanisms in the first row of Fig. 4.3c, we observe that the pressure axis returned by the inversion software is consistent with previous studies (Ekström, 1994) and the directions of the slip vector. Moreover, considering that the individual faults modelled are normal (negative rake angles) the semi-vertical pressure axes are consistent with the dominant isotropic component (implosion) shown in the lune plots (second row in Fig. 4.3c). In contrast, the IMO network

and its subset provide solutions which are not consistent with the theory postulated by Ekström (1994) i.e. rake angles are not compatible with pressure/tension axes in the focal mechanism solutions (first row in Fig. 4.3a and b). Furthermore, the lune plots (second row in Fig. 4.3a and b) show inconsistent results for the ISO component by only varying the rake angle, which is a clear artefact due to the station configuration and the absence of seismic stations in the proximity of the caldera. In other words, we should not expect such a dramatic change in the full moment tensor, only by changing the rake angle 45°. Finally, in Fig. 4.4, we show the match between the seismograms and the synthetics predicted by the source models for the three inversions and five stations each. For all the networks the fit appears to be very good, regardless of how different the source models are.

- Seismic moment M_0 estimations: The seismic moment estimations obtained by the two networks also show incompatible results. On one hand, the ideal network, which retrieves a good quality MT estimation, fails to provide a realistic seismic moment estimation, due to a concentration of energy inside the ring fault. All individual contributions to the radiation interfere constructively inside the ring, i.e. focusing effect (Contreras-Arratia and Neuberg, 2019), which is a direct result of the geometry and not of the seismic energy released by the earthquake. This can be observed in Fig. 4.5b, where the amplitude profiles for curved sources in red and black exhibit unusual larger amplitudes for proximal stations. When we compare these profiles with a point source profile (such as the shown in blue), lead to an overestimation of the seismic moment and therefore the magnitude of the event, i.e. the seismic moment needs to be very high to fit the red or black curves with a power-law such as the blue curve. Moreover, the fact that the ring fault and the point source used as hypocentre for the MT inversion are not at the same location (Fig. 4.5a) results in an increase of the misfits for all source parameter estimations. Nevertheless, the seismic moments obtained by the IMO network can be trusted, since for long epicentral distances the amplitude decay is similar for a point source and a ring source, reducing the effect of the geometry in the seismic moment estimation. In summary, we calculate

the seismic moment by using seismograms from stations at long epicentral distances, thus, the complex fault can be seen as a point source.

- The seismic moments calculated for different partial ruptures with rake $= -90°$ in a caldera-size ring are shown in Table 4.2. The ratio between the seismic moment of a planar rupture and the seismic moment of the same area but curved M_0^P/M_0, gives us the value needed to correct the seismic moment returned by the inversion. Thus, we can obtain a seismic moment which accurately estimates the real rupture area. In all cases the ratio is bigger than one, therefore, the apparent seismic moment increases. In our previous study, we obtained correction factors for conduit-size ring-faults in the range of 1.1 for a 1/4-ring to 42 for a full-ring rupture (Contreras-Arratia and Neuberg, 2019). For caldera-size ring-faults, we obtain correction factor in the range 2.9 to 9.7, respectively (Table 4.2). If we assume that all events in a caldera-size fault are 1/4-ring ruptures, the cumulative seismic moment for planar faults needs to be multiplied by 2.9 to obtain the seismic moment with the real rupture area. On the other hand, if we assume only full-ring ruptures, the correction approaches one order of magnitude. The corrections for ring ruptures follows the same principle, the source magnitude is underestimated. However, correction factors for conduit-size and caldera-size are dramatically different, hence, the application of this conceptual model for different ring sizes needs to be modelled for each particular case.

Rake	DC %	CLVD %	ISO %	M_0 IMO network	M_0 ideal network
$-45°$	8	32	60	3.87×10^{14} Nm	3.00×10^{15} Nm
$-90°$	7	28	65	5.73×10^{14} Nm	1.14×10^{15} Nm
$-135°$	15	20	65	5.36×10^{14} Nm	1.23×10^{15} Nm

Table 4.1: MT solutions for three 1/4-ring ruptures with different rake values in a caldera-size ring-fault using the ideal network. Also, their magnitude estimation using the subset of IMO and ideal networks, these networks are shown in Fig. 4.2b and c.

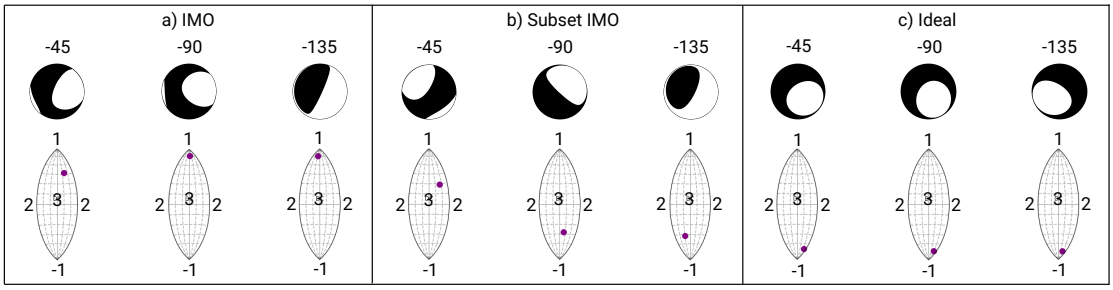

Figure 4.3: Analysis of the results provided by inversion software: Focal mechanisms showing the deviatoric components of the MT solution and lune plots showing the full MT solution (dark dots). Three 1/4-ring ruptures with 60° dip and different rake angles were analysed ($\lambda = [-45°, -90°, -135°]$). For lune plots, 1: Explosion (positive isotropic component: tensional forces), -1: Implosion (negative isotropic component: pressure forces), 2: CLVD and 3: DC.

Source	Inverted seismic moment M_0	Same size planar fault M_0^P	M_0^P/M_0
1/4-ring	2.79×10^{15} Nm	8.17×10^{15} Nm	2.93
1/2-ring	4.35×10^{15} Nm	1.60×10^{16} Nm	3.68
3/4-ring	3.16×10^{15} Nm	2.45×10^{16} Nm	7.75
full-ring	3.37×10^{15} Nm	3.27×10^{16} Nm	9.7

Table 4.2: Seismic moment calculated for different arc length ruptures, the seismic moment for the analogue planar fault and their correction coefficient used to calculate the apparent seismic moment.

4.4 Discussion

In Chapter 2, we showed that classical methods for inversion of seismic sources cannot be directly applied to non-planar ruptures since problems arise when the shape of the fault is oversimplified. However, understanding the link between these complex sources and the results given by different software packages is of major importance, since we can quantify the uncertainties in moment tensor inversions and apply corrections. Furthermore, after modelling extensively different cases of ring ruptures, we can analyse the results obtained using different seismic networks and evaluate whether they are suitable for further analysis or they lead to

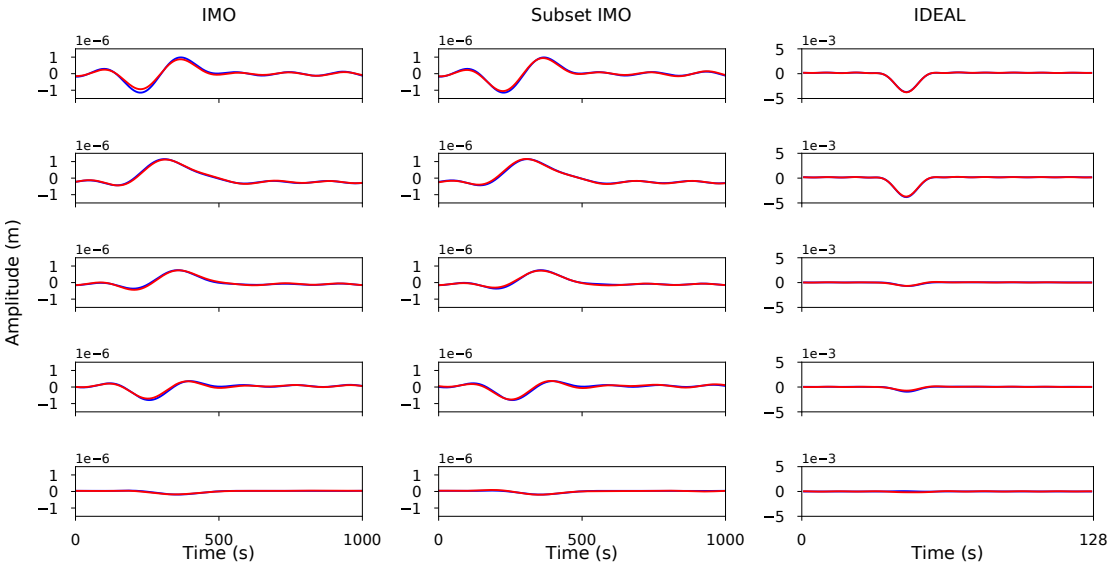

Figure 4.4: Examples of waveform match between input seismograms (blue) and synthetics produced by the inversion software (red). We show vertical seismograms, however, all three components at each station were used to obtain the MT solutions. The match is very good for the three inversions and all the stations. (Left) For the source inverted using the IMO network, we show waveforms from station VOT, THO, ASK, IEY and MJO (Fig. 4.2b). (Centre) For the source inverted using the subset of IMO stations, we show waveforms from the same previous stations. (Right) For the ideal network, we show waveforms from the stations S01, S13, S03, S10 and S18 (Fig. 4.2c). Note that the fit appears to be very good regardless of the type of the source model returned. For the first two cases, we used a lowpass filter of 0.005 Hz corner frequency. For the last case, a lowpass filter with 0.08 Hz corner frequency. Note that the time scales are different.

a completely wrong interpretation of the modelled processes.

4.4.1 MT calculations and network configuration

The ambiguity in the MT results and seismic moment estimations obtained with different network configurations need to be considered and acknowledged. For small earthquakes, for which the point source approximation is valid, we obtain

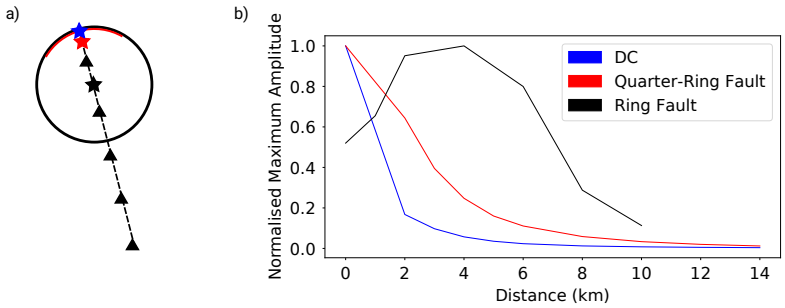

Figure 4.5: Maximum amplitude as a function of the epicentral distance for different faults. a) Scheme showing 3 ruptures: point source DC (blue), 1/4-ring rupture (red) and full-ring rupture (black). The stars show schematically the epicentres for each case, which were calculated from a joint inversion (localisation and MT), note that the epicentres are not located on the fault. The triangles represent seismic stations. b) Normalised maximum amplitudes as a function of epicentral distance. Every MT inversion software uses a point source approach, which tries to fit an amplitude profile similar to the blue line, to the data of our curved sources in red and black. Therefore, proximal stations force the software to overestimate the amplitudes and the magnitude due to the focusing effect inside the caldera. On the other hand, distal stations accurately estimate the magnitude since the dependence of the amplitude decay is similar in this domain.

well-constrained MT solutions when the focal sphere of the event is sufficiently covered, Lanza and Waite (2018a) indicates that the ideal number of well-distributed seismic stations is 8. For example, earthquakes at Bárðarbunga are shallow, thus, distant seismic networks do not span the focal sphere adequately. We showed in Fig. 4.2a and b that the IMO network correctly spans the azimuthal angles, but the take-off angle coverage is limited, spanning only values around 90°. Thus, the lack of seismic stations in the proximity of the epicentre affects the MT calculation, providing biased results. On the other hand, the ideal network sufficiently covers the focal sphere (Fig. 4.2c), providing results that can be further analysed. In addition, the inversion software returns a variety of solutions depending on the network considered. Although, they all show a very good fit to the data (Fig. 4.4) we select as the reliable result the one returned for the ideal network, since it

supports the solution provided by Ekström (1994) for partial-ring ruptures. The good match for different sources returned was previously reported by Sindija and Neuberg (2019), who studied the performance of MT inversions for different network configurations and sources at Montserrat, West Indies. In many cases, their results fit the data but failed to retrieve the moment tensor components, hence, we suggest that a good match between input seismograms and synthetics returned from the inversion is not necessarily an indicator of the quality of the inversion.

Complexities during the inversion process arise when the events are shallow compared to the radiation's wavelength. The focal mechanisms for each point source show dip-slip faulting, which according to Kanamori and Given (1981) present intrinsic uncertainties when the MT inversion is performed. In these cases the seismic moment and the dip angle of the fault are poorly constrained due to the lack of radiation produced by the components M_{xz} and M_{yz}, only the factor $M_0 \sin(2\delta)$ can be accurately calculated (Tsai et al., 2011). Despite the dip-slip nature of the individual sources, the superposition of all contributions is represented mainly by the diagonal of the MT (ISO + CLVD components). Thus, shear components are small compared to the diagonal values, as it is shown for the DC percentages ranging from 8% to 15% for 1/4-ring ruptures in Table 4.1. Although this effect is intrinsic for MT inversions of shallow earthquakes, in our case, their effect is minimal.

An alternative method to our point source MT inversion is the multiple moment tensor inversion (Tsai et al., 2005) which allows us to calculate the real source parameters of every section on the curved source, which can provide an incredibly detailed description. However, by applying the corrections calculated here, we use a simple method that can account for the destructive interference observed. Furthermore, for the application to Bárðarbunga case, our goal is to calculate the cumulative seismic moment, therefore, only the overall value of the seismic moment is needed, not individual sections.

An important limitation of our modelling is the oversimplification of our elastic medium as a half-space with constant velocity, this means that ray paths are straight lines, i.e. no refraction occurs. In this situation, the rays radiated downwards cannot reach the surface, thus, that information is lost. In real seismic applications, velocity structures produce refraction of waves and we can completely

cover the focal sphere, obtaining better-constrained results. More work has to be done considering these propagation effects, but they are beyond the scope of this study.

4.4.2 Magnitude estimation and earthquake location

Another aspect which affects the MT inversion is the size of the fault and its proximity to seismic stations, for magnitude estimation, the point source approximation must be valid. The size of the rupture must be very small compared to the distance of observation, assuming long wavelengths. Geometrically, the point source location that minimises the misfit of a full-ring rupture is its centre, even though no fault is located there. For small conduit-size ring faults, the location is accurate since the horizontal misfit is bigger than the diameter $D \sim 40$ m of the ring. On the other hand, for caldera-size rings, the point source location is several kilometres away from the actual fault, this produces an artefact in the source parameter estimations. In some extreme cases, the amplitudes can increase by a large amount with distance, and they are not correlated with the radiation patterns or the geometrical spreading, e.g. the black profile in Fig. 4.5b.

In Fig. 4.5b, we show the maximum normalised amplitudes produced by a 1/4-ring fault at different distances, by a full-ring rupture (black line) and by a DC point source (blue line). At small epicentral distances, the trend of the amplitude profiles look extremely different, let alone the actual amplitudes. Every MT inversion software is based on a point source approach, regardless of the calculation algorithm, they minimise the misfit between the seismograms and the wavefield produced by the source model. The forward model produced by the MT solution shows a point source amplitude profile (such as the blue line), thus, this profile's shape is used to interpret the data generated by 1/4-ring and full-ring ruptures, which show focusing effect, i.e. profile showing larger amplitudes at proximal stations. Therefore, in order to minimise the misfit in the estimation, the software provides a result one order of magnitude larger than for distal stations (Table 4.1), i.e. the software inversion systematically overestimates the M_0 to fit the amplitudes observed. For distal stations, the decay looks very similar for a point source and a 1/4-ring rupture and eventually for a full-ring rupture at longer distances.

Hence, the effect of the fault curvature is reduced at larger distances and the point source approximation retrieves a seismic moment that can be further analysed. This implies that the application of the correction factor still relies on the point source approach, which is valid at long distances. In this way, the local focusing effect at proximal stations is avoided.

In contrast to the result for MT inversion, where proximal stations performed better, seismic moment estimations are better constrained when we use distal stations. This leads to the obvious and simple conclusion that an adequate analysis of moment tensors together with a correct determination of seismic moments which considers complex fault ruptures can only be achieved with sufficiently dense seismic networks that cover a wide area.

4.4.3 Cumulative seismic moment at Bárðarbunga

The trapdoor caldera collapse at Bárðarbunga produced a maximum subsidence of 65 m at the centre of the caldera (Gudmundsson et al., 2016). Even though the seismicity is concentrated at the north-northwest segment and at the southern segment, Parks et al. (2017) calculated slip around the whole ring structure obtaining an average value of 40 m. Previous studies claimed that the caldera collapse happened mainly aseismically (Riel et al., 2015), due to the difference of more than two orders of magnitude between the smaller seismic moment M_0 and the geodetic moment $M_0^{(g)}$ (Ágústsdóttir et al., 2019; Gudmundsson et al., 2016; Riel et al., 2015). However, seismicity is assumed to be planar in all previous studies, which is a good approximation when the rupture area is small compared to the size of the caldera. In contrast, for bigger rupture areas, the curvature of the fault affects the radiation patterns and the seismic moment is always underestimated (Contreras-Arratia and Neuberg, 2019).

Gudmundsson et al. (2016) reported the cumulative seismic moment for the caldera collapse as 5.07×10^{18} Nm. We correct this value assuming that partial ring rupture occurs over all the extent of the perimeter (1/4-, 1/2, 3/4-, full-ring ruptures), with a mean rupture arc of around 90°. Therefore, we propose the apparent seismic moment to be $2.9 \times 5.07 \times 10^{18}$ Nm $= 1.5 \times 10^{19}$ Nm. As mentioned above, Gudmundsson et al. (2016) calculated the geodetic moment in

the range of 4×10^{19} Nm to 4×10^{20} Nm depending on different values of rigidity μ. For our synthetic experiments we use $\mu = 10$ GPa which leads to a value of 2×10^{20} Nm, which we use as an upper bound. The vertical extent of the fault needs to be reduced from 12 km to 6 km (Ágústsdóttir et al., 2019) and the slip from 60 m to 40 m (Parks et al., 2017). With all these corrections we obtain a geodetic moment between 1.4×10^{19} Nm and 6.67×10^{19} Nm, which are now in the same order of magnitude as the seismic moment. Furthermore, Heap et al. (2020) have proposed a method to rescale elastic moduli in volcanic environments, e.g. the rigidity is estimated to be 2.1 GPa, which is approximately the lower bound for seismic moment proposed by Gudmundsson et al. (2016). Therefore, we postulate that the seismic and geodetic moments match for smaller and more realistic elastic moduli in volcanic settings; however, for larger rigidity values, normally used in seismology, the geodetic moment is $4-5$ times larger than the total seismic moment during the caldera collapse.

If we consider the upper bound, the discrepancy between the geodetic (larger) and the seismic (smaller) moments can be explained by slow earthquakes (Brooks et al., 2006) on lubricated faults (Brodsky and Kanamori, 2001), or fault creeping that produce a tremor-like seismic signal (Rubin et al., 1999). Here we propose that considering only big events $M_{\mathrm{W}} > 4$ at the rim of the caldera, the cumulative seismic moment can be corrected to obtain a larger value, now in the same order of magnitude than the geodetic moment.

4.5 Conclusions

We proved that the direct application of planar fault theory is not appropriate for curved fault seismic sources. However, we can identify clues to conclude that curved sources are acting, such as a moment tensor showing a combination of isotropic and compensated linear vector dipole components.

The network configuration is crucial to obtain reliable results. In order to obtain a good representation of the moment tensor, proximal stations are needed. In addition, distal stations are needed for a good seismic moment estimation. Hence, we need a sufficiently good seismic network with stations covering a wide area around the volcano.

Moment tensor results for different kind of ruptures in a caldera-size ring-fault show a deviatoric tensor which is dominated by a compensated linear vector dipole component, however, the isotropic component is the most important, as it is shown in the lune plots in Fig. 4.3c. The deviatoric tensor shows sub-vertical pressure axes, which supports the conclusion by Ágústsdóttir et al. (2019) of normal faults acting, and give insight that the Bárðarbunga caldera is in stage 4 of evolution according to the model of Acocella (2007).

Our modelling shows that the seismic moment estimation using a point source approach underestimates the magnitude of the earthquakes, which needs to be corrected in order to account for the real rupture area. This correction estimates a seismic moment that matches the geodetic moment for small rigidity values. However, for intact rock properties commonly used in seismology, the discrepancy can be up to a factor of 5. This contrast previous estimations that show a seismic moment of around 1% to 10% of the geodetic moment, showing a closer match between these energy estimates of the same process.

We prove that a ring-fault conceptual model can be successfully used to explain seismicity in caldera-size ring-faults. It needs to be carefully applied together with forward modelling in order to exploit its full potential. Future work could also address, the real shape of rims instead of a perfect ring and a stratified media to better constrain the MT solution.

Chapter 5

Discussion

5.1 Under which assumptions is a point source approach good enough to describe complex sources?

In this thesis, I study the effect of curved source geometry on the radiation observed and how this radiation is interpreted by software packages that retrieve source parameters under a point source assumption. I consider complex sources that can be acting at volcanic environments. First, conduits follow the conceptual model proposed by Neuberg et al. (2006) or Iverson et al. (2006), where brittle behaviour or stick-slip movement at the boundaries produce seismic signals. In this case, the radius of the ring fault is of the order of tens of meters. Sources of these dimensions are normally treated as point sources, which gives no possibility to consider complexities at the source. In addition, I study caldera-size ring faults with a radius of the order of kilometres which have been studied as a finite source (Fichtner and Tkalčić, 2010). However, more efforts need to be done to accurately describe the physics of these sources. In both cases, I advance in the description of the seismic source by modelling its complexities as a extended source, regardless of the size of the ring fault.

Several authors have acknowledged the rupture in curved sources such as calderas (Ekström, 1994; Nettles and Ekström, 1998; Shuler and Ekström, 2009; Shuler et al., 2013a,b), in which the source parameter estimation was based on a point source approach. The moment tensor inversions (MTI) link a representative mo-

ment tensor solution that fits the data with the complex source, resulting in the force equivalent which does not match the real source dynamics. For example, the model proposed by Ekström (1994) considers an outward dipping cone with only pure shear sources (double couples, DC), however, the representative source returned by the MTI is a vertical compensated linear vector dipole (vertical CLVD). The vertical CLVD source considers a rearrangement of volume from a horizontal layer to the vertical axis, and does not have any physical similarity with the cone rupture proposed, but it explains the data when the isotropic component is set to zero. Additionally, I show in Fig. 4.4 that for different source models returned by the MTI, the data fitting is very good despite the uncertainty in the source description. Therefore, I can obtain a range of different solutions without notably affecting the misfits.

In general, a point source approach can be used to understand complex sources, however, the solutions need to be interpreted, analysed and corrected if applicable. I will further discuss these corrections in the following sections.

5.2 How to represent the radiation of complex sources?

I represent ring faults with different radii as a extended source, each point source contribution represents a vertical DC. I calculate a summation of radiation patterns and synthetic seismograms in order to understand the seismic source. The radiation patterns calculated for a full-ring rupture show similarities with single forces, regardless of the pure shear nature of each point source contribution (Contreras-Arratia and Neuberg, 2019). I found a similar solution for a dyke rupture but elongated in the dyke's axis. For the case of partial ring rupture, the solutions resemble DCs (Fig. 2.18), since partial interference occurs at the extremes of the partial rupture and only the contributions at the centre interfere constructively. For the case of partial- or full-ring ruptures with non-vertical walls, Ekström (1994) found radiation patterns similar to CLVD, therefore, a trade-off is obtained which depends on the dip angle; vertical walls linked with DC and 45° walls with CLVD. Nevertheless, the radiation patterns are the first approximation

of the real solutions, since they do not fully represent the results. The equations for radiation patterns depend only on the geometry of the source and they are not dependent on the travel time differences from each source, i.e. it is assumed that all the contributions arrive at the same time at the station, which is not a real case scenario for extended sources (Fig. 2.16).

To overcome this problem, I produce synthetic seismograms which by definition consider travel time differences when I locate individual sources at different locations. The application of this method needs to be carefully planned since non-coherent waves can be produced if the conditions 1.12 and 2.3 are not satisfied. This non-coherent superposition produces non-stationary interference patterns, which are important to understand if extended sources are acting (Fig. 1.6). However, I need to low-pass filter them in order to apply an MTI, thus, the signals are coherent and they appear to come from a point source, i.e. I force the conditions 1.12 and 2.3 to be satisfied to ensure coherency for the applicability of the point source inversion approach. If this condition is not met, the signals would contain features that indicate an extended source and the conditions to apply the MTI are not satisfied.

5.3 Moment tensor inversions

The synthetic seismograms obtained for the different complex sources shown in Fig. 2.1 are subjected to MTI to retrieve information about the source. I use the classic approach of a point source since it is widely used in volcano seismology. My goal is to check if this approach is directly applicable to complex sources, if it can be applied with extra considerations or if it is completely inapplicable.

Results for all sources and radii show that the seismic moment returned is systematically underestimated (Fig. 2.16 and Table 4.2), therefore, it needs to be corrected in order to accurately describe the energy released at the source. The rupture of a certain magnitude produces a radiation pattern which will interfere with other waves and result in smaller amplitudes. Thus, the MTI, which estimates the seismic moment from observations, underestimates the real energy at the source. Additionally, I observe that the linearity between the seismic moment and the amplitudes observed is no longer valid. By considering a ring fault of 20 m

and test ruptures increasing the area with the arc length, I find that the amplitudes reach a maximum for 1/2-ring rupture. Larger ruptures increase destructive interference and reduce the amplitudes (Fig. 2.17). In the same figure, I show the amplitudes when the area is normalised (compare different shapes with the same rupture area), I conclude that the "efficiency" is higher for planar faults and decrease as the shape deviates from a plane. Finally, I stated in Chapter 2 and 4 the correction factors which need to be applied for each source, in some cases the estimated seismic moment is 42 times smaller than the real value, hence, it is an important effect that needs to be considered in order to get real slip values or rupture areas. The corrected seismic moments can be interpreted in two different ways: by maintaining the rupture area constant and apply the correction to the value of slip (Chapter 3) or, constrain the slip (or cumulative slip) and recalculate the rupture area (Chapter 4).

An important effect is observed when analysing the seismic radiation from ring geometry ruptures, it has been defined in Chapters 2 and 4 as "focusing effect" , this is shown in Fig. 2.6 and Fig. 4.5. At the centre of the ring all contributions are arriving at the same time, thus, constructive interference occurs in the vertical component. This is an effect of the source geometry and travel paths, not a real effect due to the size of the event, hence, it ought not to be considered for seismic moment estimations. The focusing effect varies depending on the nature of the point sources and their radiation patterns, it needs to be modelled using synthetic seismograms to calculate actual amplitude values, nonetheless, the positive interference occurs always at the centre of the source array (Fig. 4.5).

In terms of the moment tensor solutions, I previously mentioned studies that link conical ring faults to CLVD solutions (Ekström, 1994; Nettles and Ekström, 1998; Shuler and Ekström, 2009; Shuler et al., 2013a,b), however, those studies constrain their solutions to be only deviatoric components. Since a trade-off between CLVD and isotropic solutions has been reported (Shuler et al., 2013a, and references therein), the same authors proposed the inclusion of isotropic components to explain teleseismic observations around the world (Shuler et al., 2013b). They tested isotropic components such as tensile cracks and ring faults and discarded the action of isotropic sources by different reasons, e.g. low-viscosity values

needed for volume exchange or high overburden pressure at large depths. Additionally, by analysing the MTI results obtained for partial- or full-ring ruptures, the deviatoric solution is consistent with previous studies (Fig. 4.3, first row). Nevertheless, while considering the full moment tensor, the isotropic components dominate the solutions (Fig. 4.3, second row), even though each contribution is a pure shear source. This might be a result of using local networks with good focal sphere coverage, which cannot be resolved with teleseismic data. In summary, when ring ruptures are acting, MTI with local networks return isotropic dominant sources that need to be seen as a representative model of the whole source. For example, given that the physical mechanism at Bárðarbunga is a caldera collapse, I can interpret this as a volume reduction (implosion), rather than a reorganisation of volume from the horizontal into the vertical component (CLVD).

A potential limitation of the source models studied and moment tensor inversions is the moment-dip trade-off. Essentially, it states the impossibility to constrain with low-frequency observations the dip angle and the seismic moment for vertical or sub-vertical pure shear sources. Regardless of the pure shear nature of each contribution within the ring of sources, the net contribution is interpreted by the MTI software as ISO + CLVD components, thus, all source parameters can be accurately estimated. In general, the dip-moment trade-off can be avoided if the wavelength of the radiation is shorter than the depth of the event. This trade-off might be a problem for the case of a partial-ring rupture in conduits, however, since the source is small (conduit), smaller wavelengths can be included to solve the problem accurately. For the case of vertical walls in a caldera-size ring fault, this trade-off will inevitably influence the results, hence, they need to be carefully analysed.

Regarding the waveforms, I showed in Fig. 2.16 and 2.5 that the far-field net displacement waveform produced by two opposed point sources located in close proximity is the double derivative of the displacement at the fault, in contrast to the theory of point sources that predicts the first derivative. This result invites to be more measured when the MT results are retrieved, not always they can be directly interpreted, they can lead to a misinterpretation of the displacement at the fault which has huge implications, especially for volcano seismology. More intuitive interpretations can be the key to explain complex signals under the complex source

approach. If a point source is assumed when in reality a dyke rupture or a full-ring rupture is acting, the retrieved slip history will represent the derivative of the actual displacement at the fault. For example, a slip at the ring source modelled by a step function will produce its double derivative as displacement at the station, when inverting, a delta function will be returned as the slip history at the fault (Fig. 2.20). In this case, a real displacement at the fault with a certain offset (step function), will be misinterpreted as a movement in one direction and returning to the initial position (delta function). For the case of magma ascent estimations at Soufrière Hills, it is a notable difference, on one hand, a net upward movement of magma, or an up-down movement with no net displacement, respectively.

For the case of calderas, theoretically, the same waveforms than the conduit case are expected, however, since the period of the waves is very long satisfying the condition 2.3, all phases arrive at local stations within the same wave package. Thus, individual phases cannot be observed separately, making their identification more challenging in these environments.

Polarisations observed are consistent with moment tensor inversions (Fig. 2.16) for dyke and ring faults, the polarisations are negative everywhere within the area of study, up to 15 km epicentral distance. For partial ring ruptures with vertical walls, the polarisations show similarities with DC solutions, on the other hand, for outward/inward dipping walls polarisations are in accordance with CLVD components.

5.4 Case studies

I apply the results obtained in two case studies which will allow us to recalculate the magnitudes of the events during two intense swarm events. The first case details a conduit-size ring source at Soufrière Hills, where the corrections on the seismic moment are attributable to larger slip values. The second case describes a caldera-size source at Bárðarbunga, the corrections on the seismic moment in this case are attributable to a larger rupture area.

5.4.1 Soufrière Hills, Montserrat, West Indies

Intense seismic activity has been recorded at Soufrière Hills volcano, Montserrat, since the start of its eruption in 1995. Low-frequency events (hybrids and LPs) have been extensively recorded, White et al. (1998) reported more than 300,000 events between 1996 and 1997. I propose a full-ring rupture in order to explain the seismic trigger for low-frequency waves according to the model proposed by Neuberg et al. (2006).

I develop a simple method to estimate the seismic moment of low-frequency events by comparing their amplitudes with synthetic seismograms created using the MT shown in Eq. 2.6, which is the returned MT solution for a full-ring rupture. These seismic moments are subjected to corrections to account for the source geometry by a factor of 42. The increased seismic moment is thought to be the result of an increase in slip value. Geologic observations made by Tuffen et al. (2003) have estimated the slip within magma to be of the order of centimetres, which is consistent with values for full-ring rupture. The seismic moment for a single point source (not corrected) produces a slip of the order of millimetres, which is not consistent with these geologic observations.

The total slip calculated due to brittle slip between June 22nd and June 25th, 1997, is minuscule, it represents $< 1\%$ of the average ascent velocity. I distinguish two regions with two different ascent mechanisms: at the centre, fluid flow dominates and it ascends with average velocities of $2 \times 10^{-2} mboxm/s$, almost 200 times faster than the brittle slip rate at the boundaries $10^{-4} mboxm/s$. With continuous data (Green and Neuberg, 2006), the slip can represent up to 3% of the total ascent during period of time I study, still a small value. If the magma composition (viscosity) does not change, the same slip rate at the boundaries is expected, which can be labelled as aseismic due to the small slip values. Nevertheless, if a change in the viscosity is registered, these slip rate values can vary significantly; this means much more seismicity with the subsequent increase in slip rate is observed when viscosity is increased (De Angelis and Henton, 2011). For example, during the first years of the eruption (1996-1997), the extrusion was not important, but the low-frequency seismicity was at its peak; a colder conduit (plug) with higher viscosity could have started the movement, producing the most intense seismic period

observed during the 25 years of eruption. For this period, the slip rate must have been a higher proportion of the total magma ascent.

Although the slip rate is small compared to the total magma ascent, I propose a first-order approximation of the extrusion rate from the cumulative seismic moment observed. This needs to be calibrated for each volcano in order to estimate its baseline and temporal evolution.

5.4.2 Bárðarbunga

A caldera collapse event occurred during 2014 at Bárðarbunga, Iceland, with intense seismic activity and a maximum subsidence of $\sim$ 65 m. Small magnitude seismicity is characterised by pure-shear sources acting mostly at the NNW and the south sections of the caldera (Ágústsdóttir et al., 2019). Larger magnitude events show a clear non-DC component, mainly CLVD Ágústsdóttir et al. (2019); Gudmundsson et al. (2016); Riel et al. (2015). The cumulative seismic moment calculated by the same authors points to a very small value ($\sim$ 1%) of the geodetic moment obtained by (Gudmundsson et al., 2016). Later, studies proposed some corrections to the initial values considered for the geodetic moment estimations (Ágústsdóttir et al., 2019; Heap et al., 2020; Parks et al., 2017) which allow us to recalculate it and obtain a smaller value.

The seismic moment can be recalculated (increased) by assuming that larger ruptures are affected by the curvature of the ring fault. Since the caldera has a diameter of several kilometres it is unlikely that a full-ring rupture is acting, hence, I propose that partial-ring rupture is responsible for the radiation interpreted as non-DC. I quantify the area of rupture as a 1/4-ring rupture on average, thus, the correction factor used is 3. This assumption allows us to increase the seismic moment previously provided to be around the same value of the geodetic moment when the rigidity of the medium is low ($\sim$ 2 GPa). For cases of a more competent rock, the seismic moment can represent 1/5 of the geodetic moment, this difference can be attributed to slow ruptures (Brooks et al., 2006) on lubricated faults (Brodsky and Kanamori, 2001) or seismic tremor (Rubin et al., 1999).

The study of caldera-size ring sources has interesting implications regarding network configurations and location of the representative point source, which are

discussed in the following section.

5.5 Indirect results

Here, I focus on how moment tensor inversion (MTI) packages interpret the radiation produced by complex sources. In the following, I detail three important points that indirectly emerge from my study.

- Even if the source is extended, its radiation is subjected to point source moment tensor inversion, the location is constrained to a point in space, which for ring ruptures, is never coincident, e.g. the point source location of a full-ring rupture is at its centre, not at the perimeter. For the conduit-size ring, no practical difference needs to be considered, since the misfits in the location are larger than the size of the conduit. However, for the case of the caldera, the point source is several kilometres away from the actual fault, which produces artefacts and can lead to wrong interpretations. Ágústsdóttir et al. (2019) reported locations during Bárðarbunga collapse within the boundaries of the caldera, which can be the result of the curvature and not a physical mechanism. As it is mentioned in Chapter 4, the aspect ratio of the caldera is relatively low, this means that faults are developed at the boundaries of the ring, not within the caldera. Their results and therefore their interpretation of a piecemeal collapse might be due to the artefact I propose.

- For caldera-size events and at the same time mega ruptures, the network configuration plays a major role since results are strongly dependent on the station locations. For seismic moment estimations the previously discussed focusing effect produces an overestimation in the seismic moment, alongside the reverse amplitude profile which can be observed where the ratio distance/radius ~ 1 in Fig. 2.6. Seismic stations within the caldera boundaries record this constructive interference and force the MTI software to overestimate the magnitude. In order to accurately estimate the seismic moment, the seismic stations need to be at longer distances from the caldera, where the ring source is seen as a point source.

- At the same time, the network configuration can greatly influence the results of the MT components. I compared the results from a local network with a maximum distance between stations of 15 km which covers adequately the focal sphere (Fig. 4.2c), a regional network emulating the Icelandic Meteorological Office (IMO) network (Fig.4.2a) and a subset of it (Fig. 4.2b). The MTI using the local network returned results which are consistent with the rake angles used as input and the results obtained by Ekström (1994) (Fig.4.3c). However, for the other two regional networks, the results are not consistent with the geometry, rake angles or previous studies. Therefore, I propose that the poor coverage of the focal sphere for these shallow earthquakes overshadows an accurate representation of the returned point source, hence, the real dynamics of the ring fault cannot be captured.

5.6 Uncertainties

The moment tensor results provided in this thesis are based on minimising the misfit, i.e. returning only one solution. In general, the misfits are very small, but as we shown in Fig. 4.4, more than one solution can show a good match and the moment tensor can be misinterpreted (Sindija and Neuberg, 2019). In order to test the robustness of solutions a statistical approach can be employed obtaining a probability distribution around the best solution, e.g. a Bayesian approach. Since the software used (KIWI and VOLPIS) does not provide probability density functions (PDF), this only will be considered for future work.

We have shown that the seismic moment estimations for curved sources are a good approximation after applying the correction factors. However, the largest uncertainties come from the assumptions of the angular rupture, e.g. full-ring rupture for Soufrière Hills and 1/4-ring rupture for Bárðarbunga. Even if these assumptions are realistic, considering the symmetry and size of the system and the model of displacements, respectively, we assume large misfits due to the uncertainty in the acting rupture angle and the resulting error can reach an order of magnitude. Nevertheless, previous studies, e.g. (Parks et al., 2017; Tuffen et al., 2003) support our assumptions and validate our results as a good approximation.

Although the seismic moments are well constrained, the values for the area of rupture, slip and rigidity are not. For the case of Soufrière Hills, the area of rupture is assumed to be constant and depends on the radius of the conduit, however, the trade-off between slip and rigidity can influence significantly the estimations. The rigidity carries the largest uncertainty as one cannot assume values of intact rock since fractures and temperature of the volcanic setting are not taken into account. Efforts towards a more realistic estimation of rigidity have been made (Heap et al., 2020), and despite the inherently large uncertainties, the results are still consistent with geologic observations and, therefore, a good first order approximation. For the case of Bárðarbunga, the recalculation of the rupture area and seismic moment results in a factor of 3, which is small compared with the uncertainties in the rigidity estimation. In general the rigidity estimation is the main source of uncertainty and our models cannot constrain it accurately, therefore, the uncertainty in seismic moment estimations are related primarily to the assumption of the rigidity value and not to the recalculation of rupture area or slip.

5.7 Limitations

The methodology presented in this thesis considers radiation produced by an extended seismic source which is subjected to MTI in order to obtain a representation of this complex source under the approximation of a point source. Thus, in general, the limitations of this methodology are similar to the limitations of moment tensor inversions. This includes the previously discussed usage of an inverse method which provide solutions using probability density functions.

Since this study focuses on retrieving the source information, a half-space elastic medium is used to avoid signal contamination with path effects. However, an accurate velocity structure and topography for real cases need to be considered. The half-space used for the forward model produces straight seismic rays that do not show refraction. Therefore, the focal sphere is covered with a very small area of observation which may limit the number of stations used for inversion in a real case. In general, by considering a 1-D velocity model, distal stations can effectively span the focal sphere and more information can be included to better constrain

the problem, as can be seen from Fig. 4.2. Moreover, to compare the synthetics produced by the complex source with real data, the medium has to be accurately described in order to minimise misfits when comparing the waveforms.

In addition, the radiation's frequencies used to model the source reduce the applicability of the MTI. The dip-moment trade-off explains the uncertainties on the estimation of the vertical double couple components of the moment tensor, e.g. M_{xz} and M_{yz}, when the wavelengths considered are longer than the depth of the events. Therefore, if a short-period wavelet is used to describe the source time history, the effect of dip-moment trade-off is minimised. However, by considering shallow events or long wavelets the condition 2.3 is satisfied, but the moment-dip trade-off influences the results and uncertainties will be unavoidable. As Tsai et al. (2011) reported, these need to be studied and quantified (Tsai et al., 2011), especially for vertical faults and partial-ring rupture (Fig. 2.16).

The use of real geometries can also be considered. By using a perfect ring fault, I describe the source as a first-order approximation of the real geometry, Gudmundsson et al. (2016) showed the exact geometry of a partial ring rupture at Bárðarbunga, to explain the deformation pattern. The same geometry can be used to accurately explain the seismic wavefield for that particular event and reduce the misfits when synthetics are compared to real data.

Finally, all the point sources are normalised to the same seismic moment and displacement at the source. This description allows to determine a representative point source which can be corrected to obtain an average slip and magnitude. However, ruptures most likely have different slip values and potentially different displacements at the source. Hence, a more flexible description which allows for these heterogeneities in the rupture will improve the description and reduce uncertainties. For example, the partial-ring ruptures at Bárðarbunga should have smaller fault displacements towards the edges in the same way than for planar faults. This can be achieved by using multiple moment tensor inversions, which allows different source parameters for different sections of the fault (Tsai et al., 2005). I will develop this idea in the next section.

5.8 Future work

In this thesis, I propose a method to easily calculate the centroid moment tensor and the magnitude, slip and area of an earthquake with a complex source. To obtain a more detailed description of the rupture a multiple moment tensor inversion can be used, alongside with an inverse scheme that consider probability density functions. By increasing the number of source parameters (model parameters) I allow to differentiate sections of the rupture, however, more observations are needed to constrain them all. At the same time, some simplifications can be made, for example, for ring faults the strike of the point sources can be regularised in order to obtain a smooth variation of the strike in contiguous point sources, this can be achieved by using Tikhonov regularisation. These results can give more definite clues if ring ruptures are acting.

More work needs to be done to constrain the cumulative seismic moment during other periods with high low-frequency seismic activity at Soufrière Hills and other volcanoes around the world. By having a complete catalogue of events the slip produced by brittle failure can be estimated, subsequently, statistical analysis will allow us to find a more accurate ratio between the cumulative rupture slip and the total extrusion during a specific time window. Additionally, better methods to estimate the seismic moment of low-frequency events need to be explored, e.g. a method which retrieves the displacement at the source and magnitudes by analysing the trigger waveform, not the resonance waveform. These results can also help to constrain the values of bulk viscosity of magma at each volcano, together with its temporal evolution

In order to publish my work in Chapter 3, the correlation between cumulative seismic moment and tilt needs to be addressed. The results I found point to displacements at the fault of the order of centimetres, which can be contrasted by numerical models of magma flow and deformation. Flow models proposed by Marsden et al. (2019) can include the transient slip at the boundaries of the conduit and the tilt can be estimated, accurate values of maximum tilt produced will give us more evidence that supports the conceptual model proposed by Neuberg et al. (2006).

Finally, the discrepancy between the cumulative seismic moment and the geodetic moment can be completely solved by considering low and realistic rigidity values. Also, if the rigidity is higher, the possibility of slow earthquakes and lubrication of faults can explain this discrepancy. Contrasting long term seismic data and deformation data can help us to calculate seismic energy liberated by quasi-stationary slip of hundreds of seconds or more. Additionally, including friction studies and analysing the seismic coupling at the boundaries of the caldera can give important information about energy release.

5.9 Concluding remarks

My thesis focuses on the differences that arise when considering deviations from a planar seismic source geometry into more complex sources with conduit and caldera sizes. The seismic radiation changes due to negative interference, therefore, the moment tensor inversions will interpret this radiation in different and particular ways. The wavelength has an important effect when analysing results, if coherence is assured, the source can be seen as a point source and moment tensor inversions (MTI) can be applied. On the other hand, if waves are not coherent, it is evidence that extended sources are acting but the latter can lead to misinterpretations of the source parameters and therefore need to be filtered out.

Although, I model the complex source as a superposition of double couples (DC), the representative point source in most cases is represented by non-DC solutions. The seismic moment estimated by inversion software is systematically underestimated, the waveforms points to a different interpretation of the slip at the fault and the polarisations observed are particular for each case. If coherence is assured, corrections can be applied to the results in order to obtain a better estimation of the seismic moment, which accounts for the destructive interference modelled.

Implications for magma ascent and caldera subsidence are part of the applications of this thesis and can be further explored, especially to be implemented in volcano observatories. The link between low-frequency trigger rupture and magma extrusion can be calibrated and applied to each particular volcano. Moreover, for the case of caldera subsidence, a more accurate value of the rupture area can lead

to partially explain the deformation observed, contributing to the reconciliation of both, the seismic and geodetic moments. Finally, some indirect results point to the fact that moment tensor inversions are dependent on the network configuration, they need to be carefully analysed and interpreted, including the dynamics of the source, the magnitude of the event and its location.

References

Acocella, V. (2007). Understanding caldera structure and development: An overview of analogue models compared to natural calderas. *Earth-Science Reviews*, **85**(3-4), pp. 125–160. xi, 15, 18, 19, 81, 95

Ágústsdóttir, T., Winder, T., Woods, J., White, R. S., Greenfield, T. and Brandsdóttir, B. (2019). Intense Seismicity During the 2014–2015 Bárðarbunga-Holuhraun Rifting Event, Iceland, Reveals the Nature of Dike-Induced Earthquakes and Caldera Collapse Mechanisms. *Journal of Geophysical Research: Solid Earth*, **124**(8), pp. 8331–8357. 1, 20, 78, 80, 81, 93, 94, 95, 103, 104

Ágústsdóttir, T., Woods, J., Greenfield, T., Green, R. G., White, R. S., Winder, T., Brandsdóttir, B., Steinthórsson, S. and Soosalu, H. (2016). Strike-slip faulting during the 2014 Bárðarbunga-Holuhraun dike intrusion, central Iceland. *Geophysical Research Letters*, **43**(4), pp. 1495–1503. 1, 4, 22, 57

Aki, K. and Richards, P. G. (2002). *Quantitative seismology*. University Science Books, Sausalito, California. 700pp. 3, 5, 10, 11, 13, 14, 22, 78, 82

Aspinall, W., Miller, A., Lynch, L., Latchman, J., Stewart, R., White, R. and Power, J. (1998). Soufrière Hills eruption, Montserrat, 1995–1997: Volcanic earthquake locations and fault plane solutions. *Geophysical Research Letters*, **25**(18), pp. 3397–3400. 57

Bean, C. J., De Barros, L., Lokmer, I., Métaxian, J.-P., O' Brien, G. and Murphy, S. (2014). Long-period seismicity in the shallow volcanic edifice formed from slow-rupture earthquakes. *Nature Geoscience*, **7**(1), p. 71. 17, 57

Ben-Menahem, A. (1962). Radiation of seismic body waves from a finite moving source in the earth. *Journal of Geophysical Research*, **67**(1), pp. 345–350. 12

Brodsky, E. E. and Kanamori, H. (2001). Elastohydrodynamic lubrication of faults. *Journal of Geophysical Research: Solid Earth*, **106**(B8), pp. 16357–16374. 19, 94, 103

Brooks, B. A., Foster, J. H., Bevis, M., Frazer, L. N., Wolfe, C. J. and Behn, M. (2006). Periodic slow earthquakes on the flank of Kīlauea volcano, Hawai'i. *Earth and Planetary Science Letters*, **246**(3-4), pp. 207–216. 19, 94, 103

Cesca, S. and Dahm, T. (2008). A frequency domain inversion code to retrieve time-dependent parameters of very long period volcanic sources. *Computers & Geosciences*, **34**(3), pp. 235–246. 29

Cesca, S., Heimann, S., Stammler, K. and Dahm, T. (2010). Automated procedure for point and kinematic source inversion at regional distances. *Journal of Geophysical Research: Solid Earth*, **115**(B6). 28, 46, 84

Chevalier, L., Collombet, M. and Pinel, V. (2017). Temporal evolution of magma flow and degassing conditions during dome growth, insights from 2D numerical modeling. *Journal of Volcanology and Geothermal Research*, **333**, pp. 116–133. 16

Chouet, B. (1988). Resonance of a fluid-driven crack: Radiation properties and implications for the source of long-period events and harmonic tremor. *Journal of Geophysical Research: Solid Earth*, **93**(B5), pp. 4375–4400. 57

Chouet, B. A. (1996). Long-period volcano seismicity: its source and use in eruption forecasting. *Nature*, **380**(6572), p. 309. 2, 17, 22, 57

Chouet, B., Dawson, P., Ohminato, T., Martini, M., Saccorotti, G., Giudicepietro, F., De Luca, G., Milana, G. and Scarpa, R. (2003). Source mechanisms of explosions at Stromboli Volcano, Italy, determined from moment-tensor inversions of very-long-period data. *Journal of Geophysical Research: Solid Earth*, **108**(B1). 1, 2, 4, 22

Chouet, B. A. and Matoza, R. S. (2013). A multi-decadal view of seismic methods for detecting precursors of magma movement and eruption. *Journal of Volcanology and Geothermal Research*, **252**, pp. 108–175. 2, 17, 51

Cole, P., Smith, P., Komorowski, J.-C., Alfano, F., Bonadonna, C., Stinton, A., Christopher, T., Odbert, H. and Loughlin, S. (2014a). Ash venting occurring both prior to and during lava extrusion at Soufriere Hills Volcano, Montserrat, from 2005 to 2010. *Geological Society, London, Memoirs*, **39**(1), pp. 71–92. 57

Cole, P., Smith, P., Stinton, A., Odbert, H., Bernstein, M., Komorowski, J. and Stewart, R. (2014b). Vulcanian explosions at Soufrière Hills Volcano, Montserrat between 2008 and 2010. *Geological Society, London, Memoirs*, **39**(1), pp. 93–111. 57

Collier, L. and Neuberg, J. (2006). Incorporating seismic observations into 2D conduit flow modeling. *Journal of Volcanology and Geothermal Research*, **152**(3-4), pp. 331–346. 15, 16, 73

Contreras-Arratia, R. and Neuberg, J. W. (2019). Complex seismic sources in volcanic environments: Radiation modelling and moment tensor inversions. *Journal of Volcanology and Geothermal Research*, **381**, pp. 262–272. 3, 12, 13, 59, 76, 78, 79, 82, 86, 87, 93, 97

Costa, A., Caricchi, L. and Bagdassarov, N. (2009). A model for the rheology of particle-bearing suspensions and partially molten rocks. *Geochemistry, Geophysics, Geosystems*, **10**(3). 16

Cruz, F. G. and Chouet, B. A. (1997). Long-period events, the most characteristic seismicity accompanying the emplacement and extrusion of a lava dome in Galeras Volcano, Colombia, in 1991. *Journal of Volcanology and Geothermal Research*, **77**(1-4), pp. 121–158. 2

Cruz-Atienza, V. and Virieux, J. (2004). Dynamic rupture simulation of non-planar faults with a finite-difference approach. *Geophysical Journal International*, **158**(3), pp. 939–954. 12

Dahm, T. and Krüger, F. (1999). Higher-degree moment tensor inversion using far-field broad-band recordings: theory and evaluation of the method with application to the 1994 Bolivia deep earthquake. *Geophysical Journal International*, **137**(1), pp. 35–50. 55

De Angelis, S. and Henton, S. (2011). On the feasibility of magma fracture within volcanic conduits: constraints from earthquake data and empirical modelling of magma viscosity. *Geophysical Research Letters*, **38**(19). xii, 15, 58, 60, 63, 65, 66, 73, 102

Del Pezzo, E., Bianco, F. and Borgna, I. (2013). Magnitude scale for LP events: a quantification scheme for volcanic quakes. *Geophysical Journal International*, **194**(2), pp. 911–919. 64

DeMets, C., Gordon, R. G. and Argus, D. F. (2010). Geologically current plate motions. *Geophysical Journal International*, **181**(1), pp. 1–80. 80

Denlinger, R. P. and Hoblitt, R. P. (1999). Cyclic eruptive behavior of silicic volcanoes. *Geology*, **27**(5), pp. 459–462. 58

Donaldson, C., Caudron, C., Green, R. G., Thelen, W. A. and White, R. S. (2017). Relative seismic velocity variations correlate with deformation at Kīlauea volcano. *Science advances*, **3**(6), p. e1700219. 1

Ekström, G. (1994). Anomalous earthquakes on volcano ring-fault structures. *Earth and Planetary Science Letters*, **128**(3-4), pp. 707–712. 3, 4, 22, 53, 55, 78, 79, 85, 86, 91, 96, 97, 99, 105

Ekström, G., Nettles, M. and Dziewoński, A. (2012). The global CMT project 2004–2010: Centroid-moment tensors for 13,017 earthquakes. *Physics of the Earth and Planetary Interiors*, **200**, pp. 1–9. 7

Eyre, T. S., Bean, C. J., De Barros, L., O' Brien, G. S., Martini, F., Lokmer, I., Mora, M. M., Pacheco, J. F. and Soto, G. J. (2013). Moment tensor inversion for the source location and mechanism of long period (LP) seismic events from 2009 at Turrialba volcano, Costa Rica. *Journal of volcanology and geothermal research*, **258**, pp. 215–223. 65

Ferrazzini, V. and Aki, K. (1987). Slow waves trapped in a fluid-filled infinite crack: Implication for volcanic tremor. *J. geophys. Res*, **92**(B9), pp. 9215–9223. 2, 17, 22, 57

Feuillet, N., Nostro, C., Chiarabba, C. and Cocco, M. (2004). Coupling between earthquake swarms and volcanic unrest at the Alban Hills Volcano (central Italy) modeled through elastic stress transfer. *Journal of Geophysical Research: Solid Earth*, **109**(B2). 1

Fichtner, A. and Tkalčić, H. (2010). Insights into the kinematics of a volcanic caldera drop: Probabilistic finite-source inversion of the 1996 Bardarbunga, Iceland, earthquake. *Earth and Planetary Science Letters*, **297**(3-4), pp. 607–615. 3, 96

Goto, A. (1999). A new model for volcanic earthquake at Unzen Volcano: Melt rupture model. *Geophysical Research Letters*, **26**(16), pp. 2541–2544. 16, 17

Green, D. N. and Neuberg, J. (2006). Waveform classification of volcanic low-frequency earthquake swarms and its implication at Soufrière Hills Volcano, Montserrat. *Journal of Volcanology and Geothermal Research*, **153**(1), pp. 51–63. xii, xiii, xiv, 1, 17, 57, 58, 60, 61, 62, 74, 75, 102

Greenfield, T., White, R. S. and Roecker, S. (2016). The magmatic plumbing system of the Askja central volcano, Iceland, as imaged by seismic tomography. *Journal of Geophysical Research: Solid Earth*, **121**(10), pp. 7211–7229. 1

Gudmundsson, M. T. and Högnadóttir, T. (2007). Volcanic systems and calderas in the Vatnajökull region, central Iceland: Constraints on crustal structure from gravity data. *Journal of Geodynamics*, **43**(1), pp. 153–169. 80

Gudmundsson, M. T., Jónsdóttir, K., Hooper, A., Holohan, E. P., Halldórsson, S. A., Ófeigsson, B. G., Cesca, S., Vogfjörd, K. S., Sigmundsson, F., Högnadóttir, T. et al. (2016). Gradual caldera collapse at Bárdarbunga volcano, Iceland, regulated by lateral magma outflow. *Science*, **353**(6296), p. aaf8988. 3, 12, 18, 20, 78, 81, 93, 94, 103, 107

Hale, A. J., Calder, E. S., Loughlin, S., Wadge, G. and Ryan, G. A. (2009). Modelling the lava dome extruded at Soufrière Hills Volcano, Montserrat, August 2005–May 2006: Part II: Rockfall activity and talus deformation. *Journal of volcanology and geothermal research*, **187**(1-2), pp. 69–84. 57

Hammer, C. and Neuberg, J. (2009). On the dynamical behaviour of low-frequency earthquake swarms prior to a dome collapse of Soufrière Hill volcano, Montserrat. *Geophysical Research Letters*, **36**(6). 17, 58

Hautmann, S., Gottsmann, J., Sparks, R. S. J., Costa, A., Melnik, O. and Voight, B. (2009). Modelling ground deformation caused by oscillating overpressure in a dyke conduit at Soufrière Hills Volcano, Montserrat. *Tectonophysics*, **471**(1-2), pp. 87–95. 57

Hayes, G. P. (2017). The finite, kinematic rupture properties of great-sized earthquakes since 1990. *Earth and Planetary Science Letters*, **468**, pp. 94–100. 12

Heap, M. J., Villeneuve, M., Albino, F., Farquharson, J. I., Brothelande, E., Amelung, F., Got, J.-L. and Baud, P. (2020). Towards more realistic values of elastic moduli for volcano modelling. *Journal of Volcanology and Geothermal Research*, **390**, p. 106684. 65, 66, 73, 94, 103, 106

Heimann, S., Vasyura-Bathke, H., Sudhaus, H., Isken, M. P., Kriegerowski, M., Steinberg, A. and Dahm, T. (2019). A python framework for efficient use of pre-computed Green's functions in seismological and other physical forward and inverse source problems. *Solid Earth*, **10**(6), pp. 1921–1935. 84

Iverson, R. M., Dzurisin, D., Gardner, C. A., Gerlach, T. M., LaHusen, R. G., Lisowski, M., Major, J. J., Malone, S. D., Messerich, J. A., Moran, S. C. et al. (2006). Dynamics of seismogenic volcanic extrusion at Mount St Helens in 2004–05. *Nature*, **444**(7118), p. 439. 3, 4, 15, 22, 23, 96

Jenkins, J., Maclennan, J., Green, R. G., Cottaar, S., Deuss, A. and White, R. S. (2018). Crustal formation on a spreading ridge above a mantle plume: receiver function imaging of the Icelandic crust. *Journal of Geophysical Research: Solid Earth*, **123**(6), pp. 5190–5208. 80

Jolly, A., Neuberg, J., Jousset, P. and Sherburn, S. (2012). A new source process for evolving repetitious earthquakes at Ngauruhoe volcano, New Zealand. *Journal of volcanology and geothermal research*, **215**, pp. 26–39. 57

Jost, M. u. and Herrmann, R. (1989). A student's guide to and review of moment tensors. *Seismological Research Letters*, **60**(2), pp. 37–57. 7

Kanamori, H. and Given, J. W. (1981). Use of long-period surface waves for rapid determination of earthquake-source parameters. *Physics of the Earth and Planetary interiors*, **27**(1), pp. 8–31. 91

Kokelaar, B. (2002). Setting, chronology and consequences of the eruption of Soufrière Hills Volcano, Montserrat (1995-1999). *Geological Society, London, Memoirs*, **21**(1), pp. 1–43. 57

Kumagai, H., Chouet, B. A. and Nakano, M. (2002). Waveform inversion of oscillatory signatures in long-period events beneath volcanoes. *Journal of Geophysical Research: Solid Earth*, **107**(B11), pp. ESE–7. 2

Kumagai, H., Placios, P., Ruiz, M., Yepes, H. and Kozono, T. (2011). Ascending seismic source during an explosive eruption at Tungurahua volcano, Ecuador. *Geophysical Research Letters*, **38**(1). 1, 4, 22

Labuz, J. F. and Zang, A. (2012). Mohr–Coulomb failure criterion. *Rock mechanics and rock engineering*, **45**(6), pp. 975–979. 1

Lanza, F. and Waite, G. P. (2018a). A nonlinear approach to assess network performance for moment-tensor studies of long-period signals in volcanic settings. *Geophysical Journal International*, **215**(2), pp. 1352–1367. 11, 50, 90

Lanza, F. and Waite, G. P. (2018b). Nonlinear moment-tensor inversion of repetitive long-periods events recorded at Pacaya volcano, Guatemala. *Frontiers in Earth Science*, **6**, p. 139. 65

Larsen, G., Gudmundsson, M., Vogfjörð, K., Ilyinskaya, E., Oddsson, B. and Pagneux, E. (2015). The Bárðarbunga volcanic system. *Catalogue of Icelandic Volcanoes. IMO, UI, CPD-NCIP*. 80

Lecocq, T., Caudron, C. and Brenguier, F. (2014). MSNoise, a python package for monitoring seismic velocity changes using ambient seismic noise. *Seismological Research Letters*, **85**(3), pp. 715–726. 1

Lokmer, I. and Bean, C. J. (2010). Properties of the near-field term and its effect on polarisation analysis and source locations of long-period (LP) and very-long-period (VLP) seismic events at volcanoes. *Journal of Volcanology and Geothermal Research*, **192**(1-2), pp. 35–47. 7

Lokmer, I., Bean, C. J., Saccorotti, G. and Patane, D. (2007). Moment-tensor inversion of LP events recorded on Etna in 2004 using constraints obtained from wave simulation tests. *Geophysical Research Letters*, **34**(22). 2, 65

Loughlin, S., Luckett, R., Ryan, G., Christopher, T., Hards, V., De Angelis, S., Jones, L. and Strutt, M. (2010). An overview of lava dome evolution, dome collapse and cyclicity at Soufrière Hills Volcano, Montserrat, 2005–2007. *Geophysical Research Letters*, **37**(19). 57

Luckett, R., Loughlin, S., De Angelis, S. and Ryan, G. (2008). Volcanic seismicity at Montserrat, a comparison between the 2005 dome growth episode and earlier dome growth. *Journal of Volcanology and Geothermal Research*, **177**(4), pp. 894–902. 57

Lyons, J. J. and Waite, G. P. (2011). Dynamics of explosive volcanism at Fuego volcano imaged with very long period seismicity. *Journal of Geophysical Research: Solid Earth*, **116**(B9). 1, 51

Marsden, L. H., Neuberg, J., Thomas, M., Mothes, P. and Ruiz, M. (2019). Combining magma flow and deformation modelling to explain observed changes in tilt. *Frontiers in Earth Science*, **7**, p. 219. 16, 108

Masterlark, T. and Tung, S. (2017). Finite Element Models of Elastic Volcano Deformation. In *Volcanoes-Geological and Geophysical Setting, Theoretical Aspects and Numerical Modeling, Applications to Industry and Their Impact on the Human Health*. IntechOpen. 12

Melnik, O. and Sparks, R. (2002). Dynamics of magma ascent and lava extrusion at Soufrière Hills Volcano, Montserrat. *Geological Society, London, Memoirs*, **21**(1), pp. 153–171. 57

Mildon, Z. K., Pugh, D. J., Tarasewicz, J., White, R. S. and Brandsdóttir, B. (2016). Closing crack earthquakes within the Krafla caldera, North Iceland. *Geophysical Supplements to the Monthly Notices of the Royal Astronomical Society*, **207**(2), pp. 1137–1141. 1, 4, 23

Miller, A., Stewart, R., White, R., Luckett, R., Baptie, B., Aspinall, W., Latchman, J., Lynch, L. and Voight, B. (1998). Seismicity associated with dome growth and collapse at the Soufriere Hills Volcano, Montserrat. *Geophysical Research Letters*, **25**(18), pp. 3401–3404. 1, 17, 57

Molina, I., Kumagai, H. and Yepes, H. (2004). Resonances of a volcanic conduit triggered by repetitive injections of an ash-laden gas. *Geophysical Research Letters*, **31**(3). 22

Moré, J. J. (1978). The Levenberg-Marquardt algorithm: implementation and theory. In *Numerical analysis*. Springer, pp. 105–116. 28, 46

Murotani, S., Satake, K. and Fujii, Y. (2013). Scaling relations of seismic moment, rupture area, average slip, and asperity size for M∼9 subduction-zone earthquakes. *Geophysical Research Letters*, **40**(19), pp. 5070–5074. 63, 71, 73

Murphy, M. D., Sparks, R. S. J., Barclay, J., Carroll, M. R., Lejeune, A.-M., Brewer, T. S., MacDonald, R., Black, S. and Young, S. (1998). The role of magma mixing in triggering the current eruption at the Soufriere Hills volcano, Montserrat, West Indies. *Geophysical Research Letters*, **25**(18), pp. 3433–3436. 57

Nettles, M. and Ekström, G. (1998). Faulting mechanism of anomalous earthquakes near Bárdarbunga Volcano, Iceland. *Journal of Geophysical Research: Solid Earth*, **103**(B8), pp. 17973–17983. 3, 22, 53, 79, 81, 96, 99

Neuberg, J. (2000). Characteristics and causes of shallow seismicity in andesite volcanoes. *Philosophical Transactions of the Royal Society of London A: Mathematical, Physical and Engineering Sciences*, **358**(1770), pp. 1533–1546. 1, 17

Neuberg, J. (2011). Earthquakes, volcanogenic. In *Encyclopedia of solid earth geophysics*, volume 1. Springer Dordrecht, Netherlands, pp. 261–269. 2

Neuberg, J., Baptie, B., Luckett, R. and Stewart, R. (1998). Results from the broadband seismic network on Montserrat. *Geophysical Research Letters*, **25**(19), pp. 3661–3664. 57

Neuberg, J., Luckett, R., Baptie, B. and Olsen, K. (2000). Models of tremor and low-frequency earthquake swarms on Montserrat. *Journal of Volcanology and Geothermal Research*, **101**(1), pp. 83–104. 17, 57, 65

Neuberg, J. and O' Gorman, C. (2002). A model of the seismic wavefield in gas-charged magma: application to Soufriere Hills Volcano, Montserrat. *Geological Society, London, Memoirs*, **21**(1), pp. 603–609. 68, 69

Neuberg, J. W., Tuffen, H., Collier, L., Green, D., Powell, T. and Dingwell, D. (2006). The trigger mechanism of low-frequency earthquakes on Montserrat. *Journal of Volcanology and Geothermal Research*, **153**(1), pp. 37–50. xii, 1, 3, 4, 15, 16, 17, 22, 23, 57, 58, 59, 63, 65, 66, 72, 96, 102, 108

Okada, Y. (1985). Surface deformation due to shear and tensile faults in a half-space. *Bulletin of the seismological society of America*, **75**(4), pp. 1135–1154. 5

Okada, Y. (1992). Internal deformation due to shear and tensile faults in a half-space. *Bulletin of the seismological society of America*, **82**(2), pp. 1018–1040. 5

Okumura, S., Nakamura, M., Nakano, T., Uesugi, K. and Tsuchiyama, A. (2010). Shear deformation experiments on vesicular rhyolite: Implications for brittle fracturing, degassing, and compaction of magmas in volcanic conduits. *Journal of Geophysical Research: Solid Earth*, **115**(B6). 15, 16

Olson, A. H. and Apsel, R. J. (1982). Finite faults and inverse theory with applications to the 1979 Imperial Valley earthquake. *Bulletin of the Seismological Society of America*, **72**(6A), pp. 1969–2001. 12

Parks, M. M., Heimisson, E. R., Sigmundsson, F., Hooper, A., Vogfjörd, K. S., Árnadóttir, T., Ófeigsson, B., Hreinsdóttir, S., Hjartardóttir, Á. R., Einarsson, P. et al. (2017). Evolution of deformation and stress changes during the caldera collapse and dyking at Bárdarbunga, 2014–2015: Implication for triggering of seismicity at nearby Tungnafellsjökull volcano. *Earth and Planetary Science Letters*, **462**, pp. 212–223. 81, 93, 94, 103, 105

Peter, D., Komatitsch, D., Luo, Y., Martin, R., Le Goff, N., Casarotti, E., Le Loher, P., Magnoni, F., Liu, Q., Blitz, C. et al. (2011). Forward and adjoint simulations of seismic wave propagation on fully unstructured hexahedral meshes. *Geophysical Journal International*, **186**(2), pp. 721–739. 65

Richardson, J. P. and Waite, G. P. (2013). Waveform inversion of shallow repetitive long period events at Villarrica Volcano, Chile. *Journal of Geophysical Research: Solid Earth*, **118**(9), pp. 4922–4936. 1, 4, 23, 57

Riel, B., Milillo, P., Simons, M., Lundgren, P., Kanamori, H. and Samsonov, S. (2015). The collapse of Bárðarbunga caldera, Iceland. *Geophysical Journal International*, **202**(1), pp. 446–453. 3, 78, 81, 82, 93, 103

Roche, O., Druitt, T. and Merle, O. (2000). Experimental study of caldera formation. *Journal of Geophysical Research: Solid Earth*, **105**(B1), pp. 395–416. 18, 81

Rodriguez Cardozo, F., Hjorleifsdottir, V., Jonsdottir, K., Geirsson, H. and Iglesias, A. (2018). New insights about Bárðarbunga's seismic sources during and after the 2014-2015 caldera collapse events. In *AGU Fall Meeting Abstracts*. 81, 82

Rubin, A. M., Gillard, D. and Got, J.-L. (1999). Streaks of microearthquakes along creeping faults. *Nature*, **400**(6745), p. 635. 19, 94, 103

Ruiz, M. C., Lees, J. M. and Johnson, J. B. (2006). Source constraints of Tungurahua volcano explosion events. *Bulletin of volcanology*, **68**(5), pp. 480–490. 1, 4, 22

Salvage, R. and Neuberg, J. (2016). Using a cross correlation technique to refine the accuracy of the Failure Forecast Method: Application to Soufrière Hills volcano, Montserrat. *Journal of Volcanology and Geothermal Research*, **324**, pp. 118–133. 58

Scholz, C. H. (2002). *The mechanics of earthquakes and faulting*. Cambridge university press. 1

Shuler, A. and Ekström, G. (2009). Anomalous earthquakes associated with Nyiragongo Volcano: Observations and potential mechanisms. *Journal of Volcanology and Geothermal Research*, **181**(3-4), pp. 219–230. 53, 79, 96, 99

Shuler, A., Ekström, G. and Nettles, M. (2013a). Physical mechanisms for vertical-CLVD earthquakes at active volcanoes. *Journal of Geophysical Research: Solid Earth*, **118**(4), pp. 1569–1586. 3, 4, 22, 23, 79, 96, 99

Shuler, A., Nettles, M. and Ekström, G. (2013b). Global observation of vertical-CLVD earthquakes at active volcanoes. *Journal of Geophysical Research: Solid Earth*, **118**(1), pp. 138–164. 3, 4, 22, 23, 79, 96, 99

Sigurdsson, H., Houghton, B., McNutt, S., Rymer, H. and Stix, J. (2015). *The encyclopedia of volcanoes*. Elsevier. 18

Sindija, D. and Neuberg, J. (2019). The effect of seismic network geometry on moment tensor inversions. In *Geophysical Research Abstracts*, volume 21. 30, 91, 105

Sparks, R. and Young, S. (2002). The eruption of Soufrière Hills volcano, Montserrat (1995-1999): overview of scientific results. *Geological Society, London, Memoirs*, **21**(1), pp. 45–69. 57

Sparks, R. S. J., Young, S. R., Barclay, J., Calder, E. S., Cole, P., Darroux, B., Davies, M., Druitt, T., Harford, C., Herd, R. et al. (1998). Magma production and growth of the lava dome of the Soufriere Hills Volcano, Montserrat, West Indies: November 1995 to December 1997. *Geophysical Research Letters*, **25**(18), pp. 3421–3424. 57

Stinton, A., Cole, P., Odbert, H., Christopher, T., Avard, G. and Bernstein, M. (2014a). Dome growth and valley fill during Phase 5 (8 October 2009–11 February 2010) at the Soufrière Hills Volcano, Montserrat. *Geological Society, London, Memoirs*, **39**(1), pp. 113–131. 57

Stinton, A. J., Cole, P. D., Stewart, R. C., Odbert, H. M. and Smith, P. (2014b). The 11 February 2010 partial dome collapse at Soufriere Hills volcano, Montserrat. *Geological Society, London, Memoirs*, **39**(1), pp. 133–152. 57

SuiTung, T. M. and Lo, D. S. H. (2018). Finite element models of elastic earthquake deformation. *Earthquakes: Forecast, Prognosis and Earthquake Resistant Construction*, p. 169. 12

Tape, W. and Tape, C. (2012). A geometric setting for moment tensors. *Geophysical Journal International*, **190**(1), pp. 476–498. 84

Thomas, M. E. and Neuberg, J. (2012). What makes a volcano tick - A first explanation of deep multiple seismic sources in ascending magma. *Geology*, **40**(4), pp. 351–354. 15, 50, 58

Thomas, M. E. and Neuberg, J. W. (2014). Understanding which parameters control shallow ascent of silicic effusive magma. *Geochemistry, Geophysics, Geosystems*, **15**(11), pp. 4481–4506. 68

Tkalčić, H., Dreger, D. S., Foulger, G. R. and Julian, B. R. (2009). The puzzle of the 1996 Bárdarbunga, Iceland, earthquake: No volumetric component in the source mechanism. *Bulletin of the Seismological Society of America*, **99**(5), pp. 3077–3085. 3, 81

Tromp, J., Komatitsch, D. and Liu, Q. (2008). Spectral-element and adjoint methods in seismology. *Communications in Computational Physics*, **3**(1), pp. 1–32. 65, 81

Tsai, V. C., Hayes, G. P. and Duputel, Z. (2011). Constraints on the long-period moment-dip tradeoff for the Tohoku earthquake. *Geophysical research letters*, **38**(7). 91, 107

Tsai, V. C., Nettles, M., Ekström, G. and Dziewonski, A. M. (2005). Multiple CMT source analysis of the 2004 Sumatra earthquake. *Geophysical Research Letters*, **32**(17). 55, 91, 107

Tsvetkova, Y. D. and Melnik, O. (2018). The influence of non-Newtonian properties of magma on flow in a volcanic conduit. In *Doklady Physics*, volume 63. Springer, pp. 485–488. 16

Tuffen, H., Dingwell, D. B. and Pinkerton, H. (2003). Repeated fracture and healing of silicic magma generate flow banding and earthquakes? *Geology*, **31**(12), pp. 1089–1092. 15, 17, 63, 72, 73, 74, 76, 102, 105

Turcotte, D. L. and Schubert, G. (2014). *Geodynamics*. Cambridge University Press. 73

Varley, N., Arámbula-Mendoza, R., Reyes-Dávila, G., Sanderson, R. and Stevenson, J. (2010). Generation of Vulcanian activity and long-period seismicity at Volcán de Colima, Mexico. *Journal of Volcanology and Geothermal Research*, **198**(1-2), pp. 45–56. 57

Vasco, D. (1989). Deriving source-time functions using principal component analysis. *Bulletin of the Seismological Society of America*, **79**(3), pp. 711–730. 29

Vavryčuk, V. (2015). Moment tensor decompositions revisited. *Journal of Seismology*, **19**(1), pp. 231–252. 7

Voight, B., Sparks, R., Miller, A., Stewart, R., Hoblitt, R., Clarke, A., Ewart, J., Aspinall, W., Baptie, B., Calder, E. et al. (1999). Magma flow instability and cyclic activity at Soufriere Hills volcano, Montserrat, British West Indies. *Science*, **283**(5405), pp. 1138–1142. 58

Wadge, G., Herd, R., Ryan, G., Calder, E. and Komorowski, J.-C. (2010). Lava production at Soufrière Hills Volcano, Montserrat: 1995–2009. *Geophysical Research Letters*, **37**(19). 57

Wadge, G., Voight, B., Sparks, R., Cole, P., Loughlin, S. and Robertson, R. (2014). An overview of the eruption of Soufriere Hills Volcano, Montserrat from 2000 to 2010. *Geological Society, London, Memoirs*, **39**(1), pp. 1–40. 56, 57, 69, 70, 71, 73

Wang, R. (1999). A simple orthonormalization method for stable and efficient computation of Green's functions. *Bulletin of the Seismological Society of America*, **89**(3), pp. 733–741. 26, 84

Webb, S. L. and Dingwell, D. B. (1990). The onset of non-Newtonian rheology of silicate melts. *Physics and Chemistry of Minerals*, **17**(2), pp. 125–132. 16

White, R. S., Drew, J., Martens, H. R., Key, J., Soosalu, H. and Jakobsdóttir, S. S. (2011). Dynamics of dyke intrusion in the mid-crust of Iceland. *Earth and Planetary Science Letters*, **304**(3), pp. 300–312. 1, 4, 22

White, R. A., Miller, A. D., Lynch, L. and Power, J. (1998). Observations of hybrid seismic events at Soufriere Hills volcano, Montserrat: July 1995 to September 1996. *Geophysical Research Letters*, **25**(19), pp. 3657–3660. 57, 102

Young, S. R., Sparks, R. S. J., Aspinall, W. P., Lynch, L. L., Miller, A. D., Robertson, R. E. and Shepherd, J. B. (1998). Overview of the eruption of Soufriere Hills volcano, Montserrat, 18 July 1995 to December 1997. *Geophysical Research Letters*, **25**(18), pp. 3389–3392. 57

Appendix A

Input files

In this appendix I show examples of the input files for different software I used during my thesis.

A.1 QSEIS

```
#This is an example of the input file used, for only one source. To
consider the contribution of all sources we need to run this model
for different locations following Eq. 1.3, 1.4, 1.5. And for
different sources using different linear combinations of Myz and
Mzx.


# This is the input file of FORTRAN77 program "qseis06" for
calculation of
# synthetic seismograms based on a layered halfspace earth model.
#
# by
# Rongjiang  Wang <wang@gfz-potsdam.de>
# GeoForschungsZentrum Potsdam
# Telegrafenberg, D-14473 Potsdam, Germany
#
# Last modified: Potsdam, Nov., 2006
```

```
# Last modified by PJD: 11 Dec 2011. File name: PJD_test1_2200m
# = = = = = = = = = = = = = = = = = = = = = = = = = = = = = = = = = = =
# If not specified, SI Unit System is used overall!
#
# Coordinate systems:
# cylindrical (z,r,t) with z = downward,
#                          r = from source outward,
#                          t = azmuth angle from north to east;
# cartesian (x,y,z) with   x = north,
#                          y = east,
#                          z = downward;
# = = = = = = = = = = = = = = = = = = = = = = = = = = = = = = = = = = =
#
# SOURCE PARAMETERS
# =================
# 1. source depth [km]
#---------------------------------------------------------------------
 1.000                    |dble: source_depth;
#---------------------------------------------------------------------
#
# RECEIVER PARAMETERS
# ===================
# 1. receiver depth [km]
# 2. switch for distance sampling role (1/0 = equidistant/
#rregular); switch
#    for unit used (1/0 = km/deg)
# 3. number of distance samples
# 4. if equidistant, then start and end trace distance (> 0); else
#distance
#    list (please order the receiver distances from small to large)
# 5. (reduced) time begin [sec] & length of time window [sec],
#number of time
#    samples (<= 2*nfmax in qsglobal.h)
# 6. switch for unit of the following time reduction parameter:
```

```
#1 = velocity
#    [km/sec], 0 = slowness [sec/deg]; time reduction parameter
#--------------------------------------------------------------------
 0.000                 |dble: receiver_depth;
 0  1                  |int: sw_equidistant, sw_d_unit;
 8                    |int: no_distances;
 1.00 1.00 1.00 1.00 1.00 1.00 1.00 1.00     |dble: d_1,d_n; or
 0 3 300     |dble: t_start,t_window; int: no_t_samples;
 1  0.0                |int: sw_t_reduce; dble: t_reduce;
#--------------------------------------------------------------------
#
# WAVENUMBER INTEGRATION PARAMETERS
# ================================
# 1. select slowness integration algorithm (0 = suggested for full
#wave-field
#    modelling; 1 or 2 = suggested when using a slowness window
#with narrow
#    taper range - a technique for suppressing space-domain
#aliasing);
# 2. 4 parameters for low and high slowness (Note 1) cut-offs [s/km]
#with
#    tapering: 0 < slw1 < slw2 defining cosine taper at the lower end,
#and 0 <
#    slw3 < slw4 defining the cosine taper at the higher end. default
#values
#    will be used in case of inconsistent input of the cut-offs
#(possibly with
#    much more computational effort);
# 3. parameter for sampling rate of the wavenumber integration
#(1 = sampled
#    with the spatial Nyquist frequency, 2 = sampled with twice higher
#than
#    the Nyquist, and so on: the larger this parameter, the smaller
#the space-
```

```
#    domain aliasing effect, but also the more computation effort);
# 4. the factor for suppressing time domain aliasing (> 0 and <= 1)
#(Note 2).
#---------------------------------------------------------------------
 0                                    |int: sw_algorithm;
 0.000  0.000  0.000  0.000           |dble: slw(1-4);
 10.00                                 |dble: sample_rate;
 0.1                                  |dble: supp_factor;
#---------------------------------------------------------------------
#
#         OPTIONS FOR PARTIAL SOLUTIONS
#       (only applied to the source-site structure)
#     ========================================
#
# 1. switch for filtering free surface effects (0 = with free surface,
#i.e.,
#    do not select this filter; 1 = without free surface; 2 = without
#free
#    surface but with correction on amplitude and wave form. Note
#switch 2
#    can only be used for receivers at the surface)
# 2. switch for filtering waves with a shallow penetration depth
#(concerning
#    their whole trace from source to receiver), penetration depth
#limit [km]
#
#    if this option is selected, waves whose travel path never
#exceeds the
#    given depth limit will be filtered ("seismic nuting"). the
#condition for
#    selecting this filter is that the given shallow path depth limit
#should
#    be larger than both source and receiver depth.
#
```

```
# 3. number of depth ranges where the following selected
#up/down-sp2oing P or
#    SV waves should be filtered
# 4. the 1. depth range: upper and lower depth [km], switch for
#filtering P
#    or SV wave in this depth range:
#
#    switch no:              1      2        3       4         other
#    filtered phase:         P(up)  P(down)  SV(up)  SV(down)  Error
#
# 5. the 2. ...
#
#    The partial solution options are useful tools to increase the
#numerical
#    significance of desired wave phases. Especially when the desired
#phases
#    are smaller than the undesired phases, these options should be
#selected
#    and carefully combined.
#---------------------------------------------------------------------
 1                     |int: isurf;
 0  0.000              |int: sw_path_filter; dble:shallow_depth_limit;
# 0                    |int: no_of_depth_ranges;
 0
# 0.0 2000.0  3
# 0.0 2000.0  4
#---------------------------------------------------------------------
#
# SOURCE TIME FUNCTION (WAVELET) PARAMETERS (Note 3)
# ================================================
# 1. wavelet duration [unit = time sample rather than sec!], that is
#about
#    equal to the half-amplitude cut-off period of the wavelet (> 0.
#if <= 0,
```

```
#    then default value = 2 time samples will be used), and switch for
#the
#    wavelet form (0 = user's own wavelet; 1 = default wavelet:
#normalized
#    square half-sinusoid for simulating a physical delta impulse;
#2 = tapered
#    Heaviside wavelet, i.e. integral of wavelet 1)
# 2. IF user's own wavelet is selected, then number of the wavelet
#time samples
#    (<= 1024), and followed by
# 3. equidistant wavelet time samples
# 4  ...(continue) (! no comment lines allowed between the time sample
#list!)
#    IF default, delete line 2, 3, 4 ... or comment them out!
#---------------------------------------------------------------------
 20.0  1                      |int:dble: wavelet_duration; sw_wavelet;
# 100                         |int: no_w_samples; below dble: w_samples;
#  0.000  0.063  0.127  0.189  0.251  0.312  0.372  0.430  0.486  0.541
#  0.593  0.643  0.690  0.735  0.776  0.815  0.850  0.881  0.910  0.934
#  0.955  0.972  0.985  0.994  0.999  1.000  0.997  0.990  0.979  0.964
#  0.945  0.922  0.896  0.866  0.833  0.796  0.756  0.713  0.667  0.618
#  0.567  0.514  0.458  0.401  0.342  0.282  0.220  0.158  0.095  0.032
# -0.032 -0.095 -0.158 -0.220 -0.282 -0.342 -0.401 -0.458 -0.514 -0.567
# -0.618 -0.667 -0.713 -0.756 -0.796 -0.833 -0.866 -0.896 -0.922 -0.945
# -0.964 -0.979 -0.990 -0.997 -1.000 -0.999 -0.994 -0.985 -0.972 -0.955
# -0.934 -0.910 -0.881 -0.850 -0.815 -0.776 -0.735 -0.690 -0.643 -0.593
# -0.541 -0.486 -0.430 -0.372 -0.312 -0.251 -0.189 -0.127 -0.063  0.000
#---------------------------------------------------------------------
#
#  FILTER PARAMETERS OF RECEIVERS (SEISMOMETERS OR HYDROPHONES)
#  ===========================================================
# 1. constant coefficient (normalization factor)
# 2. number of roots (<= nrootmax in qsglobal.h)
# 3. list of the root positions in the complex format (Re,Im). If no
```

```
#roots,
#    comment out this line
# 4. number of poles (<= npolemax in qsglobal.h)
# 5. list of the pole positions in the complex format (Re,Im). If no
#poles,
#    comment out this line
#-----------------------------------------------------------------------
 1.0
 0
# (0.0, 0.0), (0.0, 0.0), (159.0,0.0)
 0
# (-0.02356, -0.02356), (-0.02356, 0.02356), (-50,0)
#-----------------------------------------------------------------------
#
# OUTPUT FILES FOR GREEN'S FUNCTIONS (Note 4)
# ===========================================
# 1. selections of source types (yes/no = 1/0)
# 2. file names of Green's functions (please give the names without
# extensions,
#    which will be appended by the program automatically: *.tz, *.tr,
# *.tt
#    and *.tv are for the vertical, radial, tangential, and volume
#change (for
#    hydrophones) components, respectively)
#-----------------------------------------------------------------------
#  explosion   strike-slip dip-slip   clvd       single_f_v  single_f_h
#-----------------------------------------------------------------------
    0           0           1          0          0           0    |int
   'ex'        'ss'        'ds'       'cl'       'fz'        'fh' |char
#-----------------------------------------------------------------------
# OUTPUT FILES FOR AN ARBITRARY POINT DISLOCATION SOURCE
#               (for applications to earthquakes)
# ======================================================
# 1. selection (0 = not selected; 1 or 2 = selected), if (selection =
```

```
1),
#then
#    the 6 moment tensor elements [N*m]: Mxx, Myy, Mzz, Mxy, Myz, Mzx
#(x is
#    northward, y is eastward and z is downard); else if (selection =
2),
#then
#    Mis [N*m] = isotropic moment part = (MT+MN+MP)/3, Mcl = CLVD moment
#part
#    = (2/3)(MT+MP-2*MN), Mdc = double-couple moment part = MT-MN,
#Strike [deg],
#    Dip [deg] and Rake [deg].
#
#Note: to use this option, the Green's functions above should be computed
#          (selection = 1) if they do not exist already.
#
#                 north(x)
#                  /
#                 /\ strike
#                *----------------------->  east(y)
#                |\                        \
#                |-\                        \
#                |  \     fault plane        \
#                |90 \                        \
#                |-dip\                        \
#                |     \                        \
#                |      \                        \
#           downward(z)  \------------------------\
#
# 2. switch for azimuth distribution of the stations (0 = uniform azimuth,
#    else = irregular azimuth angles)
# 3. list of the azimuth angles [deg] for all stations given above (if
the
#    uniform azimuth is selected, then only one azimuth angle is required)
```

```
#
#-------------------------------------------------------------------------
#    Mis        Mcl        Mdc        Strike     Dip        Rake
 File
#-------------------------------------------------------------------------
# 2 0.00       0.00   1.00e+12        0.00      90.00       -90.0   'seis'
#-------------------------------------------------------------------------
#     Mxx        Myy        Mzz        Mxy        Myz        Mzx
 File
#-------------------------------------------------------------------------
 1   0.00        0.00       0.00       0.00      0.00     1.00e+12
'test'
  8
  0 45. 90. 135. 180. 225. 270. 315.
#-------------------------------------------------------------------------
#
# GLOBAL MODEL PARAMETERS (Note 5)
# ================================
# 1. switch for flat-earth-transform
# 2. gradient resolution [%] of vp, vs, and ro (density), if <= 0, then
#default
#    values (depending on wave length at cut-off frequency) will be used
#-------------------------------------------------------------------------
 0                              |int: sw_flat_earth_transform;
 0  0  0                        |dble: vp_res, vs_res, ro_res;
#-------------------------------------------------------------------------
#
#                 LAYERED EARTH MODEL
#       (SHALLOW SOURCE + UNIFORM DEEP SOURCE/RECEIVER STRUCTURE)
# ========================================================
# 1. number of data lines of the layered model (source site)
#-------------------------------------------------------------------------
 1                           |int: no_model_lines;
#-------------------------------------------------------------------------
```

```
#
# MULTILAYERED MODEL PARAMETERS (source site)
# ===========================================
# no  depth[km]  vp[km/s]  vs[km/s]  ro[g/cm^3] qp      qs
#-----------------------------------------------------------------------------
  1   0.00       3.5000    0.30000   2.0000      1000.0  1000.0
#-----------------------------------------------------------------------------
#
#           LAYERED EARTH MODEL
#       (ONLY THE SHALLOW RECEIVER STRUCTURE)
#       ====================================
# 1. number of data lines of the layered model
#
#Note: if the number = 0, then the receiver site is the same as the
#      source site, else different receiver-site structure is considered.
#      please be sure that the lowest interface of the receiver-site
#      structure given given below can be found within the source-site
#      structure, too.
#
#-----------------------------------------------------------------------------
 0                                |int: no_model_lines;
#-----------------------------------------------------------------------------
#
# MULTILAYERED MODEL PARAMETERS (shallow receiver-site structure)
# ===============================================================
# no  depth[km]    vp[km/s]    vs[km/s]   ro[g/cm^3]   qp      qs
#-----------------------------------------------------------------------------
#  1     0.000      2.900       1.676      2.600       92.00     41.00
#  2     2.000      2.900       1.676      2.600       92.00     41.00
#  3     2.000      5.400       3.121      2.600       92.00     41.00
#  4     7.000      5.400       3.121      2.600       92.00     41.00
#  5     7.000      6.160       3.561      2.600      576.00    256.00
#  6    17.000      6.160       3.561      2.600      576.00    256.00
#  7    17.000      6.630       3.832      2.900      576.00    256.00
```

```
#  8    35.000      6.630       3.832      2.900      576.00    256.00
#  9    35.000      8.0400      4.4700     3.3198    1340.00    600.00
#---------------------------------end of all inputs----------------------
```

A.2 KIWI

```
# This is an example of input file for the Python script
# rapidinv.py
#
# Each of the following lines define inversion parameters
# These are identified by a capital alphanumeric string
# (CODES) and followed by the selected values (VALUES)
#
# All emply lines and commented lines (starting with #)
# will be ignored, as well as lines starting with
# unrecognised CODES
# For those CODES which are not assigned, default values
# will be used (see rapidinv.defaults).
# VALUES has to be correctly formatted (see rapidinv.acceptables).
# Ordering of CODES - VALUES lines is arbitrary, but if
# CODES are assigned more than one time, last assignation
# will prevail.
#

# Inversion subdirectory (where all is saved locally)
INVERSION_DIR    ../RESULTS/RING

# Greens functions
GFDB_STEP1       ../GFDB/dbFULL
GFDB_STEP2       ../GFDB/dbFULL
```

```
# Data
DATA_DIR          ../DATA/RING
DATA_FILE         RING
STAT_INP_FILE     stations-strato.dat


# Channels, components, weighting
SW_WEIGHT_DIST    False
COMP_2_USE        une
EPIC_DIST_MIN     0.
EPIC_DIST_MAX     10.

# Source location and origin time
LATITUDE_NORTH    0.0
LONGITUDE_EAST    0.0
YEAR              1970
MONTH             01
DAY               01
HOUR              02
MIN               46
SEC               40
RISE_TIME         0.2

# Inversion flow
NUM_INV_STEPS     2

# Phases windowing, step 1
PHASES_2_USE_ST1 a
WIN_START_A_ST1  0.05
WIN_TAPER_A_ST1  0.01

# Inversion of point source parameters step 1
SW_RAPIDSTEP1     True
DEPTH_1           0.1
```

```
DEPTH_2          2
DEPTH_STEP       0.1
DEPTH_UPPERLIM   0.9
DEPTH_BOTTOMLIM  1.1
STRIKE_1         0
STRIKE_2         360
STRIKE_STEP      30
DIP_1            -180
DIP_2            180
DIP_STEP         30
RAKE_1           0
RAKE_2           90
RAKE_STEP        30
SCAL_MOM_1       1e10
SCAL_MOM_2       1e14
SCAL_MOM_STEP    9e12

# Parameters for inversion step 1
BP_F1_STEP1      0.2
BP_F2_STEP1      0.4
BP_F3_STEP1      8.0
BP_F4_STEP1      10.0
MISFIT_MET_STEP1 ampspec_l2norm
INV_MODE_STEP1   invert_dmsdst

# Plot parameters for inversion step 1
MAX_STAT_2_PLOT  20
DATA_PLOT_STEP1  amsp
FILT_PLOT_STEP1  filtered
AMPL_PLOT_STEP1  norm

# Inversion of point source parameters step 2
EFFECTIVE_DT_ST2 0.1
CC_SHIFT1        -10
```

```
CC_SHIFT2         10
REL_NORTH_1       -50
REL_NORTH_2       50
REL_NORTH_STEP    10
REL_EAST_1        -50
REL_EAST_2        50
REL_EAST_STEP     10
REL_TIME_1        -2
REL_TIME_2        2
REL_TIME_STEP     1

# Parameters for inversion step 2
BP_F1_STEP2       0.2
BP_F2_STEP2       0.4
BP_F3_STEP2       8.0
BP_F4_STEP2       10.0
MISFIT_MET_STEP2 l2norm
INV_MODE_STEP2    grid
INVERS_MET_STEP2 minimize_lm

# Phases windowing, step 2
PHASES_2_USE_ST2  a
WIN_START_A_ST2   0.05
WIN_TAPER_A_ST2   0.01

# Number of iterative loops for step 2
LOOPS_LOC_CONF    1
REDUCE_LOC_CONF   3

# Plot parameters for inversion step2
DATA_PLOT_STEP2   seis
FILT_PLOT_STEP2   plain
START_PLOT_STEP2 0
LEN_PLOT_STEP2    2
```

```
TICK_PLOT_STEP2  1
AMPL_PLOT_STEP2  norm
```

A.3 VOLPIS

This is the input file to perform the MT inversion using VOLPIS.

```
'retard.dat'
1024, 0.1, 0.5, 10, 0, 2, 1
1, 1, 99999, 99999
2, 1
0, 0, 0
```

Where retard.dat contains information about the stations and length of the time series. 1024 is the number of samples for each time series, 0.1 the low cut-off frequency, 0.5 is the high cut-off frequency. The rest are default values.

The following is an example of the retard.dat file.

```
./
Z   1  S01   P   5.800    10    10   10.000    0.000 999  1.000
N   1  S01   S   5.800    10    10   10.000    0.000 999  1.000
E   1  S01   S   5.800    10    10   10.000    0.000 999  1.000
Z   2  S02   P   5.800    10    10   10.000   30.000 999  1.000
N   2  S02   S   5.800    10    10   10.000   30.000 999  1.000
E   2  S02   S   5.800    10    10   10.000   30.000 999  1.000
Z   3  S03   P   5.800    10    10   10.000   60.000 999  1.000
N   3  S03   S   5.800    10    10   10.000   60.000 999  1.000
E   3  S03   S   5.800    10    10   10.000   60.000 999  1.000
Z   4  S04   P   5.800    10    10   10.000   90.000 999  1.000
N   4  S04   S   5.800    10    10   10.000   90.000 999  1.000
E   4  S04   S   5.800    10    10   10.000   90.000 999  1.000
Z   5  S05   P   5.800    10    10   10.000  120.000 999  1.000
N   5  S05   S   5.800    10    10   10.000  120.000 999  1.000
E   5  S05   S   5.800    10    10   10.000  120.000 999  1.000
Z   6  S06   P   5.800    10    10   10.000  150.000 999  1.000
```

```
N   6  S06   S   5.800    10    10   10.000  150.000 999  1.000
E   6  S06   S   5.800    10    10   10.000  150.000 999  1.000
Z   7  S07   P   5.800    10    10   10.000  180.000 999  1.000
N   7  S07   S   5.800    10    10   10.000  180.000 999  1.000
E   7  S07   S   5.800    10    10   10.000  180.000 999  1.000
Z   8  S08   P   5.800    10    10   10.000  210.000 999  1.000
N   8  S08   S   5.800    10    10   10.000  210.000 999  1.000
E   8  S08   S   5.800    10    10   10.000  210.000 999  1.000
Z   9  S09   P   5.800    10    10   10.000  240.000 999  1.000
N   9  S09   S   5.800    10    10   10.000  240.000 999  1.000
E   9  S09   S   5.800    10    10   10.000  240.000 999  1.000
Z  10  S10   P   5.800    10    10   10.000  270.000 999  1.000
N  10  S10   S   5.800    10    10   10.000  270.000 999  1.000
E  10  S10   S   5.800    10    10   10.000  270.000 999  1.000
Z  11  S11   P   5.800    10    10   10.000  300.000 999  1.000
N  11  S11   S   5.800    10    10   10.000  300.000 999  1.000
E  11  S11   S   5.800    10    10   10.000  300.000 999  1.000
Z  12  S12   P   5.800    10    10   10.000  330.000 999  1.000
N  12  S12   S   5.800    10    10   10.000  330.000 999  1.000
E  12  S12   S   5.800    10    10   10.000  330.000 999  1.000
Z  13  S13   P   5.800    10    10   10.000    0.000 999  1.000
N  13  S13   S   5.800    10    10   10.000    0.000 999  1.000
E  13  S13   S   5.800    10    10   10.000    0.000 999  1.000
Z  14  S14   P   5.800    10    10   10.000   30.000 999  1.000
N  14  S14   S   5.800    10    10   10.000   30.000 999  1.000
E  14  S14   S   5.800    10    10   10.000   30.000 999  1.000
Z  15  S15   P   5.800    10    10   10.000   60.000 999  1.000
N  15  S15   S   5.800    10    10   10.000   60.000 999  1.000
E  15  S15   S   5.800    10    10   10.000   60.000 999  1.000
Z  16  S16   P   5.800    10    10   10.000   90.000 999  1.000
N  16  S16   S   5.800    10    10   10.000   90.000 999  1.000
E  16  S16   S   5.800    10    10   10.000   90.000 999  1.000
Z  17  S17   P   5.800    10    10   10.000  120.000 999  1.000
N  17  S17   S   5.800    10    10   10.000  120.000 999  1.000
```

```
E  17  S17   S   5.800    10    10   10.000  120.000 999  1.000
Z  18  S18   P   5.800    10    10   10.000  150.000 999  1.000
N  18  S18   S   5.800    10    10   10.000  150.000 999  1.000
E  18  S18   S   5.800    10    10   10.000  150.000 999  1.000
Z  19  S19   P   5.800    10    10   10.000  180.000 999  1.000
N  19  S19   S   5.800    10    10   10.000  180.000 999  1.000
E  19  S19   S   5.800    10    10   10.000  180.000 999  1.000
Z  20  S20   P   5.800    10    10   10.000  210.000 999  1.000
N  20  S20   S   5.800    10    10   10.000  210.000 999  1.000
E  20  S20   S   5.800    10    10   10.000  210.000 999  1.000
Z  21  S21   P   5.800    10    10   10.000  240.000 999  1.000
N  21  S21   S   5.800    10    10   10.000  240.000 999  1.000
E  21  S21   S   5.800    10    10   10.000  240.000 999  1.000
Z  22  S22   P   5.800    10    10   10.000  270.000 999  1.000
N  22  S22   S   5.800    10    10   10.000  270.000 999  1.000
E  22  S22   S   5.800    10    10   10.000  270.000 999  1.000
Z  23  S23   P   5.800    10    10   10.000  300.000 999  1.000
N  23  S23   S   5.800    10    10   10.000  300.000 999  1.000
E  23  S23   S   5.800    10    10   10.000  300.000 999  1.000
Z  24  S24   P   5.800    10    10   10.000  330.000 999  1.000
N  24  S24   S   5.800    10    10   10.000  330.000 999  1.000
E  24  S24   S   5.800    10    10   10.000  330.000 999  1.000
Z  25  S25   P   5.800    10    10   10.000    0.000 999  1.000
N  25  S25   S   5.800    10    10   10.000    0.000 999  1.000
E  25  S25   S   5.800    10    10   10.000    0.000 999  1.000
Z  26  S26   P   5.800    10    10   10.000   30.000 999  1.000
N  26  S26   S   5.800    10    10   10.000   30.000 999  1.000
E  26  S26   S   5.800    10    10   10.000   30.000 999  1.000
Z  27  S27   P   5.800    10    10   10.000   60.000 999  1.000
N  27  S27   S   5.800    10    10   10.000   60.000 999  1.000
E  27  S27   S   5.800    10    10   10.000   60.000 999  1.000
Z  28  S28   P   5.800    10    10   10.000   90.000 999  1.000
N  28  S28   S   5.800    10    10   10.000   90.000 999  1.000
E  28  S28   S   5.800    10    10   10.000   90.000 999  1.000
```

```
Z  29  S29   P   5.800    10    10    10.000  120.000 999  1.000
N  29  S29   S   5.800    10    10    10.000  120.000 999  1.000
E  29  S29   S   5.800    10    10    10.000  120.000 999  1.000
Z  30  S30   P   5.800    10    10    10.000  150.000 999  1.000
N  30  S30   S   5.800    10    10    10.000  150.000 999  1.000
E  30  S30   S   5.800    10    10    10.000  150.000 999  1.000
Z  31  S31   P   5.800    10    10    10.000  180.000 999  1.000
N  31  S31   S   5.800    10    10    10.000  180.000 999  1.000
E  31  S31   S   5.800    10    10    10.000  180.000 999  1.000
Z  32  S32   P   5.800    10    10    10.000  210.000 999  1.000
N  32  S32   S   5.800    10    10    10.000  210.000 999  1.000
E  32  S32   S   5.800    10    10    10.000  210.000 999  1.000
Z  33  S33   P   5.800    10    10    10.000  240.000 999  1.000
N  33  S33   S   5.800    10    10    10.000  240.000 999  1.000
E  33  S33   S   5.800    10    10    10.000  240.000 999  1.000
Z  34  S34   P   5.800    10    10    10.000  270.000 999  1.000
N  34  S34   S   5.800    10    10    10.000  270.000 999  1.000
E  34  S34   S   5.800    10    10    10.000  270.000 999  1.000
Z  35  S35   P   5.800    10    10    10.000  300.000 999  1.000
N  35  S35   S   5.800    10    10    10.000  300.000 999  1.000
E  35  S35   S   5.800    10    10    10.000  300.000 999  1.000
Z  36  S36   P   5.800    10    10    10.000  330.000 999  1.000
N  36  S36   S   5.800    10    10    10.000  330.000 999  1.000
E  36  S36   S   5.800    10    10    10.000  330.000 999  1.000
```

A.4 Specfem3D

Here we show the most important input files needed to create synthetic seismograms using Specfem3D. First, the $Mesh_Par_file$, which contains information about the mesh for the especific case of Bardarbunga.

```
 #-------------------------------------------------------------
#
# Meshing input parameters
```

```
#
#-----------------------------------------------------------

# coordinates of mesh block in latitude/longitude and depth in km
LATITUDE_MIN                    = 0.0d0
LATITUDE_MAX                    = 448000.0d0
LONGITUDE_MIN                   = 0.0d0
LONGITUDE_MAX                   = 448000.0d0
DEPTH_BLOCK_KM                  = 36.d0
UTM_PROJECTION_ZONE             = 11
SUPPRESS_UTM_PROJECTION         = .true.

# file that contains the interfaces of the model / mesh
INTERFACES_FILE                 = interfaces.dat

# file that contains the cavity
CAVITY_FILE                     = no_cavity.dat

# number of elements at the surface along edges of the mesh at the surface
# (must be 8 * multiple of NPROC below if mesh is not regular and contains
mesh doublings)
# (must be multiple of NPROC below if mesh is regular)
NEX_XI                          = 128
NEX_ETA                         = 128

# number of MPI processors along xi and eta (can be different)
NPROC_XI                        = 4
NPROC_ETA                       = 4

#-----------------------------------------------------------
#
# Doubling layers
#
#-----------------------------------------------------------
```

```
# Regular/irregular mesh
USE_REGULAR_MESH                = .true.
# Only for irregular meshes, number of doubling layers and their position
NDOUBLINGS                      = 0
# NZ_DOUBLING_1 is the parameter to set up if there is only one doubling
layer
# (more doubling entries can be added if needed to match NDOUBLINGS value)
NZ_DOUBLING_1                   = 11
NZ_DOUBLING_2                   = 0

#-----------------------------------------------------------
#
# Visualization
#
#-----------------------------------------------------------

# create mesh files for visualisation or further checking
CREATE_ABAQUS_FILES             = .false.
CREATE_DX_FILES                 = .false.
CREATE_VTK_FILES                = .false.

# path to store the databases files
LOCAL_PATH                      = DATABASES_MPI

#-----------------------------------------------------------
#
# CPML
#
#-----------------------------------------------------------

# CPML perfectly matched absorbing layers
THICKNESS_OF_X_PML              = 0.0d0
THICKNESS_OF_Y_PML              = 0.0d0
```

```
THICKNESS_OF_Z_PML              = 0.0d0

#-----------------------------------------------------------
#
# Domain materials
#
#-----------------------------------------------------------

# number of materials
NMATERIALS                      = 1
# define the different materials in the model as:
# #material_id  #rho  #vp  #vs  #Q_Kappa  #Q_mu  #anisotropy_flag  #domain_id
#     Q_Kappa          : Q_Kappa attenuation quality factor
#     Q_mu             : Q_mu attenuation quality factor
#     anisotropy_flag  : 0 = no anisotropy / 1,2,... check the implementation
in file aniso_model.f90
#     domain_id        : 1 = acoustic / 2 = elastic
1  1600.  4500.  2600.  1000. 1000.0  0  2
#2  1100  1600  0    9999. 50.0  0  1
#3  1000  1500  700  9999. 9999. 0  2
#4  1300  1400  700  9999. 50.0  0  2

#-----------------------------------------------------------
#
# Domain regions
#
#-----------------------------------------------------------

# number of regions
NREGIONS                        = 1
# define the different regions of the model as :
#NEX_XI_BEGIN  #NEX_XI_END  #NEX_ETA_BEGIN  #NEX_ETA_END  #NZ_BEGIN #NZ_END
 #material_id
1              128           1               128           1
```

```
 30        1
#1               64              1               64              5
  5        2
#1               64              1               64              6
  15       3
#17              64              7               25              7
  10       4
```

This is an example of a STATIONS file, describing the geometry of the seismic network.

```
ADA IC 212170.81 349231.58 0.0 0.0
ALF IC 26954.301 190003.57 0.0 0.0
ASB IC 162475.67 79754.836 0.0 0.0
ASK IC 210333.89 298578.50 0.0 0.0
ASM IC 61718.565 117368.88 0.0 0.0
AUS IC 47411.987 193890.21 0.0 0.0
BJA IC 73118.064 83189.085 0.0 0.0
BJK IC 145093.52 300111.54 0.0 0.0
BRE IC 324070.97 229747.92 0.0 0.0
DIM IC 310115.02 275500.99 0.0 0.0
DJK IC 146783.85 276576.05 0.0 0.0
DYN IC 178123.06 267513.54 0.0 0.0
ENT IC 50337.974 188706.28 0.0 0.0
ESK IC 29975.286 176513.37 0.0 0.0
FAG IC 79592.369 311399.14 0.0 0.0
FED IC 85016.626 161700.75 0.0 0.0
FLA IC 328525.58 232191.92 0.0 0.0
GFL IC 31072.089 193446.64 0.0 0.0
GHA IC 298107.10 289011.87 0.0 0.0
GIL IC 325553.90 300427.07 0.0 0.0
GOD IC 45367.475 182057.40 0.0 0.0
GRA IC 302533.14 246626.81 0.0 0.0
GRF IC 135869.03 276068.19 0.0 0.0
```

```
GRI IC 370312.06 221519.25 0.0 0.0
GRS IC 277943.39 315997.63 0.0 0.0
GRV IC 62203.811 26754.986 0.0 0.0
GYG IC 112310.55 134864.08 0.0 0.0
HAE IC 94776.943 293425.28 0.0 0.0
HAU IC 78112.812 148618.94 0.0 0.0
HED IC 321732.40 257184.52 0.0 0.0
HEI IC 101514.70 85688.708 0.0 0.0
HES IC 87805.375 167963.87 0.0 0.0
HLA IC 302486.93 209726.12 0.0 0.0
HRN IC 316269.78 130023.28 0.0 0.0
HUS IC 121890.68 258373.58 0.0 0.0
HVE IC 179436.10 162663.47 0.0 0.0
HVO IC 31890.545 206457.99 0.0 0.0
IEY IC 97718.483 237552.98 0.0 0.0
JOK IC 121818.76 230802.31 0.0 0.0
KAL IC 83077.159 260160.97 0.0 0.0
KAS IC 81100.534 56125.455 0.0 0.0
KRE IC 181859.57 314112.49 0.0 0.0
KRI IC 64759.554 45409.200 0.0 0.0
KRO IC 90308.784 91657.724 0.0 0.0
KSK IC 112238.70 316939.94 0.0 0.0
KUD IC 114297.87 54413.986 0.0 0.0
KVE IC 168656.70 301334.45 0.0 0.0
KVO IC 282791.14 280501.22 0.0 0.0
LEI IC 361533.35 290346.77 0.0 0.0
LOD IC 55224.107 207762.76 0.0 0.0
MEL IC 267817.34 292353.06 0.0 0.0
MID IC 43661.704 154174.90 0.0 0.0
MJO IC 74819.623 163163.58 0.0 0.0
MKO IC 203619.52 313966.06 0.0 0.0
MOK IC 203614.56 313919.11 0.0 0.0
NYL IC 75158.975 12832.226 0.0 0.0
REN IC 275236.94 280082.21 0.0 0.0
```

```
RJU IC 42596.709 214510.60 0.0 0.0
RNE IC 57664.095 14480.156 0.0 0.0
SAN IC 85057.463 69827.737 0.0 0.0
SAU IC 79481.252 126501.40 0.0 0.0
SIG IC 321750.98 184391.93 0.0 0.0
SKI IC 299479.56 272176.39 0.0 0.0
SKR IC 148502.45 221050.87 0.0 0.0
SLY IC 64223.746 191081.78 0.0 0.0
SNB IC 55976.814 215633.28 0.0 0.0
SOL IC 71741.486 100843.24 0.0 0.0
SVA IC 239275.60 267239.08 0.0 0.0
THO IC 197097.09 298581.51 0.0 0.0
URH IC 182288.61 277584.39 0.0 0.0
VAT IC 105238.07 198271.08 0.0 0.0
VME IC 17009.697 135076.28 0.0 0.0
VOG IC 74828.224 29733.503 0.0 0.0
VON IC 163411.68 250127.68 0.0 0.0
VOS IC 62291.074 63745.265 0.0 0.0
VOT IC 121123.75 281488.37 0.0 0.0
VSH IC 187930.49 344768.20 0.0 0.0
```

Here we show an example of CMTSOLUTION (Sources modelled) used to create the synthetics with the geometry of Bardarbunga for a half-ring propagating rupture.

```
PDE  1999 01 01 00 00 00.00  67000 67000 -25000 2.2 2.2 hom_explosion
event name:       hom_explosion
time shift:       0.0000
half duration:    20
latorUTM:       164162.4
longorUTM:      261293.7
depth:           5.0
Mrr:       -3.464101615137755e+20
Mtt:       3.464101615137755e+20
Mpp:       0.0
```

```
Mrt:       -1.9999999999999993e+20
Mrp:       0.0
Mtp:       0.0
./DATA/GF/gf40s-iceland.txt
PDE  1999 01 01 00 00 00.00  67000 67000 -25000 2.2 2.2 hom_explosion
event name:       hom_explosion
time shift:       1.0000
half duration:    20
latorUTM:       164109.227136
longorUTM:      261901.468622
depth:           5.0
Mrr:       -3.464101615137755e+20
Mtt:       3.3596461702676244e+20
Mpp:       1.0445544487012993e+19
Mrt:       -1.9696155060244152e+20
Mrp:       3.4729635533386076e+19
Mtp:       -5.923962654520477e+19
./DATA/GF/gf40s-iceland.txt
PDE  1999 01 01 00 00 00.00  67000 67000 -25000 2.2 2.2 hom_explosion
event name:       hom_explosion
time shift:       2.0000
half duration:    20
latorUTM:       163951.324173
longorUTM:      262490.770502
depth:           5.0
Mrr:       -3.464101615137755e+20
Mtt:       3.058878703906754e+20
Mpp:       4.0522291123100066e+19
Mrt:       -1.879385241571816e+20
Mrp:       6.8404028665133744e+19
Mtp:       -1.1133407984528389e+20
./DATA/GF/gf40s-iceland.txt
PDE  1999 01 01 00 00 00.00  67000 67000 -25000 2.2 2.2 hom_explosion
event name:       hom_explosion
```

```
time shift:       3.0000
half duration:    20
latorUTM:       163693.488913
longorUTM:      263043.7
depth:           5.0
Mrr:       -3.464101615137755e+20
Mtt:       2.5980762113533156e+20
Mpp:       8.660254037844387e+19
Mrt:       -1.7320508075688765e+20
Mrp:       9.999999999999998e+19
Mtp:       -1.5000000000000003e+20
./DATA/GF/gf40s-iceland.txt
PDE  1999 01 01 00 00 00.00  67000 67000 -25000 2.2 2.2 hom_explosion
event name:       hom_explosion
time shift:       4.0000
half duration:    20
latorUTM:       163343.555551
longorUTM:      263543.456634
depth:           5.0
Mrr:       -3.464101615137755e+20
Mtt:       2.032818273929748e+20
Mpp:       1.4312833412080067e+20
Mrt:       -1.5320888862379554e+20
Mrp:       1.2855752193730781e+20
Mtp:       -1.7057370639048865e+20
./DATA/GF/gf40s-iceland.txt
PDE  1999 01 01 00 00 00.00  67000 67000 -25000 2.2 2.2 hom_explosion
event name:       hom_explosion
time shift:       5.0000
half duration:    20
latorUTM:       162912.156634
longorUTM:      263974.855551
depth:           5.0
Mrr:       -3.464101615137755e+20
```

```
Mtt:       1.4312833412080068e+20
Mpp:       2.032818273929748e+20
Mrt:       -1.2855752193730778e+20
Mrp:       1.5320888862379554e+20
Mtp:       -1.7057370639048865e+20
./DATA/GF/gf40s-iceland.txt
PDE  1999 01 01 00 00 00.00  67000 67000 -25000 2.2 2.2 hom_explosion
event name:       hom_explosion
time shift:       6.0000
half duration:    20
latorUTM:       162412.4
longorUTM:      264324.788913
depth:           5.0
Mrr:       -3.464101615137755e+20
Mtt:       8.660254037844387e+19
Mpp:       2.5980762113533166e+20
Mrt:       -9.999999999999995e+19
Mrp:       1.7320508075688768e+20
Mtp:       -1.5e+20
./DATA/GF/gf40s-iceland.txt
PDE  1999 01 01 00 00 00.00  67000 67000 -25000 2.2 2.2 hom_explosion
event name:       hom_explosion
time shift:       7.0000
half duration:    20
latorUTM:       161859.470502
longorUTM:      264582.624173
depth:           5.0
Mrr:       -3.464101615137755e+20
Mtt:       4.052229112310006e+19
Mpp:       3.0588787039067544e+20
Mrt:       -6.840402866513371e+19
Mrp:       1.879385241571816e+20
Mtp:       -1.1133407984528389e+20
./DATA/GF/gf40s-iceland.txt
```

```
PDE  1999 01 01 00 00 00.00  67000 67000 -25000 2.2 2.2 hom_explosion
event name:       hom_explosion
time shift:       8.0000
half duration:    20
latorUTM:       161270.168622
longorUTM:      264740.527136
depth:           5.0
Mrr:       -3.464101615137755e+20
Mtt:       1.0445544487012997e+19
Mpp:       3.3596461702676244e+20
Mrt:       -3.472963553338605e+19
Mrp:       1.9696155060244152e+20
Mtp:       -5.923962654520479e+19
./DATA/GF/gf40s-iceland.txt
PDE  1999 01 01 00 00 00.00  67000 67000 -25000 2.2 2.2 hom_explosion
event name:       hom_explosion
time shift:       9.0000
half duration:    20
latorUTM:       160662.4
longorUTM:      264793.7
depth:           5.0
Mrr:       -3.464101615137755e+20
Mtt:       0.0
Mpp:       3.464101615137755e+20
Mrt:       0.0
Mrp:       1.999999999999999e+20
Mtp:       0.0
./DATA/GF/gf40s-iceland.txt
PDE  1999 01 01 00 00 00.00  67000 67000 -25000 2.2 2.2 hom_explosion
event name:       hom_explosion
time shift:       10.0000
half duration:    20
latorUTM:       160054.631378
longorUTM:      264740.527136
```

```
depth:           5.0
Mrr:       -3.464101615137755e+20
Mtt:       1.0445544487012983e+19
Mpp:       3.3596461702676244e+20
Mrt:       3.472963553338605e+19
Mrp:       1.9696155060244152e+20
Mtp:       5.923962654520475e+19
./DATA/GF/gf40s-iceland.txt
PDE  1999 01 01 00 00 00.00  67000 67000 -25000 2.2 2.2 hom_explosion
event name:       hom_explosion
time shift:       11.0000
half duration:    20
latorUTM:       159465.329498
longorUTM:      264582.624173
depth:           5.0
Mrr:       -3.464101615137755e+20
Mtt:       4.052229112310003e+19
Mpp:       3.0588787039067544e+20
Mrt:       6.840402866513371e+19
Mrp:       1.879385241571816e+20
Mtp:       1.1133407984528386e+20
./DATA/GF/gf40s-iceland.txt
PDE  1999 01 01 00 00 00.00  67000 67000 -25000 2.2 2.2 hom_explosion
event name:       hom_explosion
time shift:       12.0000
half duration:    20
latorUTM:       158912.4
longorUTM:      264324.788913
depth:           5.0
Mrr:       -3.464101615137755e+20
Mtt:       8.660254037844383e+19
Mpp:       2.5980762113533166e+20
Mrt:       9.999999999999995e+19
Mrp:       1.7320508075688768e+20
```

```
Mtp:       1.5e+20
./DATA/GF/gf40s-iceland.txt
PDE  1999 01 01 00 00 00.00  67000 67000 -25000 2.2 2.2 hom_explosion
event name:       hom_explosion
time shift:       13.0000
half duration:    20
latorUTM:       158412.643366
longorUTM:      263974.855551
depth:           5.0
Mrr:       -3.464101615137755e+20
Mtt:       1.4312833412080063e+20
Mpp:       2.032818273929748e+20
Mrt:       1.2855752193730778e+20
Mrp:       1.5320888862379554e+20
Mtp:       1.7057370639048865e+20
./DATA/GF/gf40s-iceland.txt
PDE  1999 01 01 00 00 00.00  67000 67000 -25000 2.2 2.2 hom_explosion
event name:       hom_explosion
time shift:       14.0000
half duration:    20
latorUTM:       157981.244449
longorUTM:      263543.456634
depth:           5.0
Mrr:       -3.464101615137755e+20
Mtt:       2.032818273929748e+20
Mpp:       1.431283341208007e+20
Mrt:       1.5320888862379554e+20
Mrp:       1.2855752193730781e+20
Mtp:       1.7057370639048865e+20
./DATA/GF/gf40s-iceland.txt
PDE  1999 01 01 00 00 00.00  67000 67000 -25000 2.2 2.2 hom_explosion
event name:       hom_explosion
time shift:       15.0000
half duration:    20
```

```
latorUTM:       157631.311087
longorUTM:      263043.7
depth:           5.0
Mrr:       -3.464101615137755e+20
Mtt:       2.5980762113533156e+20
Mpp:       8.660254037844392e+19
Mrt:       1.7320508075688765e+20
Mrp:       9.999999999999997e+19
Mtp:       1.5000000000000003e+20
./DATA/GF/gf40s-iceland.txt
PDE  1999 01 01 00 00 00.00  67000 67000 -25000 2.2 2.2 hom_explosion
event name:       hom_explosi0.1on
time shift:       16.0000
half duration:    20
latorUTM:       157373.475827
longorUTM:      262490.770502
depth:           5.0
Mrr:       -3.464101615137755e+20
Mtt:       3.058878703906754e+20
Mpp:       4.052229112310008e+19
Mrt:       1.879385241571816e+20
Mrp:       6.840402866513372e+19
Mtp:       1.1133407984528394e+20
./DATA/GF/gf40s-iceland.txt
PDE  1999 01 01 00 00 00.00  67000 67000 -25000 2.2 2.2 hom_explosion
event name:       hom_explosion
time shift:       17.0000
half duration:    20
latorUTM:       157215.572864
longorUTM:      261901.468622
depth:           5.0
Mrr:       -3.464101615137755e+20
Mtt:       3.3596461702676244e+20
Mpp:       1.0445544487013005e+19
```

```
Mrt:       1.9696155060244152e+20
Mrp:       3.4729635533386056e+19
Mtp:       5.923962654520481e+19
./DATA/GF/gf40s-iceland.txt
PDE  1999 01 01 00 00 00.00  67000 67000 -25000 2.2 2.2 hom_explosion
event name:       hom_explosion
time shift:       18.0000
half duration:    20
latorUTM:       157162.4
longorUTM:      261293.7
depth:           5.0
Mrr:       -3.464101615137755e+20
Mtt:       3.464101615137755e+20
Mpp:       0.0
Mrt:       1.9999999999999993e+20
Mrp:       0.0
Mtp:       0.0
./DATA/GF/gf40s-iceland.txt
```

Here we show an example of Par_file used to create the synthetics with the geometry of Bardarbunga.

```
#-------------------------------------------------------------
#
# Simulation input parameters
#
#-------------------------------------------------------------

# forward or adjoint simulation
# 1 = forward, 2 = adjoint, 3 = both simultaneously
SIMULATION_TYPE                 = 1
# 0 = earthquake simulation,  1/2/3 = three steps in noise simulation
NOISE_TOMOGRAPHY                = 0
SAVE_FORWARD                    = .false.
```

```
INVERSE_FWI_FULL_PROBLEM        = .false.

# UTM projection parameters
# Use a negative zone number for the Southern hemisphere:
# The Northern hemisphere corresponds to zones +1 to +60,
# The Southern hemisphere corresponds to zones -1 to -60.
UTM_PROJECTION_ZONE             = 11
SUPPRESS_UTM_PROJECTION         = .true.

# number of MPI processors
NPROC                           = 16

# time step parameters
NSTEP                           = 12000
DT                              = 0.05

#-----------------------------------------------------------
#
# LDDRK time scheme
#
#-----------------------------------------------------------
USE_LDDRK                       = .false.
INCREASE_CFL_FOR_LDDRK          = .false.
RATIO_BY_WHICH_TO_INCREASE_IT   = 1.4

#-----------------------------------------------------------
#
# Mesh
#
#-----------------------------------------------------------

# Number of nodes for 2D and 3D shape functions for hexahedra.
# We use either 8-node mesh elements (bricks) or 27-node elements.
```

```
NGNOD                           = 8

# models:
# available options are:
#   default (model parameters described by mesh properties)
# 1D models available are:
#   1d_prem,1d_socal,1d_cascadia
# 3D models available are:
#   aniso,external,gll,salton_trough,tomo,SEP,coupled,...
MODEL                           = default

# path for external tomographic models files
TOMOGRAPHY_PATH                 = ./DATA/tomo_files/
# if you are using a SEP model (oil-industry format)
SEP_MODEL_DIRECTORY             = ./DATA/my_SEP_model/

#-----------------------------------------------------------

# parameters describing the model
APPROXIMATE_OCEAN_LOAD          = .false.
TOPOGRAPHY                      = .false.
ATTENUATION                     = .false.
ANISOTROPY                      = .false.
GRAVITY                         = .false.


ATTENUATION_f0_REFERENCE        = 0.33333d0

# attenuation period constant Q factor
MIN_ATTENUATION_PERIOD          = 999999998.d0
MAX_ATTENUATION_PERIOD          = 999999999.d0

COMPUTE_FREQ_BAND_AUTOMATIC     = .true.
```

```
# Olsen's constant for Q_mu = constant * V_s attenuation rule
USE_OLSEN_ATTENUATION           = .false.
OLSEN_ATTENUATION_RATIO         = 0.05

#-----------------------------------------------------------
#
# Absorbing boundary conditions
#
#-----------------------------------------------------------

# C-PML boundary conditions for a regional simulation

PML_CONDITIONS                  = .false.

# C-PML top surface
PML_INSTEAD_OF_FREE_SURFACE     = .false.

# C-PML dominant frequency
f0_FOR_PML                      = 0.333333d0

# parameters used to rotate C-PML boundary conditions
# ROTATE_PML_ACTIVATE           = .false.
# ROTATE_PML_ANGLE              = 0.


STACEY_ABSORBING_CONDITIONS     = .true.

# absorbing top surface (defined in mesh as 'free_surface_file')
STACEY_INSTEAD_OF_FREE_SURFACE  = .false.

# When STACEY_ABSORBING_CONDITIONS is set to .true. :
# absorbing conditions are defined in xmin, xmax, ymin, ymax and zmin
# this option BOTTOM_FREE_SURFACE can be set to .true. to
```

```
# make zmin free surface instead of absorbing condition
BOTTOM_FREE_SURFACE             = .false.

#-----------------------------------------------------------
#
# undoing attenuation and/or PMLs for sensitivity kernel calculations
#
#-----------------------------------------------------------


UNDO_ATTENUATION_AND_OR_PML     = .false.
NT_DUMP_ATTENUATION             = 500

#-----------------------------------------------------------
#
# Visualization
#
#-----------------------------------------------------------

# save AVS or OpenDX movies
# MOVIE_TYPE = 1 to show the top surface
# MOVIE_TYPE = 2 to show all the external faces of the mesh
CREATE_SHAKEMAP                 = .false.
MOVIE_SURFACE                   = .false.
MOVIE_TYPE                      = 1
MOVIE_VOLUME                    = .false.
SAVE_DISPLACEMENT               = .false.
USE_HIGHRES_FOR_MOVIES          = .false.
NTSTEP_BETWEEN_FRAMES           = 200
HDUR_MOVIE                      = 0.0

# save AVS or OpenDX mesh files to check the mesh
SAVE_MESH_FILES                 = .true.
```

```
# path to store the local database file on each node
LOCAL_PATH                      = DATABASES_MPI

# interval at which we output time step info
NTSTEP_BETWEEN_OUTPUT_INFO      = 10000

#-----------------------------------------------------------
#
# Sources
#
#-----------------------------------------------------------


USE_SOURCES_RECEIVERS_Z         = .false.

# use a (tilted) FORCESOLUTION force point source (or several)

USE_FORCE_POINT_SOURCE          = .false.


USE_RICKER_TIME_FUNCTION        = .false.

# Use an external source time function.

USE_EXTERNAL_SOURCE_FILE        = .true.

# print source time function
PRINT_SOURCE_TIME_FUNCTION      = .false.

#-----------------------------------------------------------
#
# Seismograms
#
#-----------------------------------------------------------
```

```
# interval in time steps for writing of seismograms
NTSTEP_BETWEEN_OUTPUT_SEISMOS   = 10000

AVE_SEISMOGRAMS_DISPLACEMENT   = .true.
SAVE_SEISMOGRAMS_VELOCITY       = .false.
SAVE_SEISMOGRAMS_ACCELERATION   = .false.
SAVE_SEISMOGRAMS_PRESSURE       = .false.

# save seismograms also when running the adjoint runs for an inverse
problem
# (usually they are unused and not very meaningful, leave this off in
almost all cases)
SAVE_SEISMOGRAMS_IN_ADJOINT_RUN = .false.

USE_BINARY_FOR_SEISMOGRAMS      = .false.

# output seismograms in Seismic Unix format
SU_FORMAT                       = .false.

# output seismograms in ASDF (requires asdf-library)
ASDF_FORMAT                     = .false.

WRITE_SEISMOGRAMS_BY_MASTER     = .false.

# save all seismograms in one large combined file instead of one file
per seismogram
# to avoid overloading shared non-local file systems such as LUSTRE or
GPFS for instance
SAVE_ALL_SEISMOS_IN_ONE_FILE    = .false.


USE_TRICK_FOR_BETTER_PRESSURE   = .false.
```

```
#-----------------------------------------------------------
#
# Source encoding
#
#-----------------------------------------------------------


USE_SOURCE_ENCODING             = .false.

#-----------------------------------------------------------
#
# Energy calculation
#
#-----------------------------------------------------------

# to plot energy curves, for instance to monitor how CPML absorbing layers
#behave; should be turned OFF in most cases because a bit expensive
OUTPUT_ENERGY                   = .false.
# every how many time steps we compute energy
NTSTEP_BETWEEN_OUTPUT_ENERGY    = 10

#-----------------------------------------------------------
#
# Adjoint kernel outputs
#
#-----------------------------------------------------------

# interval in time steps for reading adjoint traces
# 0 = read the whole adjoint sources at the same time
NTSTEP_BETWEEN_READ_ADJSRC      = 0

# read adjoint sources using ASDF (requires asdf-library)
READ_ADJSRC_ASDF                = .false.
```

```
# set to .true. to compute anisotropic kernels
# default is .false. to compute isotropic kernels
ANISOTROPIC_KL                  = .false.

# compute transverse isotropic kernels
#(alpha_v,alpha_h,beta_v,beta_h,eta,rho)
# rather than fully anisotropic kernels
#in case ANISOTROPIC_KL is set to .true.
SAVE_TRANSVERSE_KL              = .false.

# this parameter must be set to .true. to compute anisotropic
#kernels for cost function using velocity observable rather
#than displacement
ANISOTROPIC_VELOCITY_KL         = .false.

# outputs approximate Hessian for preconditioning
APPROXIMATE_HESS_KL             = .false.

# save Moho mesh and compute Moho boundary kernels
SAVE_MOHO_MESH                  = .false.

#-------------------------------------------------------------
#
# Coupling with an injection technique (DSM, AxiSEM, or FK)
#
#-------------------------------------------------------------
COUPLE_WITH_INJECTION_TECHNIQUE = .false.
INJECTION_TECHNIQUE_TYPE        = 3   # 1 = DSM, 2 = AxiSEM, 3 = FK
MESH_A_CHUNK_OF_THE_EARTH       = .false.
TRACTION_PATH                   = ./DATA/AxiSEM_tractions/3/
FKMODEL_FILE                    = FKmodel
RECIPROCITY_AND_KH_INTEGRAL     = .false.   # does not work yet

ASDF_FORMAT                     = .false.
```

```
READ_ADJSRC_ASDF                = .false.
#-----------------------------------------------------------


NUMBER_OF_SIMULTANEOUS_RUNS     = 1


BROADCAST_SAME_MESH_AND_MODEL   = .false.

#-----------------------------------------------------------

# set to true to use GPUs
GPU_MODE                        = .false.

# ADIOS Options for I/Os
ADIOS_ENABLED                   = .false.
ADIOS_FOR_DATABASES             = .false.
ADIOS_FOR_MESH                  = .false.
ADIOS_FOR_FORWARD_ARRAYS        = .false.
ADIOS_FOR_KERNELS               = .false.
```

Appendix B

Codes developed

In this thesis, I used forward modelling and moment tensor inversion packages to obtain main results. However, I produced codes for pre-processing, processing and analyse the data, in the following.

B.1 Ring radiation pattern - MATLAB

```
 % Documentation
% This matlab script calculates the radiation pattern produced by a
% cylindrical fault, or part of a cylinder, rupturing along the axial
% direction. It considers a summation of plane fault contributions
% It shows a video on how the summation evolves with different angles
% Result is T

clear;
th = -90:1:90;                          %  Elevation
ph = 0:1:360;                           %  Azimuth
d = 40;                                 %  Defintions d = diameter of the
cylinder [m]
r = 1000;                              %  Distance of observation in far
field [m]
R = d/2 ;                               %  Radius, half of the diameter [m]
step=1;                                 %  Distance in angles between two
```

```
adjacent planes [degrees]
n=180;                                  %  Number of plane faults considered
[phi,theta]=meshgrid(ph,th);            %  Grid using the angles previously
defined
p = r * cosd(theta);                    %  Projection of r in the XY plane
q = R./p;                               %  Ratio between radius and distance
of observation

%  Variations of theta and phi due to "a".
theta1 = atan2d(r *sind(theta),(sqrt(R^2 + p.^2 - 2*R*p.*...
cosd(180-phi))));
phi1 =   atan2d(sind(phi),(cosd(phi)+q));
theta2 = atan2d(r *sind(theta),(sqrt(R^2 + p.^2 - 2*R*p.*...
cosd(phi))));
phi2 =   atan2d(sind(phi),(cosd(phi)-q));

%  Calculations of Amplitudes for each DC and then summation
%  a*(pi/180)*step corresponds to normalization by area
A1 = R*(pi/180)*step*sind(2*theta1) .* cosd(phi1);
A2 = 0;%-R*(pi/180)*step*sind(2*theta2) .* cosd(phi2);
A  = A1+ A2;
%%% UNTIL HERE IS THE DYKE SOLUTION (2 PLANES). %%%

T=A;            %  Copying A matrix, T at this stage is the first
                %  contribution to the integration process.
%  Grads to radians
phi =  phi * pi/180;
theta= theta * pi/180;

%  Loop to produce rotated radiation patterns (B) and integrating
%every contribution (T)

for i=1:n-1
      B = horzcat(A(:,step*i:step:length(phi)),...
```

```
      A(:,[1:step:step*i-1]) );
      T = T + B;
%      sT =sign(T);
%  Consider just the sign of polarization
%      SUMA = abs(T);
%  Taking the absolute value of the radiation
%      [xT,yT,zT] = sph2cart(phi,theta,SUMA);
%  Converting spherical into cartesians
%      subplot(1,2,1)
%      surf(xT,yT,zT,sT);
%  Video shows the radiation pattern of:
%      axis image
%      axis([-2 2 -2 2 -2 2])
%      colormap jet
%      xlabel('x-axis');
%  sign(B): each contribution
%      ylabel('y-axis');
%      zlabel('z-axis');
%      shading flat;
%      camlight left
%      drawnow
%    gif_add_frame(gcf,('DC.gif'),10)
%     subplot(1,2,2)

end
     angulo=-[0:pi/180:pi/180*i]+pi;
     radio=ones(i+1,1);
     polarplot([0 pi],[1 1],'.b','LineWidth',6,'MarkerFaceColor', ...
     'b','MarkerSize',30)
     rticklabels({})
     thetaticks({})
     rlim([0 1.05])
     size = [600 600];
     res = 300;
```

```
    set(gcf,'paperunits','inches','paperposition',[0 0 size/res]);
    print('dyke.png','-dpng',['-r' num2str(res)]);



sT =sign(T);              %  Consider just the sign of polarization
T = abs(T);               %  Taking the absolute value of the radiation
%  Converting spherical into cartesians
[xT,yT,zT] = sph2cart(phi,theta,T);

 figure('pos',[10 10 800 1000]);        %  Plot the final summation
 surf(xT,yT,zT,sT);
 axis image
 colormap jet
 %axis image
 %title('Radiation pattern of a cylindrical fault.');
 %Change if it is a part of cylinder.
 %xlabel('x-axis');
 %ylabel('y-axis');
 %zlabel('z-axis');
 set(gca,'fontsize',50, 'fontname','Arial')
 %xticks([])
 %yticks([])
 %zticks([])

 shading flat;
 grid on
 camlight left
```

B.2 Moment tensor components

```
 #!/usr/bin/env python3
# -*- coding: utf-8 -*-
"""
```

```
Created on Mon Jun 10 19:14:43 2019

@author: eerac
"""

#%%

import matplotlib.pyplot as plt
from obspy.imaging.beachball import beachball
import numpy as np
import pandas as pd


strike=np.arange(-100,251,10) #reverse fault
#strike=np.arange(-60,211,10) #normal fault
strike=-90
dip=60
rake=-90  #NEGATIVE NORMAL, POSITIVE INVERSE
#Mzz=np.zeros(36)
#AKI CONVENTION
Mxx=-(np.sin(dip*np.pi/180)*np.cos(rake*np.pi/180)*...
np.sin(2*strike*np.pi/180) + np.sin(2*dip*np.pi/180) * ...
np.sin(rake*np.pi/180) * (np.sin(strike*np.pi/180))**2)
Mxy= (np.sin(dip*np.pi/180)*np.cos(rake*np.pi/180)*...
np.cos(2*strike*np.pi/180) + 0.5* np.sin(2*dip*np.pi/180) * ...
np.sin(rake*np.pi/180) * np.sin(2*strike*np.pi/180))
Mxz=-(np.cos(dip*np.pi/180)*np.cos(rake*np.pi/180)*...
np.cos(strike*np.pi/180) + np.cos(2*dip*np.pi/180) *...
np.sin(rake*np.pi/180) * np.sin(strike*np.pi/180))
Myy= (np.sin(dip*np.pi/180)*np.cos(rake*np.pi/180)*...
np.sin(2*strike*np.pi/180) - np.sin(2*dip*np.pi/180) *...
np.sin(rake*np.pi/180) * (np.cos(strike*np.pi/180))**2)
Myz=-(np.cos(dip*np.pi/180)*np.cos(rake*np.pi/180)*...
np.sin(strike*np.pi/180) - np.cos(2*dip*np.pi/180) *...
```

```
np.sin(rake*np.pi/180) * np.cos(strike*np.pi/180))

Mzz= np.sin(2*dip*np.pi/180) * np.sin(rake*np.pi/180)
#Mzz[:]= np.sin(2*dip*np.pi/180) * np.sin(rake*np.pi/180)

#Mzz=-5.51#*4e20  down down
#Mxx=-3.43##*4e20  north north
#Myy=-4.25##*4e20  east east
#Mxz=+1.30##*4e20  north down
#Myz=+1.18##*4e20 east down
#Mxy=-0.29#*4e20 north east


M6=Mzz*4e20  #down down
M1=Mxx*4e20  #north north
M3=Myy*4e20  #east east
M4=Mxz*4e20  #north down
M5=-Myz*4e20 #east down
M2=-Mxy*4e20 #north east

#OBSPY CONVENTION
bb=[M6,M1,M3,M4,M5,M2]
#bb=[-1,-1,2,0.0,0.0,0.0]
beachball(bb, size=60, linewidth=2,facecolor='k',...
outfile='tobba.png')

#%%
# FOR SEVERAL SOURCES, SPECFEM

#Mzz=Mrr
#Mxx=Mtt
#Myy=Mpp
#Mxz=Mrt
#Myz=-Mrp
```

```
#Mxy=-Mtp

#SPECFEM CONVENTION     to export to specfem
Mtt=Mxx*4e20
Mtp=-Mxy*4e20
Mpp=Myy*4e20
Mrt=Mxz*4e20
Mrp=-Myz*4e20
Mrr=Mzz*4e20

Mo=np.zeros(10)
for i in range(10):
    Mo[i]= 1/np.sqrt(2) * np.sqrt(np.sum(Mtt[i]**2 +...
    Mtp[i]**2 + Mpp[i]**2 + Mrt[i]**2 + Mrp[i]**2 +...
    Mrr[i]**2))

d = {'col1': Mrr, 'col2': Mtt, 'col3': Mpp, 'col4':Mrt,...
'col5': Mrp, 'col6':Mtp}
dM = pd.DataFrame(data=d)
df.to_csv('stations-caldera.dat',header=False,...
index=False,sep='\t')
```

B.3 Convert SPECFEM OUTPUT to MSEED - Python3

```
#!/usr/bin/env python3
# -*- coding: utf-8 -*-
"""
Created on Wed Oct 10 17:12:05 2018

@author: eerac

FOR RUNNING USING AN EDITOR (e.g. SPYDER). NOT DIRECT
```

```
RUNNINGCREATE MSEED FILES FOR INVERSION, INPUT=SPECFEM
OUTPUT

"""

import numpy as np
from obspy import UTCDateTime, read, Trace, Stream, write
import pandas as pd
import glob

# CENTRE OF THE MESH, EPICENTRE OF THE EVENT
evla=16000
evlo=16000


#%% STATIONS IN POLAR COORDINATES

#STATIONS IN POLAR COORDINATES
azi=np.arange(0.,331.,30.)*np.pi/180
dist=np.array([3.0,4.5,6.0,8.5,15.0])*1000.

#STATION IN CARTESIAN COORDINATES
lat_spec=[]
lon_spec=[]

for i in range(len(dist)):
    for j in range(len(azi)):
        #PLANAR PROJECTION
        lon_spec.insert(j+i*len(azi),str((dist[i]*...
        np.sin(azi[j]))+evlo))              ####IN KMS
        lat_spec.insert(j+i*len(azi),str((dist[i]*...
        np.cos(azi[j]))+evla))

#STATION AT THE EPICENTRE
```

```
lon_spec.insert(len(lon_spec)+1,str(evlo))
lat_spec.insert(len(lat_spec)+1,str(evla))

#%% STATIONS IN DEGREES (FROM A FILE)
filename='STATIONS'
coordinates=[]
f = open(filename, 'r')
events=f.readlines()
for i in range(len(events)):
    coordinates.append(events[i].strip('\n'))

station=[]
network=[]
for line in coordinates:
    station.append(line[0:3])
    network.append(line[4:6])

#FOR LAT LON ELEV DEPTH
coordinates=np.array(np.loadtxt('STATIONS',skiprows=0,...
usecols=(2,3,4,5)))

#%% CREATE A STATION FILE DEPENDING ON THE SOFTWARE TO
%USE, HERE, SPECFEM IN km

numbers=[] #FOR KIWI
stations=[]
elevation=[]
depth=[]
network=[]
for i in range(len(lat_spec)): #change if you need to plot
#Z-component, Transversal, Radial or Volumetric
    numbers.insert(i,i+1)
    elevation.insert(i,'0.0')
    depth.insert(i,'0.0')
```

```
    stations.insert(i,'S'+str(i+1))
    network.insert(i,'SY')


#COMBINING

#KIWI
d = {'col1': numbers, 'col2': stations, 'col3': ...
coordinates[:,0], 'col4':coordinates[:,1]}
df = pd.DataFrame(data=d)
df.to_csv('stations-ideal.dat',header=False, index=False,...
sep='\t')

#SPECFEM
d_spec = {'col1': stations, 'col2': network, 'col3':...
lat_spec, 'col4': lon_spec, 'col5': elevation, 'col6':depth }
df_spec = pd.DataFrame(data=d_spec)
df_spec.to_csv('STATIONS',header=False, index=False,sep='\t')



#%% CREATE MSEED FILES FOR KIWI FROM SPECFEM FILES
samp=125.
starttime=10000 #UTCDateTime
delayNP=200*samp
comp='H'

cwd = 'DISPL'#os.getcwd()
strings=sorted(glob.glob('*XX.semd'))

for name in strings:

# X-component
    print(name)
```

```
    dataX=np.array(np.loadtxt(name,skiprows=0))
    z=np.zeros((len(dataX)+delayNP,2))
    a=np.zeros((len(dataX)+delayNP,2))
    a[delayNP:,1] = dataX[:,1]

    header = {'delta': 1.0/samp, 'network': name[:2], ...
    'station': name[3:6], 'channel': comp+'HE',
              'starttime' : starttime}

    sac = Stream([Trace(data=a[:,1], header=header)])

    sac.write(cwd+'.'+name[3:6]+'.'+comp+'HE',...
    format='MSEED', encoding=5, reclen=256)
    st=read(cwd+'.'+name[3:6]+'.BHE')
    st[0].decimate(factor=5,strict_length=False)
    st[0].decimate(factor=5,strict_length=False)
    st[0].decimate(factor=5,strict_length=False)
    #next line to add noise
    #st[0].data=st[0].data + np.max(np.abs(st[0].data))*...
    np.random.random(len(st[0].data))*...
    np.random.choice([-1,1],size=(len(st[0].data)))/50
    st.write(cwd+'.'+name[3:6]+'.BHE', format='MSEED', ...
    encoding=5, reclen=256)

# Y-component

    dataY=np.array(np.loadtxt('SY.'+name[3:6]+'.'+comp+'XY.semd',...
    skiprows=0))

    z=np.zeros((len(dataY)+delayNP,2))
    a=np.zeros((len(dataY)+delayNP,2))
    a[delayNP:,1] = dataY[:,1]
```

```
  header = {'delta': 1.0/samp., 'network': name[:2], ...
  'station': name[3:6], 'channel': comp+'HN',
            'starttime' : starttime}

  sac = Stream([Trace(data=a[:,1], header=header)])

  sac.write(cwd+'.'+name[3:6]+'.BHN', format='MSEED', encoding=5,...
  reclen=256)
  st=read(cwd+'.'+name[3:6]+'.BHN')
  st[0].decimate(factor=5,strict_length=False)
  st[0].decimate(factor=5,strict_length=False)
  st[0].decimate(factor=5,strict_length=False)
  #next line to add noise
  #st[0].data=st[0].data + np.max(np.abs(st[0].data))*...
  np.random.random(len(st[0].data))*...
  np.random.choice([-1,1],size=(len(st[0].data)))/50
  st.write(cwd+'.'+name[3:6]+'.BHN', format='MSEED', encoding=5, ...
  reclen=256)

# Z-component

  dataZ=np.array(np.loadtxt('SY.'+name[3:6]+'.'+comp+'XZ.semd',...
  skiprows=0))

  z=np.zeros((len(dataZ)+delayNP,2))
  a=np.zeros((len(dataZ)+delayNP,2))
  a[delayNP:,1] = dataZ[:,1]

  header = {'delta': 1.0/samp., 'network': name[:2], 'station': ...
  name[3:6], 'channel': comp+'HZ',
            'starttime' : starttime}


  sac = Stream([Trace(data=a[:,1], header=header)])
```

```
    sac.write(cwd+'.'+name[3:6]+'.BHZ', format='MSEED', encoding=5,...
    reclen=256)
    st=read(cwd+'.'+name[3:6]+'.BHZ')
    st[0].decimate(factor=5,strict_length=False)
    st[0].decimate(factor=5,strict_length=False)
    st[0].decimate(factor=5,strict_length=False)
    #next line to add noise
    #st[0].data=st[0].data + np.max(np.abs(st[0].data))*...
    np.random.random(len(st[0].data))*...
    np.random.choice([-1,1],size=(len(st[0].data)))/50
    st.write(cwd+'.'+name[3:6]+'.BHZ', format='MSEED', encoding=5,...
    reclen=256)
```

B.4 Gas fraction Calculations

```
 import numpy as np
import matplotlib.pyplot as plt

h=1500 #m
g=9.8 #SI
TwtP=np.array([4.5,5.5,6.5])   # % of total gas at 1500m
rho_m=2300 #kg/m3
T=1123.15 #K = 850ÂřC
molM_h2o=18.015e-3 #kg
Rg=8.31 #SI
R=15 #m
#magma extruded
data=np.array(np.loadtxt('vol-extruded.dat',skiprows=0))
data[:,1] = data[:,1] * 1e6

# Extrusion rate per day
rate=np.zeros((len(data)))
```

```
for i in range(len(data)-1):
    rate[i+1]=data[i+1,1]-data[i,1]

#Lithostatic Magmastatic pressure calculated with melt density
P=rho_m * g *h

#This value is too high  because the bulk density is less, however,
#it can be approximated as: Pmelt = Pbulk + excess pressure in
#magma chamber

# wt% of dissolved gas at 1500m
ndg = 4.1e-6 * np.sqrt(P)

#exssolved gas at 1500m
neg = TwtP/100 -ndg

# density of gas at 1500m
rho_g= molM_h2o * P/(Rg*T)

#bulk density of magma
rho_bulk =((1-neg)/rho_m + neg/rho_g)**-1

#gas fraction and volumes
# Select extrusion per day or period of time or random numbe data
#referred to  15 nov 1995
xi = rho_bulk/rho_g * neg

start=np.array([585]) #547 start Sparks
#start=int(start[0])
end=np.array([591])   #814 for Sparks final
#end = int(end[0])
a=len(end)
b=len(neg)
Vm=np.zeros((a,1))
```

```
Vg=np.zeros((a,b))
Vt=np.zeros((a,b))
days=np.zeros((a,1))
Q=np.zeros((a,b))
v_med=np.zeros((a,b))
v_max_cyl=np.zeros((a,b))
v_max_dyke=np.zeros((a,b))
st_rate=np.zeros((a,len(neg)))
sh_stress=np.zeros((a,len(neg)))

for i in range(len(end)):
    Vm[i,0]=np.sum(rate[start[i]:end[i]])   #data[259,1]
    Vg[i,:] = xi*Vm[i]/(1-xi)
    Vt[i,:] = Vm[i] + Vg[i,:]

# FLUX days considered and hours per day: total period 847 days
    days[i]=end[i]-start[i]
    hours=15. # 2 cycles
    Q[i,:] = rho_m * Vm[i] /(days[i] *hours*3600 ) * 1/rho_bulk

#velocities of magma at 1500m given conditions above
    v_med[i,:] = Q[i,:]/(np.pi*R**2) # flux/area
    v_max_cyl[i,:] = 2 * v_med[i,:]
    v_max_dyke[i,:] = 3/2 * v_med[i,:]

#strain rate
    st_rate[i,:] = 4/(np.pi*R**3) * Q[i,:]
    sh_stress[i,:] = 1e8 * st_rate[i,:]
#condition for rupture
strength =1e7
visc = strength/st_rate

start=int(start[0])
end = int(end[0])
```

```
plt.figure(dpi=100)
plt.plot(data[start:end,0],data[start:end,1])
plt.ylabel('Extruded Melt (Mm$^3$)', ha='center', va='center', ...
rotation='vertical', fontsize = 18, labelpad=20)
plt.xlabel('Time (s)', ha='center', va='center', fontsize = 20, ...
labelpad=10)
plt.tick_params(axis='both', which='major', labelsize=16, pad=5)
#plt.savefig('cumulative_extrusion9707.pdf',dpi=300)
plt.figure(dpi=100)
plt.plot(data[start:end,0],rate[start:end], color='orange')
plt.ylabel('Extrusion Rate (Mm$^3$/day)', ha='center', va='center',...
rotation='vertical', fontsize = 18, labelpad=20)
plt.xlabel('Time (s)', ha='center', va='center', fontsize = 20,...
labelpad=10)
plt.ticklabel_format(axis='y', style='sci', scilimits=(-2,2))
plt.tick_params(axis='both', which='major', labelsize=16, pad=5)
#plt.savefig('extrusion_rate9707.pdf',dpi=300)
np.sum(rate)/847
np.average(rate)


plt.figure(dpi=100)
plt.subplot(2,1,1)
plt.plot(data[start:end,0],rate[start:end], color='orange')
plt.ylabel('Extrusion Rate (m3/day)', ha='center', va='center', ...
rotation='vertical', fontsize = 12, labelpad=5)
plt.xlabel('Time (days)', ha='center', va='center', fontsize = 12,...
labelpad=10)
plt.ticklabel_format(axis='y', style='sci', scilimits=(-2,2))

plt.subplot(2,1,2)
plt.bar(number.keys(), number.values())
plt.ylabel('All Seismicity (events/day)', ha='center', va='center',...
```

```
rotation='vertical', fontsize = 12, labelpad=5)
plt.xlabel('Time (days)', ha='center', va='center', fontsize = 12,...
labelpad=10)
plt.ticklabel_format(axis='y', style='sci', scilimits=(-2,2))
plt.tight_layout(pad=0.7, w_pad=2.0, h_pad=0.0)

#plt.savefig('extrusion_rate-seismicity.pdf',dpi=300)
plt.show()



fig, ax1 = plt.subplots(figsize=(10,5))

color = 'tab:red'
ax1.set_title('Extrusion rate and cumulative amplitudes per day')
ax1.set_xlabel('time (s)')
ax1.set_ylabel('exp', color=color)
ax1.plot(data[start:end,0],rate[start:end], color=color)
plt.ylabel('Extrusion Rate (m3/day)', ha='center', va='center', ...
rotation='vertical', fontsize = 12, labelpad=5)
plt.xlabel('Time (days)', ha='center', va='center', fontsize = 12,...
labelpad=10)
ax1.ticklabel_format(axis='y', style='sci', scilimits=(-2,2))
ax1.tick_params(axis='y', labelcolor=color)

ax2 = ax1.twinx()  # instantiate a second axes that shares the same
#x-axis

color = 'tab:blue'
ax2.set_ylabel('sin', color=color)  # we already handled the x-label
ax2.bar(data[start:end,0], number[36:42],alpha=0.5)
plt.ylabel('All Seismicity (events/day)', ha='center', va='center',...
rotation='vertical', fontsize = 12, labelpad=5)
plt.xlabel('Time (days)', ha='center', va='center', fontsize = 12,...
```

```
labelpad=10)
ax2.ticklabel_format(axis='y', style='sci', scilimits=(-2,2))
ax2.tick_params(axis='y', labelcolor=color)

fig.tight_layout()  # otherwise the right y-label is slightly clipped
#plt.savefig('extrusion_cumulative_amplitudes.pdf',dpi=300)
plt.show()


fig, ax1 = plt.subplots(figsize=(10,5))

color = 'tab:red'
#ax1.set_title('Extrusion rate and seismicity single family',...
fontsize = 12)
ax1.set_xlabel('time (s)', fontsize = 12)
ax1.set_ylabel('exp', color=color)
ax1.set_xlim(584.5, 589.5)
ax1.bar(0.5+data[start:end,0],rate[start:end], color=color)
plt.ylabel('Extrusion Rate (m3/day)', ha='center', va='center',...
rotation='vertical', fontsize = 18, labelpad=5)
plt.xlabel('Time (days)', ha='center', va='center', fontsize = 18,...
labelpad=10)
ax1.ticklabel_format(axis='y', style='sci', scilimits=(-2,2))
ax1.tick_params(axis='y', labelcolor=color, labelsize=18)
ax1.tick_params(axis='x', labelsize=18)

ax2 = ax1.twinx()  # instantiate a second axes that shares the same x

color = 'tab:blue'
ax2.set_ylabel('sin', color=color)  # we already handled the x-label
ax2.bar([t1,t2,t3,t4,t5,t6,t7],[c1,c2,c3,c4,c5,c6,c7],width=0.2,...
alpha=0.5)
plt.ylabel('Cumulative seismic moment (Nm)', ha='center', va='center',
...
```

```
rotation='vertical', fontsize = 18, labelpad=5)
plt.xlabel('Time (days)', ha='center', va='center', fontsize = 18,...
labelpad=10)
ax2.ticklabel_format(axis='y', style='sci', scilimits=(-2,2))
ax2.tick_params(axis='y', labelcolor=color, labelsize=18)


fig.tight_layout()  # otherwise the right y-label is slightly clipped
plt.savefig('extrusion_Mo.pdf',dpi=300)
plt.show()
```

B.5 Cross Correlation

```
 #!/usr/bin/env python3
# -*- coding: utf-8 -*-
"""
Created on Thu Nov 22 17:19:44 2018

@author: eerac
"""

#%%
import matplotlib.pyplot as plt
import numpy as np
from scipy import signal
from obspy.imaging.spectrogram import spectrogram
#from __future__ import print_function
import os
import errno
from obspy import UTCDateTime, read, Trace, Stream, signal
from obspy.signal.cross_correlation import correlate,xcorr_max
from obspy.io.sac.sactrace import SACTrace
import pandas as pd
import glob
```

```
from obspy.imaging.beachball import beachball
from obspy.signal.invsim import corn_freq_2_paz
import time


#%% DATA IN SEISAN
#read files want to plot
string=sorted(glob.glob('../../Sparks/9711*MVO_*'))

stn='MBGH' #'MBGB'

for name1 in string:

    s1=read(name1)

    for j in range(len(s1)):
        if (s1[j].stats.station == stn):
            a=s1[j].data
            header = {'delta': 1/75., 'network': 'MVO','station': ...
            s1[j].stats.station, 'channel': s1[j].stats.channel, ...
            'starttime' : s1[j].stats.starttime}
            sac = Stream([Trace(data=a, header=header)])

            sac.write(name1[:-5] +'.' +s1[j].stats.station +'.'+ ...
            s1[j].stats.channel, format='MSEED')#, encoding='FLOAT64',
...
            reclen=256)

#%% DATA IN MSEED ALREADY

#from numba import jit

start_time = time.time()
```

```
date='9707'
stn='MBGH'
#read files want to plot
string=sorted(glob.glob('./Sparks/'+date+'*'+stn+'*Z'))
cwd = os.getcwd()


##CHANGE THIS FOR PERIODS IN SPARKS INSTEAD OF MONTHS
g=np.zeros((len(string)))
k=0
l=0
used=[]



for name1 in string:

    s1=read(name1)
    s1_filt = s1[0].copy()
    s1_filt.filter('bandpass', freqmin=0.5,freqmax=5.0, corners=2,...
    zerophase=True)
    a=s1_filt.data
    m=0
    w=0
    for name2 in string:
        s2=read(name2)
        if (name2 in used or name1 in used or name1 == name2):
            pass
        else:
            s2_filt = s2[0].copy()
            s2_filt.filter('bandpass', freqmin=0.5,freqmax=5.0,...
            corners=2, zerophase=True)
            b=s2_filt.data
```

```
            corr= correlate(a,b,np.max([len(a),len(b)]))
            shift, value = xcorr_max(corr)
            if (value > 0.7):
                g[m]=k
                used.insert(l,name2)
                l=l+1
                w=w+1
        m=m+1

    if (w>0): #if name1 at least correlates with 1 event, do this if.
        used.insert(l,name1)
        l=l+1
        g[k]=k
    k=k+1   #CHANGE THIS FOR PERIODS IN SPARKS INSTEAD OF MONTHS
print("--- %s seconds ---" % (time.time() - start_time))

#%%

np.savetxt('families-'+date+stn+'.txt',g)
```

B.6 Seismic moment estimation Montserrat

```
 import matplotlib.pyplot as plt
import numpy as np
from scipy import signal
from obspy.imaging.spectrogram import spectrogram
#from __future__ import print_function
import os
import errno
from obspy import UTCDateTime, read, Trace, Stream, signal
from obspy.signal.cross_correlation import correlate,xcorr_max
from obspy.io.sac.sactrace import SACTrace
import pandas as pd
import glob
```

```
from obspy.imaging.beachball import beachball
from obspy.signal.invsim import corn_freq_2_paz
import time

GURALP30_MBRY_z = {'poles': [-0.14803 + 0.14803j, -0.14803 - 0.14803j,...
      -314.16 + 0.0j],
              'zeros': [0.0 + 0.0j, 0.0 + 0.0j, 999.0 + 0.0j, 0.0 + 0.0j],
              'gain': -0.314*(2*np.pi)**0, 'sensitivity': 0.904422254e9}

st=np.loadtxt('./MONTY-NoAtt/RING19-3/MVO.MBLG.HXZ.semd')
plt.plot(st[:,0],st[:,1])
np.max(np.abs(st[:,1]))

amp=np.array([0.0, 2.93256762e-06])#, 0.00177025003])
Mo=np.array([0.0, 1.71e11])#, 1.71e14])
from scipy import stats
slope, intercept, r_value, p_value, std_err = stats.linregress(amp,Mo)
#displacement slope=9.66e16 intercept=8.21e6
#velocity slope=8.06e15 intercept=2.12e7
x=np.arange(0,0.000002,0.0000001)
lin=slope*x + intercept
plt.figure(figsize=(8,6),dpi=300)
plt.scatter(amp,Mo, marker='+',color='red',linewidth=10)
plt.ylim(0,2e11)
plt.xlim(0,0.000002)
plt.ticklabel_format(axis='x', style='sci', scilimits=(-2,2))
plt.plot(x,lin,color='blue')
plt.xticks([0, 0.000001,0.000002],fontsize=18)
plt.yticks([0, 1e11],fontsize=18)
plt.xlabel('Maximum amplitude at MBLG $A_{max}$ (m)',  fontsize=18,labelpad=10)
plt.ylabel('Equivalent seismic moment $M_{o}$ (Nm)', fontsize=18, labelpad=10)
#f.tight_layout()
#plt.savefig('Regression.pdf')
```

```
events2=[]
f = open('events1test.txt', 'r')
events=f.readlines()
for i in range(len(events)):
        events2.append(events[i].strip('\n'))

maximum=np.zeros((len(events2)+16))
Mo_ps=np.zeros((len(events2)+16))
Mo=np.zeros((len(events2)+16))
hd=np.zeros((len(events2)+16))
d=np.zeros((len(events2)+16))
d_root=np.zeros((len(events2)+16))
h=np.zeros((len(events2)+16))
header = {'delta': 1.0/75.}
mu=2.1e9
perimeter=30*np.pi
for i in range(len(events2)):
    st1=np.loadtxt(events2[i])
    st1=st1-np.mean(st1)
    st1 = Stream([Trace(data=st1, header=header)])
    st1[0].simulate(paz_remove=GURALP30_MBRY_z,...
    remove_sensitivity=True,...
    water_level=60.0,zero_mean=False, taper=False, pre_filt=None, ...
    nfft_pow2=True, pitsasim=True)
    st1.filter('bandpass', freqmin=0.5,freqmax=5.0, corners=2,...
    zerophase=True)
    st1=st1[0].data-np.mean(st1[0].data)
    maximum[i]=np.max(np.abs(st1))


amp_doub=np.array([7.8975380203011516e-07,1.0691812381946333e-06,
9.4137999278001967e-07,8.9605398272221515e-07,1.2266900682800096e-06,
1.0757286170603226e-06,7.3339231451615679e-07,1.7172375099472065e-06,
```

```
1.6598021925783931e-06,3.5731820269934419e-07,1.0850721018029901e-06,
1.0171974210008405e-06,1.7364972650073909e-06,1.4117485523377734e-06,
1.534345390649817e-06,5.8278058256937346e-07])
maximum[-16:]=amp_doub

Mo_ps=(slope*maximum+intercept)
Mo=42*(slope*maximum+intercept)
hd=Mo/(mu*perimeter)
d=1.66e-7*(Mo/42.)**(1/3)*42
h=hd/d
d_root=np.sqrt(hd)

np.sum(Mo_ps)      # ~4.47e13        doubles:4.64e13
np.sum(Mo)         # ~1.877e15       displ:1.95e15
np.sum(hd)         #                 displ:9851m2      0.1:206888
np.sum(d)          #  7.55777        displ:0.84m       0.1:
np.sum(h)          #                 displ: 3009km     0.1:63198932
np.sum(d_root)     #  7.55777        displ:1558m       0.1:7278
```